Computational Study of Rotorcraft Aerodynamics in Ground Effect and Brownout

Catriona Phillips

Submitted in fulfilment of the requirements

for the degree of

Doctor of Philosophy

Department of Aerospace Engineering

Faculty of Engineering

University of Glasgow

May 2010

Abstract

When helicopters operate close to the ground in desert conditions, the rotor wake can entrain large amounts of dust into the flow field surrounding the aircraft. This entrainment of dust can result in the potentially dangerous condition known as brownout where the pilot loses situational awareness. Understanding the physics that governs the entrainment of dust from the ground may eventually allow the condition of brownout to be avoided completely.

To enable the formation of dust clouds around helicopters to be investigated, Brown's Vorticity Transport Model (VTM) has been enhanced to include the ability to model the entrainment of dust from the ground and the transport of this dust once in the flow field. Comparison of the predictions of the VTM with experimental results has shown the VTM to be capable of capturing the general characteristics of the dust clouds. Close examination of the formation of the dust clouds revealed that the general physics that governs the entrainment process is the same for different rotors and a universal model of this process is described. Differences in the size and density of the dust clouds that form around different rotors result from differences in the overall behaviour of the wakes that are generated.

The design of a rotor can have a significant effect on the size and density of the dust cloud that is produced. The tip vortices have been identified as the main cause of the changes to the dust cloud. However, the behaviour of these tip vortices, when the rotor is operating in ground effect, is dependent on the rotor design and also on the advance ratio of the rotor. Thus, to determine the size and density of the dust cloud that would form around any particular rotor, the behaviour of the wake of that rotor must first be known.

Acknowledgements

I would like to thank my supervisor Professor Richard Brown for his endless support, guidance and encouragement throughout my PhD. I have learned a lot under his supervision and the work I have done has improved continuously. I would also like to thank my colleagues, past and present, who made life in the office both enjoyable and entertaining. I would finally like to thank my family and friends for the encouragement and support they have shown throughout my studies.

Contents

List of Figures

List of Tables

Nomenclature

Rotor System

A	rotor disc area
c	blade chord
C_D, C_L, C_M	sectional drag, lift and pitching moment coefficients, respectively
C_P	rotor power
C_T	rotor thrust, scaled by $\rho A(\Omega R)^2$
h	height of rotor above ground
N_b	number of blades
r	radial position, scaled by R
R	rotor radius
R_c	root cutout
T	rotor thrust
θ_0	collective pitch
θ_{1c}, θ_{1s}	lateral, longitudinal cyclic pitch, respectively
μ	advance ratio
$\mu^\star$	thrust normalised advance ratio, $\mu/\sqrt{C_T/2}$
σ	rotor solidity, blade area divided by rotor disc area
Ψ	azimuthal location, zero at rear of disc, positive anticlockwise
Ω	rotor rotational speed

Particle Model

d	particle diameter
m	particle mass
ρ_s	material density of particles
ς	'species' of particle
Σ	species band of particle

Fluid and Particle Dynamics

F	intercell vorticity flux *or* drag force on particle
g	acceleration due to gravity
K_δ	regularised Biot-Savart Kernel
p	pressure
Q	horizontal flux of particles
S_p	source of particulates
S_ω	source of vorticity
t	time
u	velocity of particle relative to air
V	cell volume
W	weighting factor
Γ	particle drag to mass ratio
Γ_v	tip vortex strength
ν	fluid viscosity
ν_p	particle diffusion constant
Π	projection operator
ρ	air density
ρ_p	local density of particulates in air
σ	particle phase space

υ	local flow velocity
υ_b	local on-blade velocity
υ_g	fallout velocity due to gravity
υ_p	particle velocity
υ_t	threshold velocity
Φ	particle probability density function
ω	vorticity
ω_b	blade bound vorticity

Structural Dynamics

D	dissipation
$\mathcal{L}$	Lagrangian of the system
q	generalised coordinates
Q	work done
T	kinetic energy
U	potential energy

Abbreviations

CFD	Computational Fluid Dynamics
FMM	Fast Multipole Method
IGE	In Ground Effect
OGE	Out of Ground Effect
VTM	Vorticity Transport Model
WAF	Weighted Average Flux

Chapter 1

Introduction

When helicopters are flown at low speed above desert or dusty surfaces a very real concern to their operators is the tendency for the rotor wake to disturb the surface and to entrain dust particles into the airflow surrounding the aircraft. This entrainment of dust can lead to the potentially dangerous condition known as 'brownout' where the pilot loses situational awareness as the dust cloud engulfs the aircraft and their view becomes obscured. Not only can this result in a loss of life in the severest of cases but significant damage can be done to the aircraft when operating in such conditions. Over time the constant bombardment of dust particles on the rotor blades causes the blades to erode. Additionally, dust particles that enter into the rotating components of the rotor cause a similar problem. Further to this, the continual build up of dust within the helicopter that occurs during sustained operations in desert conditions can, over time, reduce the payload of the aircraft. Over the past few years there has been a large increase in military operations in Iraq and Afghanistan. According to the Army Aviation Applied Technology Directorate, in the first year of the war in Iraq, equipment damage to helicopters, as a direct result of operating in dusty conditions, has cost the US Army $60 million in addition to suffering three fatalities and 29 non-fatal injuries. Thus, due to the current political climate, there has been a recent resurgence of interest in the area of rotor operation in ground effect and brownout.

1.1 Overview of Rotor Flight In Ground Effect

The effect of dust erosion on helicopters operating in dusty environments has always been a problem. There was interest in this topic of dust entrainment by rotor wakes back in the 1960s when Rodgers [1], using a Piasecki H-21, conducted flight tests in which dust was collected at various sampler stations around the aircraft when it was hovering above a dusty surface. The density of the dust cloud surrounding the aircraft was estimated from the dust that was collected. Until very recently, further research on this topic, at least that which has been published, has been limited. In 2006, further flight tests were conducted, as reported by Cowherd [2], in which a number of different helicopters were flown above a dusty surface. During this set of tests, the dust which became entrained into the flow field was collected at stationary points on the ground as opposed to being collected in samplers located on the aircraft itself. As with the number of flight tests, the number of controlled laboratory experiments which have investigated the formation of dust clouds around rotors has been minimal. Work published on the topic is limited to that conducted at the universities of Glasgow [3] and Maryland [4, 5] and at Continuum Dynamics, Inc [6]. These experimental investigations have provided valuable insight into the flow physics which govern the onset of brownout. There is perhaps more interest in numerical simulation of helicopter brownout, with Haehnel *et al.* [7], Wachspress *et al.* [8, 9], Whitehouse *et al.* [6] and D'Andrea [10] all having published work describing computational techniques for simulating the entrainment and transport of particles in the flow field around helicopters. As the downwash from the rotor influences the entrainment of dust from the ground plane, Wadcock *et al.* [11] examined the downwash characteristics of two different helicopters. This recent computational work has focused on understanding how the rotor wake, as it interacts with the ground, affects the size and geometry of the dust cloud that is generated. The hope is that, by changing the design of helicopters or the trajectories they follow when landing, the dust clouds that cause brownout can be ameliorated through aerodynamic means.

When using computational simulation to investigate brownout, accurate simulation of the flow field around helicopters in ground effect is an important pre-requisite to the correct simulation of the dust clouds that can form around helicopters in dusty conditions. The induced velocity of the flow field influences the formation of the dust cloud. Thus, by understanding the behaviour of the flow field around a rotor in close proximity to the ground, the behaviour of the dust cloud can be deduced. There is a large body of work which examines rotor operation in ground effect in both hover and forward flight. This body of work can thus be used to verify the predictions of computational models and to confirm whether the velocity field, and subsequently the formation of the dust cloud, are calculated correctly.

Analytical studies on the effect of a ground plane on the performance of lifting airscrews were being conducted as far back as 1937 when Betz [12] and later Knight and Hefner [13, 14] and Zbrozek [15] investigated the effect of the ground on the thrust and power requirements of an airscrew. They reported that, the greater the height of the rotor above the ground, the smaller the effect of the ground on the thrust and power requirements. The effect of the ground becomes almost negligible at a height of one rotor diameter above the ground. This line of work was extended by Cheeseman and Bennett [16] who investigated the effect of the ground on the thrust and power requirements when a helicopter is operated in forward flight close to the ground. They reported that, in forward flight, the power required by the rotor for a given thrust decreases when the height of the rotor above the ground decreases. When the forward flight speed increases, however, the effect of the ground plane decreases. A number of flight tests were conducted using a variety of different aircraft to investigate the power required to hover at a constant thrust in ground effect. The results of these tests were documented by Hayden [17]. The very complex nature of the flow field produced in ground effect was confirmed by Fradenburgh [18] who also reported that, in ground effect, the rotor experiences an upflow through the centre of the rotor. The results of these studies can all be used to validate the predictions of computational models.

With perhaps more relevance to the accurate prediction of the dust clouds that form

around helicopters when operating in desert environments, further experimental studies have focused on the changes in wake geometry with forward speed in the presence of a ground plane. Sheridan and Wiesner [19] present results from wind tunnel tests conducted during the 1970s by Boeing Vertol. They reported that, at low forward speed in flight close to the ground, a ground vortex forms upstream of the rotor. As the flight speed increases, this ground vortex moves closer to the rotor before eventually moving below and to the aft of it. They also noted that these changes in the wake geometry have an effect on the cyclic pitch required to trim the rotor. The lateral cyclic pitch required in ground effect is less than that required out of ground effect. An experimental investigation by Curtiss *et al.* [20] involving smoke flow visualisation confirmed the presence of a ground vortex but they characterised the flow field by two distinct regimes which are dependent on the rotor advance ratio and height above the ground. In the first of these regimes, called by them the recirculation regime, which occurs at low advance ratios, the rotor wake flows forward and upwards and recirculates through the front of the rotor. The formation of a well-defined horseshoe vortex below the rotor at slightly higher advance ratios occurs in the second, ground vortex, regime. They also reported that a marked change in the forces and moments experienced by the rotor occurs as the ground vortex moves below the rotor. By use of computational modelling, Whitehouse and Brown [21] confirmed the presence of these regimes. They also described a third regime which occurs between the recirculation and ground vortex regimes. In this third regime, called by them the intermittent regime, there is some of the disorder associated with the recirculation regime but there is also a ground vortex just upstream of the leading edge of the rotor. Further work was performed by Curtiss, Erdman and Sun [22] to investigate to what extent translational acceleration alters the ground effect that is experienced by a rotor. They found that acceleration can have a significant effect on the forces and moments experienced by the rotor near to the critical advance ratio at which the flow moves from being recirculatory to forming a ground vortex. Acceleration from hover was found to extend the range of advance ratios at which the recirculation regime exists and to delay

the formation of the ground vortex to a higher advance ratio. This change in ground vortex formation results in the rotor hub moments staying roughly constant over a larger range of advance ratios. It was also reported that this effect of rotor acceleration increases as the height of the rotor above the ground decreases. The changes in wake geometry described in these references will be shown in the present work to have a significant influence on the dust cloud that forms around the rotor when operating close to the ground in desert environments. Thus, computational methods must be capable of capturing these changes in the wake in order to predict accurately the dust distribution around a helicopter.

Further experimental investigations of the unsteadiness of the flow field associated with helicopters operating in ground effect have been conducted by Cimbala *et al.* [23], Saijo *et al.* [24, 25] and Ganesh and Komerath [26, 27]. Cimbala *et al.* studied the ground vortex that forms when a jet impinges on a ground plane in the presence of a cross flow. They reported that the ground vortex was found to be highly unsteady and expands and contracts at a very low frequency. Vortices shed from the lip of the jet exit were found to combine to form the ground vortex. These vortices were shown to add to the higher frequency unsteadiness of the ground vortex but were not the cause of the low frequency pulsations. The frequency of the pulsation of the ground vortex is highly dependent on freestream velocity. Saijo *et al.* [24, 25] used flow visualisation to study features in the rotor wake that are associated with rotor operations close to the ground and augmented this by using hot wire measurements to examine the unsteadiness within the wake. Hot wire anemometry was also adopted by Ganesh and Komerath in Ref. [26]. Ganesh and Komerath extended their work by using Particle Image Velocimetry (PIV) to examine the formation of the ground vortex and to measure the velocities in and around it [27]. They concluded that the ground vortex is composed of an accumulation of the tip vortices produced by the rotor. They also noted that the strength of the ground vortex was more than four times the strength of the individual tip vortices produced by the rotor.

An investigation into the effect of the ground plane in distorting the trajectory of the tip

vortices which are trailed from the rotor blades was conducted by Light [28]. The position of the tip vortices produced by a full-scale Lynx tail rotor placed close to a large, disc-shaped ground board were obtained by photographing the vortices using a wide-field shadowgraph method. Light showed that when a rotor is in ground effect, the axial descent rate of the tip vortices decreases as they reach the ground plane. In the radial direction, as with hover out of ground effect, the trajectory of the tip vortices is seen to contract initially. The radial displacement of the vortices then increases dramatically as the rotor wake approaches the ground plane.

Another feature of the rotor wake when a helicopter is operating in ground effect is that, when the wake interacts with the ground plane, the tip vortices combine to form what can be thought of as a wall jet. A number of flight tests have been conducted in which the radial velocities produced by a variety of different aircraft have been recorded. This data has been documented by Preston [29] and has been used to construct a semi-empirical mathematical model which can be used to calculate the shape and magnitude of the rotor outwash. Lee *et al.* [4] have conducted an experimental investigation, using flow visualisation and digital particle image velocimetry, to examine the effect of a ground plane on the rotor downwash. By studying the effect of the rotor height on the velocity profile produced, Lee *et al.* reported that the flow velocities along the ground are dependent on the height of the rotor above the ground. It is known that the development of the dust cloud around a helicopter is strongly linked to the induced velocities within the rotor wake. When using computational models to investigate the formation of the dust clouds in the flow field around helicopters, it is thus essential that these induced velocities are predicted accurately.

The analytical and experimental studies referred to above provided valuable information on the characteristics of flight in ground effect. The understanding of the dynamics of the flow field can be enhanced by the use of computational models to simulate rotor flight in ground effect. Although many years of development of computational models has resulted in rotor wake and performance predictions being acceptable in most operational flight con-

ditions, the presence of a ground plane still poses some challenges. In the free-vortex wake method, as adopted by Graber *et al.* [30], Keller *et al.* [31] and Leishman *et al.* [32, 33] amongst many others, a concentrated tip vortex is trailed from each rotor blade into the wake. This vortex is then convected through the flow field. In terms of computational expense, this method is fairly efficient. It is limited, however, in that the small scale structures, which result from the breakdown of the larger vortical structures, may not be captured. The approach used for the simulations presented in this dissertation reveals these smaller scale features of the flow field. In Brown's Vorticity Transport Model (VTM), the vortical structures within the rotor wake are conserved explicitly and thus exist within the flow field for very long periods of time. The small scale structures which form from the breakdown of the larger vortical structures, due to the inherent instability in the wake, are revealed. When examining the behaviour of the wake in ground effect and investigating the physics which governs the formation of the resulting dust cloud, this preservation of the vortical structures is essential.

1.2 Aims

When examining the generation of the dust clouds that form around helicopters when operating in ground effect in desert conditions, the limited body of published experimental data has resulted in only a small amount of information being available regarding the fundamental processes that are involved. The main aim of this research is to provide results from which a better understanding of the physics that govern the behaviour of the dust clouds can be obtained. Also investigated are how the size and density of the resulting dust cloud relates to the design of the helicopter. By conducting these investigations and gaining a better understanding of the physics which is involved with the formation of the dust clouds around helicopters, it is hoped that a fully aerodynamic solution to the problem of brownout may eventually be obtained.

Insight into the formation of the dust clouds will be gained by examining the behaviour of rotor wakes when operating in ground effect and establishing how this behaviour relates to the entrainment of dust from the ground. Thus, the first aim of this research is to determine the ability of the VTM to predict correctly the wake structures generated by rotors in ground effect. With confidence in the predictions of the VTM so obtained, the code is modified to include the simulation of particles within the flow field. The second aim is then to understand how the vorticity contained within the rotor wake, and hence, the velocity within the flow field, is related to the entrainment of dust from the ground plane and the transport of this dust once in the flow field. When investigating this process the work will focus on the fundamental questions of particle entrainment in an attempt to understand the underlying physics that governs the formation of dust clouds around helicopters. The final aim of the research presented in this dissertation is to establish which rotor parameters have the greatest effect on the size and density of the dust cloud that is generated around the helicopter when operating in hover and forward flight in close proximity to a ground plane. The results from this investigation should provide valuable information that may be considered when designing new helicopters in which the tendency of the helicopter to induce brownout must be reduced.

1.3 Synopsis

The work contained in this dissertation is structured as follows. In Chapter 2, the theory and numerical implementations used within the VTM are presented. The techniques used when calculating the evolution of the wake are described, including how the governing equations are solved and how the computational domain is structured. The blade aerodynamic and structural dynamic models and the method used to trim the helicopter are then defined. Finally, the method by which a ground plane is implemented is described.

Chapter 3 provides verification of the ability of the VTM to capture the behaviour of the

wake and the operating properties of a rotor when it is operated in ground effect. A number of comparisons have been conducted previously between experimental data and the predictions of the VTM for flight out of ground effect (OGE) [34,35,36]. The results presented in this chapter, however, highlight the ability of the VTM in ground effect (IGE), as correct prediction of the wake structures generated by rotors is an essential pre-requisite to the correct modelling of brownout.

To simulate particle transport within the flow field around helicopters in order to model brownout, the VTM is modified to include particle entrainment and transport models. These modifications to the VTM are described in Chapter 4. The numerical implementation of the model for the transport of the particles, once in the flow field, is presented. The particles must also be capable of entering and settling out of the flow field. The semi-empirical models used to simulate these two processes are also described. The computational implementation of the modification is discussed before, finally, the predictions of the VTM of particle distributions within the flow field are verified.

The distribution of dust within the flow field around a helicopter is dependent on the behaviour of the rotor wake. Thus, an investigation into the variation of wake structure with rotor configuration is presented in Chapter 5. The differences in wake geometry as generated by different rotors when hovering at various heights above the ground are presented. Anecdotal evidence suggests that tandem rotor helicopters are more susceptible to inducing brownout than single rotor helicopers. Thus, the wake structure generated by a single rotor and a tandem rotor configuration helicopter during forward flight are compared. The connection between vorticity, velocity and dust is then established and the physics governing the entrainment process is described. This is followed by an examination of the dust distributions generated by the single rotor and tandem rotor configurations.

Chapter 6 presents an investigation of the effect of helicopter design on brownout. A generic rotor is modelled and simulated in both hover and in forward flight above the ground. The disc loading of the rotor is altered as are various rotor design parameters such as the num-

ber of blades, twist and root cutout. By perturbing the geometric properties of the generic rotor, and observing the corresponding changes in the dust distributions that are generated, the sensitivity of the size and density of the dust cloud to each rotor parameter is examined.

Finally, in Chapter 7, conclusions from the presented research are drawn and recommendations for further work are proposed.

1.4 Work Published and Presented

Portions of the work presented in this dissertation have been published previously, either in peer-reviewed journals or conference proceedings. The description of the particle transport and entrainment models and the comparison between the dust distributions generated by the single rotor and tandem rotor configurations formed the basis of a paper that was presented at the 64th Annual Forum of the American Helicopter Society in Montréal in April 2008. This paper, with slight modifications, was published in the Journal of Aircraft in July 2009 [37].

The investigation of the differences in wake structure generated by the single rotor and tandem rotor configurations, and the connection between the rotor wake and dust distribution, was presented in September 2008 at the 34th European Rotorcraft Forum in Liverpool [38].

The effect of modifying the number of blades and the twist of the blades, as discussed in Chapter 6, formed the basis of the paper that was presented at the 35th European Rotorcraft Forum in Hamburg in September 2009 [39].

Chapter 2

The Vorticity Transport Model

2.1 Introduction

The flow environment in which helicopters operate is highly unsteady. Vorticity is shed and trailed into the rotor wake as a result of the generation of lift by the rotating blades of the system. In cases where the aircraft is in operation close to the ground, the geometry of the rotor wake can be altered by the ground plane. This change to the rotor wake and distribution of vorticity can affect the aerodynamic performance of the helicopter. The vorticity field produced by the rotors must therefore be represented correctly to allow the aerodynamics and dynamics of a rotor and fuselage within such an environment to be modelled accurately. Many aerodynamic problems can be modelled using Computational Fluid Dynamics (CFD) where the Navier-Stokes equations are solved numerically to evolve the flow field through time. In most cases these CFD techniques attempt to solve the equations of motion in terms of the primitive variables, pressure, density and velocity. These methods are known to suffer from numerical diffusion of vorticity which, when modelling the longer term behaviour of the flow field around a helicopter, reduces the accuracy of the solution. In a typical CFD method the volume surrounding the helicopter is discretised into a number of computational cells through which the solution to the equations of motion are advanced through time. The

numerical diffusion experienced within the calculations can be reduced by increasing the number of cells but because detailed simulation of rotorcraft wakes requires the vorticity to be conserved over long periods of time the increase in the number of cells required can result in the calculation becoming very computationally expensive.

A second approach to solving the Navier-Stokes equations, which overcomes the excessive dissipation of the vorticity found when using the primitive variable form, is to formulate the equations in a way that explicitly conserves the vorticity. This alternative method, in the form of the Vorticity Transport Model (VTM), has been used to carry out all the rotor simulations presented in this dissertation. This chapter describes the theory and numerical techniques which are implemented within the VTM.

2.2 The Governing Equations

The equations of motion of a fluid can be described in terms of pressure, density and velocity by considering the conservation of mass, and the interchange of momentum and energy of the system. The Navier-Stokes equations can thus be written in primitive variable form as

$$\frac{\partial}{\partial t}\upsilon + \upsilon \cdot \nabla\upsilon = -\frac{1}{\rho}\nabla p + \nu\nabla^2\upsilon \tag{2.1}$$

In developing this form of the equations it has been assumed that the flow field is incompressible so that the continuity of mass can be written simply as

$$\nabla \cdot \upsilon = 0 \tag{2.2}$$

For a large part of the flow field, the speeds at which helicopters operate mean this assumption is credible. The regions near the tips of the rotor blades, however, can experience compressibility effects due to their operation close to the speed of sound. These effects are accounted for in the VTM by the use of aerodynamic lookup tables. These tables provide

the aerofoil characteristics over a range of different Mach numbers allowing more accurate aerofoil data to be used in such regions.

As the VTM conserves vorticity explicitly and solves the Navier-Stokes equations in the vorticity-velocity form, Eq. 2.1 can be rewritten in terms of vorticity and velocity. Taking the curl of Eq. 2.1 results in the unsteady vorticity transport equation

$$\frac{\partial}{\partial t}\omega + \upsilon \cdot \nabla\omega - \omega \cdot \nabla\upsilon = \nu\nabla^2\omega \tag{2.3}$$

where the vorticity, ω, is defined as $\omega = \nabla \times \upsilon$. The evolution of the vorticity field is calculated in the VTM by advancing Eq. 2.3 through time.

With the assumption of the flow being incompressible, the velocity field has zero divergence and is therefore uniquely defined by the vorticity field. Taking the curl of the vorticity

$$\nabla \times \omega = \nabla \times \nabla \times \upsilon \tag{2.4}$$

which can be rewritten as

$$\nabla \times \omega = \nabla(\nabla \cdot \upsilon) - \nabla^2\upsilon \tag{2.5}$$

but as the flow field is assumed incompressible, substitution of Eq. 2.2 in to Eq. 2.5 results in the differential form of the Biot-Savart equation

$$\nabla^2\upsilon = -\nabla \times \omega \tag{2.6}$$

The solution to Eq. 2.6 is found using Green's theorem giving

$$\upsilon(x) = -\frac{1}{4\pi}\int_V \frac{(x-y)}{|x-y|^3} \times \omega(y)dy \tag{2.7}$$

The Reynolds numbers experienced in full scale helicopter flows are high which allows the flow to be assumed inviscid, i.e. $\nu = 0$. However, within the thin boundary layers

surrounding the lifting surfaces immersed within the flow the viscosity is not assumed negligible. The effects of these viscous regions on the flow are introduced using a source term, S_ω, on the right hand side of Eq. 2.3 so that the vorticity transport equation can be rewritten as

$$\frac{\partial}{\partial t}\omega + v \cdot \nabla\omega - \omega \cdot \nabla v = S_\omega \tag{2.8}$$

The source term accounts for the vorticity produced by lifting surfaces as they move through the flow. For the work presented in this dissertation, the lifting surfaces considered are the rotor blades.

2.3 The Vorticity Transport Model

The Vorticity Transport Model as first described by Brown [40] and further developed by Brown and Line [34] has been used to carry out the rotor simulations presented in this dissertation. An addition to the model has been made which allows the simulation of particle transport within the wake surrounding the rotor. This particle transport model was introduced to allow the VTM to simulate helicopters operating above dusty surfaces and so that the dynamics of the resulting dust cloud could be investigated.

The VTM is a finite volume based CFD model which conserves vorticity explicitly and advances it within the flow field under the action of the velocity field. In the VTM, numerical diffusion causes the vorticity to suffer from spatial smearing whilst the strength of the vorticity is maintained but this smearing is minimised by use of Toro's Weighted Average Flux (WAF) scheme [41] as described in § 2.3.2.2. The velocity field generated by the vorticity is calculated using Eq. 2.7. A Cartesian Fast Multipole Method (FMM) is used to lessen the number of cell-cell interactions that are to be calculated and thus reduces the computational costs of this calculation. Within the VTM the computational grid is essentially boundary free and an adaptive grid structure is used so that computational cells exist only in the regions of the flow where there is vorticity present. This use of an adaptive grid and the removal of

redundant cells increases the computational efficiency of the code and concentrates the computational resources on the areas of interest. The ground plane is represented by applying the zero through-flow boundary condition using the method of images.

The VTM has been used in previous studies to investigate the aerodynamics and dynamics of helicopters in a number of operational conditions. An initial study into rotor operations in ground effect was carried out by Whitehouse and Brown [21] as was an investigation in to the response of a rotorcraft as it interacts with the wake of another aircraft [42]. The VTM has been used further to examine the effects of the vortex ring state on the behaviour of rotorcraft [43, 44] and to investigate the aerodynamic interactions which occur between the rotor wake and the fuselage [35], main rotor and tail rotor [45] and within coaxial rotor systems [36].

2.3.1 The Computational Grid

As helicopters operate in three-dimensional space, the flow field around the rotorcraft in a numerical simulation must be discretised into a number of three-dimensional computational cells through which the solution to the fluid flow equations can be advanced. Within the VTM a Cartesian background stencil is used to represent the position at which each computational cell, with side Δ_0, can be located. The VTM is an Eulerian flow solver as the stencil is fixed in relation to the rotor hub. The number of possible cell positions provided by the stencil is infinite which allows the flow domain to extend indefinitely in all directions.

The development of the rotor wake is calculated according to Eq. 2.8 with the vorticity from the lifting surfaces within the flow being introduced to the computational grid through the source term, S_ω. To evolve the vorticity through the computational domain, the only cells required are those containing the vorticity and, due to the second order component of the WAF method, the two cells immediately adjacent to these. If a cell contains vorticity then new cells are created at the locations neighbouring this cell so that the vorticity can advect further at the next time step. In the same way, if a cell no longer contains any vorticity and

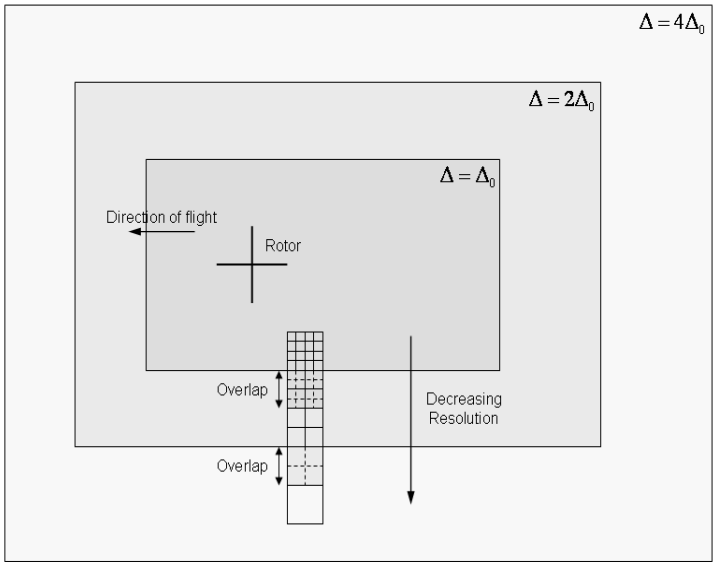

Figure 2.1: *Schematic diagram of the computational grid showing the arrangement of nested grid levels with varying cell size. Cell overlap required for the advection scheme is shown at the interfaces between grid levels.*

does not neighbour one which does, then this cell is destroyed. This creation and destruction of cells when required reduces the computational costs incurred.

As the grid is effectively boundary free, the number of cells could expand infinitely. This is protected against, however, to avoid the computation becoming far too expensive. To limit the total number of cells in the simulation, a nested grid structure is used where, at specified distances from the rotor, the resolution of the grid is reduced. The rotor is contained in the lowest grid level where the resolution is the same as that of the background stencil. Where specified, the resolution reduces with the cell edges doubling in length as shown in Figure 2.1. This process of doubling the cell size can be repeated indefinitely as the distance from the rotor increases but realistically only three or four levels are required to reduce the resolution sufficiently to keep resources concentrated within the regions of interest.

It is important that the conservative and monotonic properties of the advection scheme are preserved at the interfaces between the levels. This is achieved by extending the finer grid from the lower level and overlapping it into the next higher level grid as shown in Figure 2.1.

The flux of vorticity is then calculated on the overlapped finer grid and extrapolated onto the coarser grid. This method conserves the vorticity through changes in the grid resolution.

For the solution to advance in a stable manner through each timestep, the Courant-Friedrichs-Lewy (CFL) condition must be satisfied, that is $v\Delta t/\Delta x < 1$ where Δt is the computational timestep, v is the local flow velocity and Δx is the length of the computational cell on each grid level. As the cell size doubles at each change in grid level, the timestep used to advance the flow solution can be doubled and as a result the CFL number stays the same. Therefore as the number of grid levels increases the minimum timestep required to advance the solution also increases by a factor 2^i where i is the grid level ($i = 0, 1, 2...$), allowing fewer timesteps to be needed on the outer grid levels. This approach allows the computational resources to be focused on the most finely resolved parts of the domain closest to the rotor.

2.3.2 Numerical Implementation

The numerical methods and techniques used within the VTM to solve the governing equations and to evolve the resulting flow field through time are presented in the following section.

2.3.2.1 Discretisation of the Governing Equations

The governing equation for the transport of vorticity through a computational grid was introduced earlier as Eq. 2.8. The distribution of vorticity that is calculated is assumed to be uniform within each cell. By integrating spatially and temporally over the cell volume, V, and timestep, Δt, the discrete form of any flow variable, $q(x, t)$, can be defined by

$$[q]^n = \int_V q(x, n\Delta t_i)dx \tag{2.9}$$

and

$$[q]^n_{\Delta t_i} = \int_n^{n+1} [q]^n dt \tag{2.10}$$

where the term $\Delta t_i = 2^i \Delta t_0$ and accounts for the difference in timestep between the grid levels and n is the timestep ($n = 0, 1, 2...$). These definitions allow Eq. 2.8 to be rewritten in the discrete form

$$[\omega]^{n+1} - [\omega]^n = [\omega \cdot \nabla \upsilon]^n_{\Delta t_i} - [\upsilon \cdot \nabla \omega]^n_{\Delta t_i} + [S_\omega]^n_{\Delta t_i} \tag{2.11}$$

At the beginning of each timestep, $n\Delta t_i$, the Cartesian Fast Multipole Method is used to evaluate the velocity distribution within the flow, $\upsilon^n = \upsilon([\omega]^n)$, from the vorticity distribution, $[\omega]^n$. The vorticity distribution at time $t = (n+1)\Delta t_i$ can then be determined from the distribution at $t = n\Delta t_i$ using the operator splitting

$$\begin{aligned} [\omega]^* &= [\omega]^n + [S_\omega]^n_{\Delta t_i} \\ [\omega]^{**} &= [\omega]^* + [\omega \cdot \nabla \upsilon]^n_{\Delta t_i} \\ [\omega]^{n+1} &= [\omega]^{**} - [\upsilon \cdot \nabla \omega]^n_{\Delta t_i} \end{aligned} \tag{2.12}$$

where the stretching operator, $[\omega \cdot \nabla \upsilon]^n_{\Delta t_i}$ is evaluated using Runge-Kutta integration and the advection operator, $[\upsilon \cdot \nabla \omega]^n_{\Delta t_i}$, is evaluated using Toro's Weighted-Average-Flux (WAF) scheme [41] described in more detail in § 2.3.2.2. The construction of the vorticity field using the operator splitting approach is second order accurate in time as long as the approximation for each operator is also second order accurate in time [46].

2.3.2.2 The Advection Routine

Whilst calculating the advection of vorticity through the computational domain, it can suffer from spatial smearing due to numerical diffusion. As a result of this smearing, the vortical structures in the flow can become less compact. To overcome this, Toro's WAF scheme is

employed while calculating the flux of vorticity between cells using the advection operator, $[\upsilon \cdot \nabla\omega]^n_{\Delta t_i}$. By using Strang's method, [47], this three-dimensional operator can be broken down into three one-dimensional operators which, when integrated over the cell volume, gives

$$[\omega]^{n+1} = [\omega]^n - \frac{\Delta t}{\Delta x}(F_{k+1/2} - F_{k-1/2}) \tag{2.13}$$

for the flux of vorticity in one grid direction. Calculation of the flux of vorticity in the other two grid directions is essentially similar. The flux of vorticity through the left face and right face of the cell are $F_{k-1/2}$ and $F_{k+1/2}$ respectively and are shown schematically in Figure 2.2.

Toro's WAF scheme employs a Riemann based approach by considering the flux of vorticity as a wave of vorticity that arises at position $x_{k+1/2}$ and travels at a speed $\upsilon_{k+1/2}$, as shown schematically in Figure 2.3. The flux of vorticity is composed of two partial fluxes, $F^{(1)}_{k+1/2}$ and $F^{(2)}_{k+1/2}$. These partial fluxes are weighted by factors W_1 and W_2 which are the distances of the wave front at time $t = t^n_i + \Delta t_i/2$ from positions x_k and x_{k+1} respectively. These weighting factors are thus

$$\begin{aligned} W_1 &= \frac{1}{2}(1+\nu) \\ W_2 &= \frac{1}{2}(1-\nu) \end{aligned} \tag{2.14}$$

where $\nu = \upsilon_{k+1/2}\Delta t/\Delta x$ is the CFL number at the cell interface. The total vorticity flux is then

$$F_{k+1/2} = W_1 F^{(1)}_{k+1/2} + W_2 F^{(2)}_{k+1/2} \tag{2.15}$$

where the partial fluxes are given by

$$\begin{aligned} F^{(1)}_{k+1/2} &= \upsilon^n_{k+1/2}[\omega_k]^n \\ F^{(2)}_{k+1/2} &= \upsilon^n_{k+1/2}[\omega_{k+1}]^n \end{aligned} \tag{2.16}$$

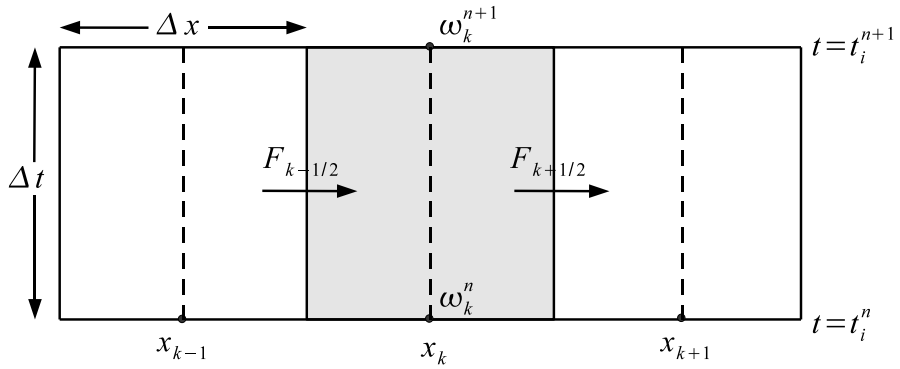

Figure 2.2: *Schematic showing the calculation of vorticity across cell faces.*

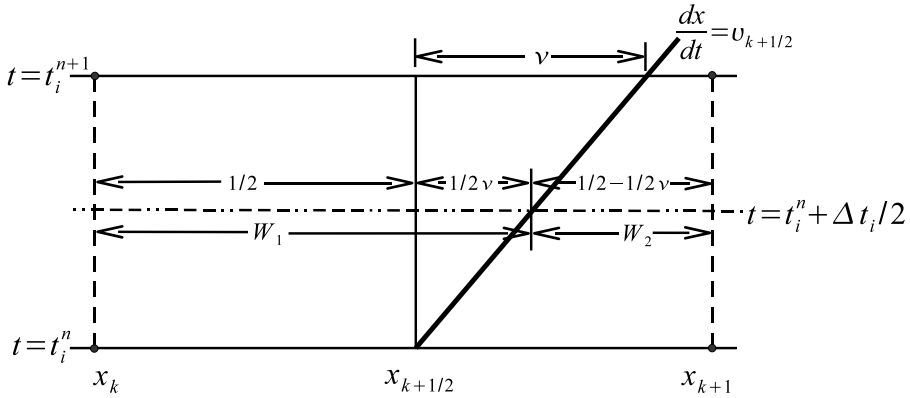

Figure 2.3: *Schematic showing the calculation of the weighting factors for the partial fluxes.*

As this scheme is second order time accurate, it can suffer from spurious oscillations in regions of high gradients of vorticity. To overcome this, wave amplifier functions are employed to ensure that the solution is Total Variation Diminishing (TVD) [48]. The Total Variation, defined in terms of a discrete vorticity field, is

$$TV(\omega^n) = \sum_{k=-\infty}^{\infty} |[\omega_{k+1}]^n - [\omega_k]^n| \tag{2.17}$$

and is essentially a measure of the oscillatory behaviour of the solution. For the scheme to

be fully TVD the amplifier functions must be chosen to satisfy the condition

$$TV(\omega^{n+1}) \leq TV(\omega^n) \tag{2.18}$$

Amplifier functions, ζ, are used to modify the weighting factors

$$\begin{aligned} W_1 &= \frac{1}{2}(1+\zeta\nu) \\ W_2 &= \frac{1}{2}(1-\zeta\nu) \end{aligned} \tag{2.19}$$

where

$$\zeta = \zeta(r^n_{k+\frac{1}{2}}, \nu) \tag{2.20}$$

and where r^n is the vorticity distribution ratio

$$r^n_{k+1/2} = \frac{[\omega_k]^n - [\omega_{k-1/2}]^n}{[\omega_{k+1/2}]^n - [\omega_k]^n} \tag{2.21}$$

The VTM uses a development of the SUPERA type amplifier function [48] to determine the value of ζ to use in the calculations.

2.3.2.3 The Velocity Field

For the WAF method to be used to calculate the vorticity flux into each cell, the velocities at the cell faces must first be known. These velocities are calculated within the VTM by approximating Eq. 2.7 as

$$\upsilon(x) \approx \int_V K_\delta(x,y) \times \omega(y) dy \tag{2.22}$$

where K_δ is the Rosenhead-Moore kernel [49, 50],

$$K_\delta(x,y) = -\frac{1}{4\pi}\frac{(x-y)}{(|x-y|^2+\delta^2)^{3/2}} \tag{2.23}$$

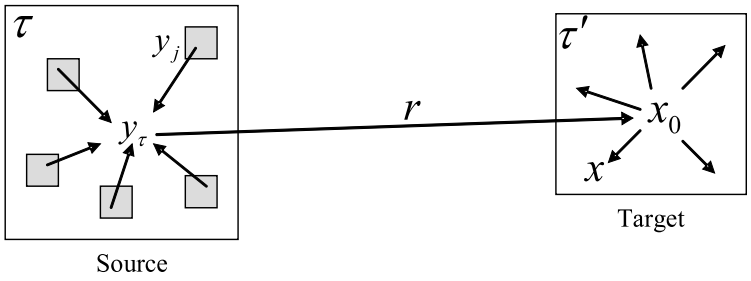

Figure 2.4: *Approximation of multiple cell cluster-cluster interaction using the multipole method.*

and replaces the Biot-Savart kernel in Eq. 2.7. The parameter δ is used to account for the fact that the vorticity is distributed uniformly in the cells rather than it being represented as a vortex singularity. The value of δ is chosen such that the maximum velocity induced by the vorticity within a cell is found at the faces of the cell.

If the solution to Eq. 2.22 was to be calculated simply by summing over all the computational cells then the computational costs would be $O(N^2)$, with N being the number of computational cells. The computational costs of the velocity calculation can be reduced to $O(N)$ by implementing the Cartesian Fast Multipole Method, [51], in which clusters of cells are formed to allow cluster-cluster rather than cell-cell interactions. When evaluating Eq. 2.22, the integral can be expanded using a truncated Taylor series. The order of truncation used in the expansion then determines the accuracy of this method. When using the FMM, clusters are formed by grouping together a number of cells. The effect of the cells within one cluster on another cluster can then be calculated assuming that the second cluster is well separated from the first. As the strength of the Biot-Savart interaction between clusters reduces quickly as the distance between the clusters increases, the computational cost of calculating the velocity can be reduced using the FMM in comparison to calculating the cell-cell interactions directly.

Figure 2.4 shows a representation of the cluster-cluster interactions implemented within the FMM. A number of cells, N_τ, are grouped together to form a cluster, τ. The centre of the cells in a cluster lie at y_j while the vorticity-weighted centre of the cluster is at y_τ. The

velocity induced in another cluster τ', which is well separated from τ, can be evaluated by considering the total vorticity contained in τ. Equation 2.22 can be rewritten in terms of the cluster structure as

$$\upsilon(x_0) \approx \sum_{j\in\tau} K_\delta(x_0, y_j) \times \omega_j \tag{2.24}$$

which can be expanded about the centre of the source cluster as a Taylor series

$$\begin{aligned} \upsilon(x_0) &\approx \sum_{j\in\tau} K_\delta(x_0, y_\tau + (y_j - y_\tau)) \times \omega_j \\ &\approx \sum_{j\in\tau}\sum_{k=0}^{\infty} \frac{1}{k!} D_y^k K_\delta(x_0, y_\tau)(y_j - y_\tau)^k \times \omega_j \end{aligned} \tag{2.25}$$

As the Taylor expansion is three-dimensional, the terms involved are vectors, so $k = (k_1, k_2, k_3)$, $k! = k_1!, k_2!, k_3!$, $D_y^k = \partial/\partial y_1^{k_1}, \partial/\partial y_2^{k_2}, \partial/\partial y_3^{k_3}$ and $x^k = x_1^{k_1}, x_2^{k_2}, x_3^{k_3}$ for $k_i \geq 0$. The subscripts $1, 2$ and 3 refer to the Cartesian directions. Truncating the series at the pth term gives

$$\upsilon(x_0) \approx \sum_{k=0}^{p} a_k(x_0, y_\tau) \times m_k(\tau) \tag{2.26}$$

and allows the velocity induced at x_0 by the vorticity in τ to be evaluated.

The range of the interactions in cluster τ is described by the tensor function

$$a_k(x_0, y_\tau) = \frac{1}{k!} D_y^k K_\delta(x_0, y_\tau) \tag{2.27}$$

The local distribution of vorticity within the cluster is given by the moments

$$m_k(\tau) = \sum_{j\in\tau} (y_j - y_\tau)^k \omega_j \tag{2.28}$$

The velocity induced at the centroid of the target cluster by the vorticity within the source cluster can then be calculated using Eq. 2.26. The saving in computational cost by using the FMM is achieved by obtaining the discrete velocities in the target cluster by using a truncated Taylor series expansion about the centroid of the cluster. For this calculation the

spatial derivatives of the velocity about x_0 must be known. The velocities at other positions, x, within the target cluster can then be approximated by using a series expansion about x_0,

$$\upsilon(x) \approx \upsilon(x_0) + \sum_{k=1}^{p} \frac{1}{k!} D_x^k \upsilon(x_0)(x - x_0)^k \tag{2.29}$$

where

$$D_x^n \upsilon(x_0) = (-1)^n \sum_{k=n}^{p} \frac{k!}{(k-n)!} a_k(x_0, y_\tau) \times m_{k-n}(\tau) \tag{2.30}$$

and is found by differentiating Eq. 2.26 with respect to x_0.

For the FMM to be implemented within the VTM the computational cells need to be grouped together in clusters. For this to be possible, it is required that an octree data structure be present within the code. In the octree structure the vorticity and velocity data is stored on levels similar to that of the adaptive grid described earlier. The individual cells which make up the grid are found at the lowest level of the structure. Eight individual child cells are then grouped together and assigned to a parent cluster on the next octree level. This process is repeated at the next level of the octree where eight of these clusters, now the children, are grouped together to form a further parent cluster. This operation is carried on throughout the grid until the whole domain is encapsulated by one parent cluster.

To calculate the velocity distribution throughout the grid, the FMM begins by first calculating the moments, as given by Eq. 2.28, in a sweep up through the octree structure from the individual cells to the overall parent cluster. After this, the FMM sweeps back down through the octree calculating the velocity on each level. To do this the velocity at cluster i on level n is taken to be composed of contributions from far field, intermediate field and near field velocities. The near field is made up of the clusters which directly neighbour the cluster i. The intermediate field is found from the neighbours of the parent cluster of i where all the children of the neighbours are intermediate field except for those that are in the near field. The far field is made up of the remaining clusters. This structure is demonstrated in Figure 2.5. For a cluster i, located on level n, the velocity due to the vorticity in the intermediate field

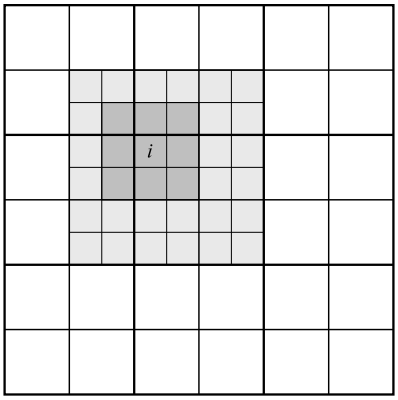

Figure 2.5: *Representation of the velocity field of cluster i showing the near field (dark grey), intermediate field (light grey) and the far field (white).*

can be calculated on level n using Eq. 2.26 to evaluate all the cluster-cluster interactions on that level. This can then be added to the velocity contribution from the far field calculated on level $n+1$ then translated to the children of i on level $n-1$ by means of Eq. 2.29. The far and intermediate fields of i then become the far field of the children of i while the near field becomes the intermediate field of the children. The calculation and translation of the velocity from the far and intermediate fields is done for all clusters on level n before moving on to level $n-1$. The contribution of the near field is not calculated until the lowest level of the octree has been reached. Once at the lowest level, the velocity contribution from the cells in the near field is calculated directly using the approximation of the Biot-Savart equation

$$v(x) = \sum_{j} K_{\delta}(x, y_j) \times \omega_j \tag{2.31}$$

and is then added to the velocity from the rest of the field. This combined velocity gives the overall velocity field required to allow the advection of the vorticity.

2.3.3 Blade Aerodynamics

As a rotor rotates within a viscous fluid, the movement of its blades through the fluid can result in vorticity being generated on the surface of the blades. This vorticity is a result of the

no slip condition on the rotor blades. Any variation in the lift produced along the spanwise direction of the blade will result in vorticity being trailed in the streamwise direction from the trailing edge of the blade. In addition to this, changes in local flow velocity will cause the chordwise distribution of vorticity to alter to the changing conditions and as a result vorticity will be shed along the span of the blade.

In deriving the vorticity transport equations earlier in § 2.2, it was assumed that the majority of the flow field is inviscid. In the thin boundary layers surrounding the rotor blades, however, viscosity does exist. The resulting shed and trailed vorticity produced by the blades is introduced into the flow through the source term

$$S_\omega = -\frac{d}{dt}\omega_b + \upsilon_b \nabla \cdot \omega_b \tag{2.32}$$

where ω_b is the bound vorticity and υ_b is the local flow velocity at a given point on the blade. The terms on the right hand side of the equation are the shed and trailed vorticity respectively.

The bound vorticity for use in the vorticity source term must be calculated and the VTM can employ a variety of different methods for doing this. Conventional CFD methods can be used to calculate the vorticity that would be shed and trailed from the rotor blades into the flow field, however, for present purposes a simpler approach is adopted to minimise the complexity of the calculation. For all the simulations presented in this dissertation, the Weissinger - L version of the lifting line model [52] is used to represent the aerodynamics of the rotor blades. This method is an approximation to the lifting surface method. Using the Weissinger - L model, the rotor blade is represented by a number of discrete bound vortex segments placed along the quarter chord line of the rotor blade. Along the three-quarter chord line lie collocation points, one corresponding to each bound vortex segment. A trailing vortex is produced from both ends of each bound vortex segment such that a horse-shoe of vortices is formed between the quarter chord and separation lines on the rotor blade as shown in Figure 2.6. The two trailing vortices are opposite in rotational sense to each

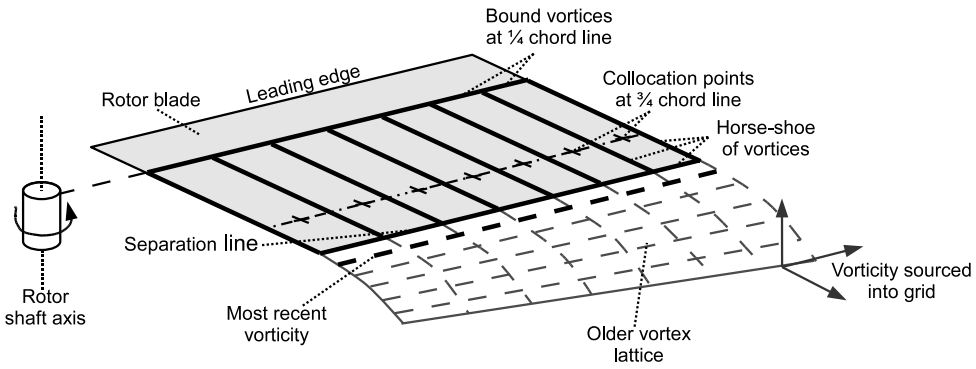

Figure 2.6: *Schematic of blade aerodynamics and vortex lattice produced in inner wake.*

other but are equal in strength to the corresponding bound vortex segment. For the vorticity field to be divergence free a fourth vortex must be shed from the blade into the free stream so that, when combined with the horse-shoe, a closed loop of vorticity is formed. This shed vortex is parallel to the separation line with its rotational sense being opposite to that of the corresponding bound vortex segment. The strength of the shed vortex equals the change in strength of the bound vortex over a finite time. The condition of zero through-flow of the local flow velocity normal to each collocation point can be used to calculate the strength of the corresponding bound vortex and thus the shed and trailed vortices.

The local flow velocity found at each collocation point is composed of the velocities due to the rotor wake and freestream, the structural motion of the blade and the velocities induced by the inner wake lattice of vorticity. The timescales associated with the high frequency dynamics and unsteady aerodynamics of the rotor blades are much smaller than those corresponding to the evolution of the rotor wake. This difference in timescales is overcome in the VTM by the introduction of a substepping approach where the global timestep, Δt, is divided into m substeps (where m is an integer). Using this approach, the evolution of the wake (the outer problem) is advanced by timestep Δt while the rotor blade (the inner problem) is advanced at timestep $\Delta t/m$. Within the inner problem, at each substep, an intermediate value of the source term is calculated. This intermediate source of shed and trailed vorticity is released into the flow at the separation line of the blade. The horse-shoe vortices

corresponding to each collocation point form a lattice as more vortices are released with each advancing substep (Figure 2.6). This vortex lattice is free to advect with the local flow velocity. After m substeps, the vorticity in the lattice is interpolated into the main grid of the outer wake problem where the total vorticity source, $[S_\omega]^n_{\Delta t}$, is then

$$[S_\omega]^n_{\Delta t} = \sum_{i=0}^{m-1} [S_\omega]^{n+i/m}_{\Delta t_i} \tag{2.33}$$

A large variety of aerofoil sections with differing aerodynamic characteristics are available for modelling helicopter rotors. When used in rotor simulations, these aerofoil sections operate over a range of angles of attack and Mach number. Without modification, the Weissinger-L approach predicts the lift-curve slope of a wing with infinite aspect ratio to be 2π. To obtain more realistic values for the dependence of lifting properties on angle of attack, the VTM implements aerodynamic look-up tables of the form $C_L(\alpha, M, Re)$. These more realistic lift characteristics are incorporated within the calculation by scaling the normal flow component at each collocation point. In effect, any loss of lift experienced by the aerofoil when operating in stalled conditions is modelled by reducing the normal component of the local flow velocity and therefore altering the strength of the corresponding bound vortex. As rotor blades often operate at high angles of attack and within regions of reverse flow on the retreating side of the rotor, the ability of this method to model the aerofoil properties around a full 360° is of great benefit. As the model is essentially inviscid and drag is not created directly, $C_D(\alpha, M, Re)$ and $C_M(\alpha, M, Re)$ are included in the look-up tables in a similar way to $C_L(\alpha, M, Re)$.

2.3.4 Structural Dynamics

In comparison to fixed wing aircraft, the dynamic system of a helicopter rotor is very complex. The rotor assembly consists of hinges which allow the rotor blades to flap normal to and lag parallel to the disc plane. Control inputs which allow the pilot to adjust the trajectory

of the aircraft by altering the pitch of the rotor blades are also required. A typical rotor head therefore consists of a number of hinges, linkages, springs and dampers which connect the rotor blades to the rotor hub. The centrifugal and Coriolis forces experienced by the rotating blades and the bending and twist of the blades contributes further to the complexity of the dynamics of real rotors. To simulate realistic rotor dynamic and aerodynamic behaviour, the detailed nature of the rotor assembly must be modelled correctly.

Within the VTM the structural dynamics of the system is approximated somewhat by employing a simplified model of the rotor system. For the results presented in this dissertation the rotor blades are modelled as rigid structures attached to the rotor hub with simple hinges, springs and dampers. The blades are then free to flap and lag in response to any forces they experience. If the motion of the rotor blades was simulated by solving the equations of motion of the blades directly then these equations would need to be altered with each rotor configuration that is simulated. To avoid the difficulties associated with this method, the VTM represents the motion of the blades using Lagrangian dynamics. This approach allows the dynamics of the rotor system to be represented in a generalised and adjustable manner which reduces the difficulties associated with modelling such complex systems.

The Lagrangian approach is based on defining the energies within the system, that is, the kinetic energy $T(q, \dot{q})$, potential energy $U(q, \dot{q})$, dissipation $D(q, \dot{q})$ and work done $Q(q, \dot{q})$, in terms of the n generalised coordinates $q = q(q_1, q_2, ..., q_n, t)$ describing the state of the system and their time derivatives $\dot{q} = dq/dt$ (where n is the number of degrees of freedom of the system). The Lagrangian of the system $\mathcal{L} = T - U$. Applying Hamilton's principle of minimisation of action results in the Euler-Lagrange equation

$$\frac{d}{dt}\left(\frac{\partial \mathcal{L}}{\partial \dot{q}_i}\right) - \frac{\partial \mathcal{L}}{\partial q_i} + \frac{\partial D_t}{\partial \dot{q}_i} = Q_i \tag{2.34}$$

where Q is the work done on the blades by the aerodynamics of the flow and D_t is the energy dissipation at time t as a result of non-aerodynamic damping in the system. Expansion of the

first term in Eq. 2.34 gives

$$\frac{d}{dt}\left(\frac{\partial \mathcal{L}}{\partial \dot{q}_i}\right) = \frac{\partial^2 \mathcal{L}}{\partial \dot{q}_i \partial \dot{q}_j}\ddot{q}_j + \frac{\partial^2 \mathcal{L}}{\partial \dot{q}_i \partial q_j}\dot{q}_j \tag{2.35}$$

which allows Eq. 2.34 to be rewritten as

$$\frac{\partial^2 \mathcal{L}}{\partial \dot{q}_i \partial \dot{q}_j}\ddot{q}_j + \frac{\partial^2 \mathcal{L}}{\partial \dot{q}_i \partial q_j}\dot{q}_j - \frac{\partial \mathcal{L}}{\partial q_i} + \frac{\partial D_t}{\partial \dot{q}_i} = Q_i \tag{2.36}$$

The accelerations, $\ddot{q}$, experienced within the system can be calculated directly using Eq. 2.36. The state of the system can then be advanced to the next timestep using the forward difference method

$$q^{n+1} = q^n + \dot{q}^n \Delta t \tag{2.37}$$

and

$$\dot{q}^{n+1} = \dot{q}^n + \ddot{q}^n \Delta t \tag{2.38}$$

2.3.5 Rotor Trim

To allow VTM simulations of helicopters to be representative of real helicopter flight conditions, the rotor must adjust to control inputs and be trimmed to specified targets. The VTM trim algorithm works by minimising the error between the predicted control values and required trim targets with the error being used to calculate the rate of change of each of the controls. The control inputs are the collective pitch and the longitudinal and lateral cyclic pitches so that $\theta = [\theta_0, \theta_{1s}, \theta_{1c}]$. Using this approach the rate of change of the control angles is

$$\tau \frac{d\theta}{dt} = F^\star - F(t) \tag{2.39}$$

where τ is a matrix of time constants, $F^\star$ is a vector of the specified target trim states and $F(t)$ is a vector of the current rotor states. The vector F comprises of the forces and moments

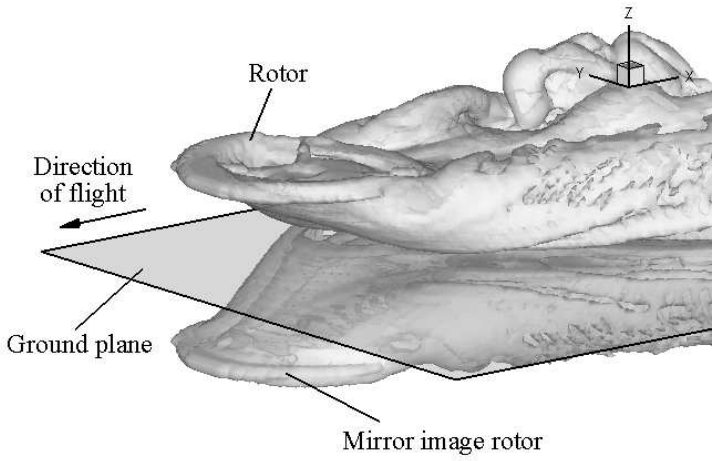

Figure 2.7: *Ground plane formed using method of images.*

on the airframe or the forces, the coning angle and the flapping angles of the rotor depending on the application. The controls are adjusted throughout a simulation with the rotor being considered to have reached a trimmed state when $\bar{F} = F^{\star}$, where $\bar{F}$ is the long term average of the forces and moments experienced by the rotor.

2.3.6 The Ground Plane

For the simulations presented in this dissertation, the ground plane is modelled in the VTM using the method of images. This method involves creating a mirror image of the rotor and its wake. The x and y components of vorticity in the mirrored wake are equal in both strength and direction to that within the original wake. The z component, however, is equal in strength but opposite in direction to that within the original rotor wake. This results in the ground plane being positioned half way between the two rotors as shown in Figure 2.7. The condition of zero flow through the ground plane is achieved using this method of images. The normal component of the induced velocity in the wake above and the wake below the ground plane cancel out. Using this technique the velocity induced by the vorticity in the rotor wake and its mirror image are calculated during the same timestep thus avoiding the convergence and ground penetration problems that can sometimes be associated with free-vortex wake

methods [32].

One benefit of employing the method of images is the ease with which it can be implemented. This method does however limit the ground plane to being a flat surface. If a more realistic ground plane was to be modelled, where there are variations in the height of the ground, then a more flexible approach such as a surface singularity method would be required. It should also be noted that the method of images represents an inviscid ground plane so that any flow features such as secondary and tertiary vortices which may be found if the effects of viscosity were included in Eq. 2.8 and the no-slip condition on the ground plane was implemented, are not captured using the present approach.

2.4 Summary

The governing equations and numerical methods used by the VTM to calculate the flow field around helicopters has been presented. The vorticity produced by the rotor blades, as calculated using the Weissinger-L version of the lifting line method, is convected through a structured Cartesian grid. The grid is adaptive so that cells only exist where there is vorticity present. Using a finite volume based approach, the evolution of the vorticity is calculated by the Navier-Stokes equations in the vorticity-velocity form. The vorticity is conserved explicitly with the effects of numerical diffusion being limited by the use of Toro's WAF scheme. The computational expense incurred during each simulation is reduced by forming clusters of grid cells on a number of grid levels and calculating the effect of the vorticity in one cluster on the velocity in another by using the Cartesian FMM. The VTM uses a Lagrangian dynamics method when modelling the rotor assembly so that the model is adjustable and different rotor configurations can be simulated with relative ease. The simulations are made to be representative of real helicopter flight by allowing the rotor control inputs to be modified throughout a simulation so that the rotor can be driven to a specified trim state.

Chapter 3

Verification of Ground Effect Predictions

3.1 Introduction

Before the VTM can be used with confidence to calculate the flow field around rotors in ground effect, the ability of the code to predict the behaviour of the wake of the rotors must first be shown. A number of flight tests and experimental investigations have been conducted previously in which various aspects of helicopter flight in ground effect have been studied, as outlined in Chapter 1. This previous work has provided a very useful set of data against which the predictions from the VTM can be compared. In this chapter both qualitative and quantitative comparisons are made between the results computed using the VTM and those found through experimental observations. The ability of the VTM to predict accurately the structures found within the wake of a rotor in ground effect and also the effect of the ground on the performance of the rotor is demonstrated.

3.2 Hover

When a rotor is hovering out of ground effect, the wake generated by the rotor blades is transported downwards and away from the rotor and thus has little effect on the operational

performance of the rotor. In ground effect, however, the ground plane obstructs the transport of the wake downstream of the rotor. Instead, as the wake approaches the ground plane it turns and travels radially outwards away from the centre of the rotor. The effect of the presence of a ground plane on the behaviour of the wake when a rotor is hovering above the ground as predicted by the VTM is compared to experimental observations.

3.2.1 Power Required to Hover

A number of studies have been conducted in which the effect of the ground on the power required by a hovering rotor has been investigated [12–15]. It was found that when a rotor is hovering above a ground plane, the power required to hover at a constant thrust reduces compared to the power that is required to hover out of ground effect. This reduction in power is most apparent when the rotor is at a height of less than one rotor diameter above the ground. Knight and Hefner [14] and Cooke and Fitzpatrick [53] both describe empirical models which relate the height of the rotor above the ground to the power required to hover. Hayden provides a comprehensive review [17] of the results obtained during flight tests and documents the power requirements of various different helicopters hovering at a range of different heights above the ground. In addition to this flight test data, Hayden also published an empirical correlation describing the power variation with rotor height above the ground. Comparing the predictions of the VTM with these empirical relationships and flight test data allows the ability of the VTM to predict the power required by a rotor hovering IGE to be verified.

To investigate how well the VTM predicts the power required to hover, a number of different rotors were simulated in hover at various heights above a ground plane. The power that was calculated was then compared to the flight test data of Hayden and to the empirical relations of Hayden, Knight and Hefner and Cooke and Fitzpatrick. The simulations were set up to represent the rotors of the AH-1G, CH-53E and OH-6A helicopters. A generic five-bladed rotor which was designed to be similar to the rotor of the EH-101, and a two-

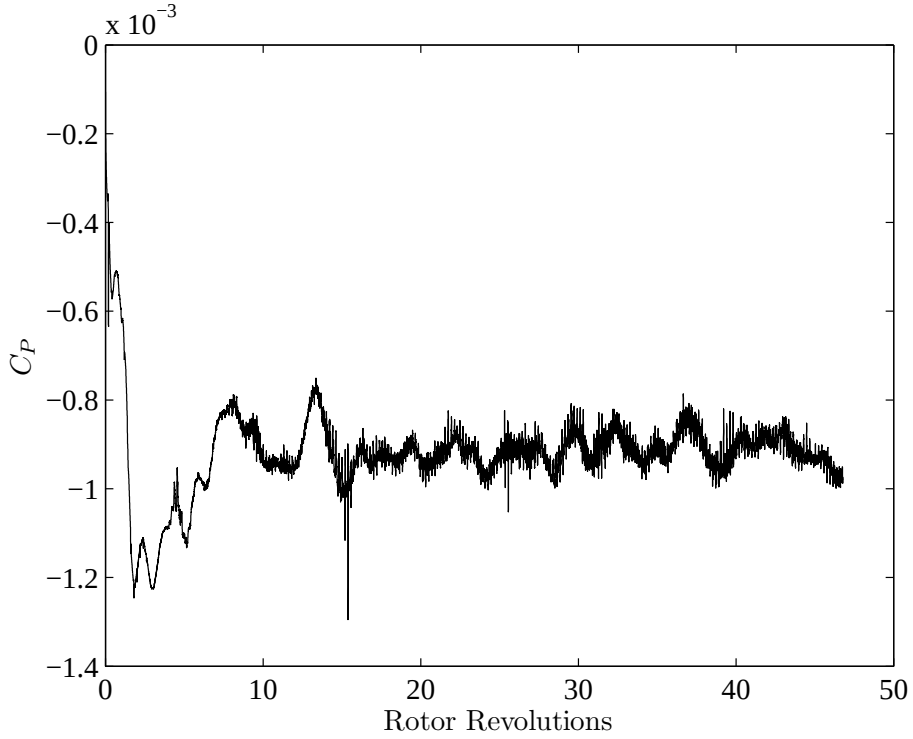

Figure 3.1: *Time history of the power required by a five-bladed rotor to hover at a constant thrust at a height of 0.75R above a ground plane.*

bladed rotor based on the rotor used in the experiments of Lee *et al.* [4], were also simulated. To examine the effect of the ground on the wake generated by the rotors in hover, all five rotors were simulated both in and out of ground effect. All the rotors were also trimmed to a constant thrust coefficient. The VTM predicts that the power required by a rotor in ground effect fluctuates over time. Shown in Figure 3.1 is the time history of the power required by the five-bladed rotor as calculated using the VTM. In the simulations presented in this dissertation, the start-up of the rotor is impulsive with the rotor operating immediately at its specified rotational speed. The initial transients of the system caused by the start-up of the rotor dissipate after approximately 20 rotor revolutions. The system then settles into its long-term behaviour. A true representation of the power required by the rotor can only be obtained once the transients have dissipated. Thus, the power requirements as calculated using the VTM are averaged over a large enough number of rotor revolutions, after the initial

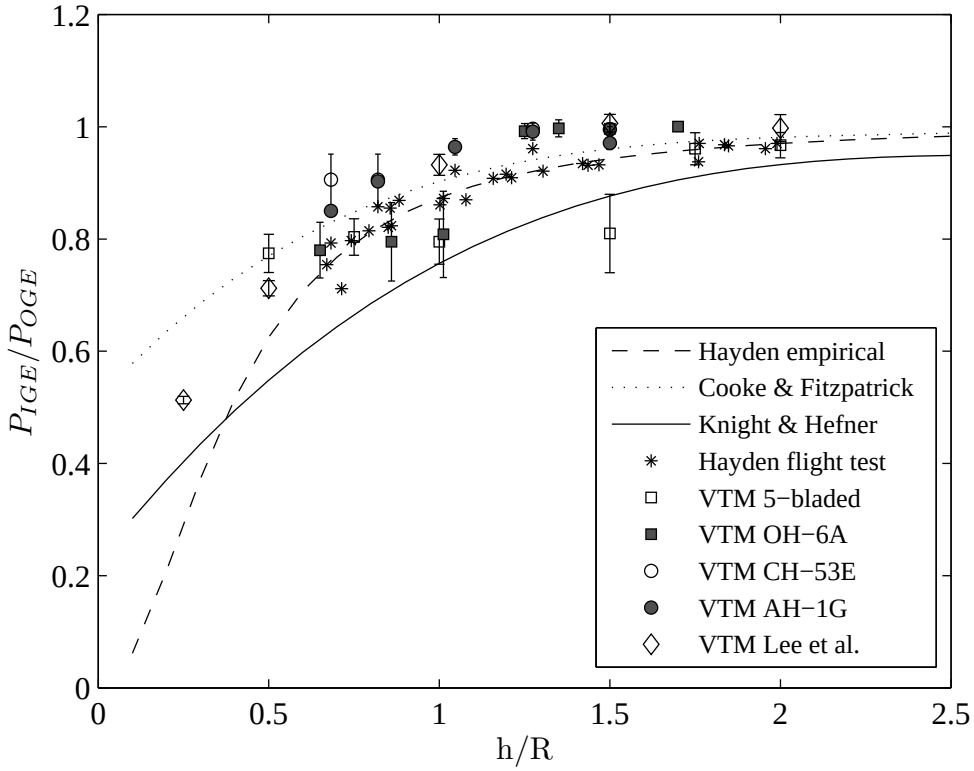

Figure 3.2: *Power required to hover IGE. VTM predictions for rotors operating at various heights above the ground compared to flight test data and empirical correlations.*

transients have settled, so that the long term average is revealed. The resulting power required IGE is then normalised by the power required by each rotor system OGE. The time averaged power requirements of the five different rotors, over a range of heights, as predicted using the VTM, are shown in Figure 3.2. Individual plots of the power required by each rotor are shown in Figure 3.3. The error bars represent the standard deviation of the power data about the average and thus give an indication of the unsteadiness of the rotor performance. Also presented in these figures are the empirical curves of Cooke and Fitzpatrick [53], Knight and Hefner [14] and Hayden [17] as well as flight test data for a number of different rotors that was documented by Hayden. The data points calculated using the VTM show the same trend, of increasing power with height, as the empirical curves but with some scatter in the data as the different rotors behave quite dissimilarly in some cases. The ratio of power IGE to power OGE is approximately 0.8 at a height of around $0.7R$ (where R is the rotor radius).

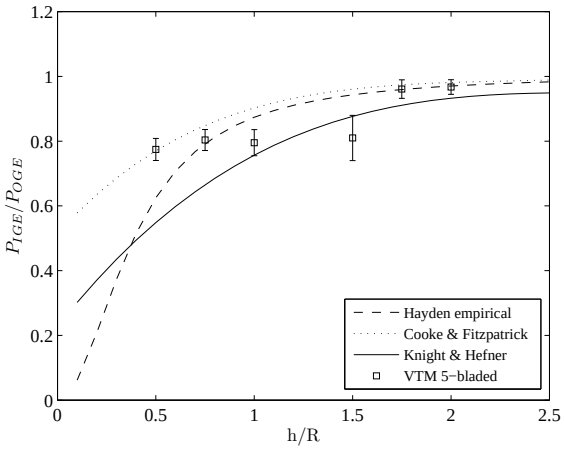

(a) *5-bladed rotor*

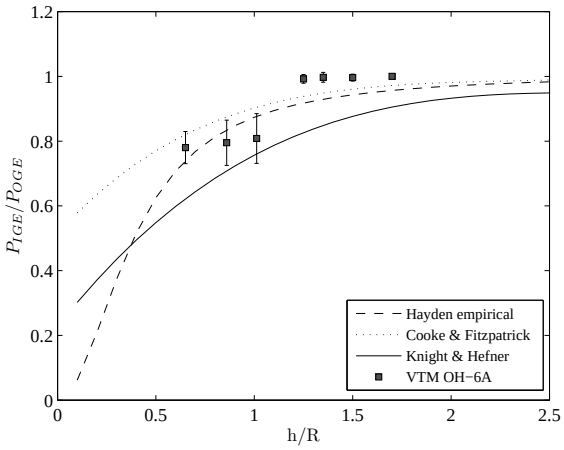

(b) *Rotor from the OH-6A*

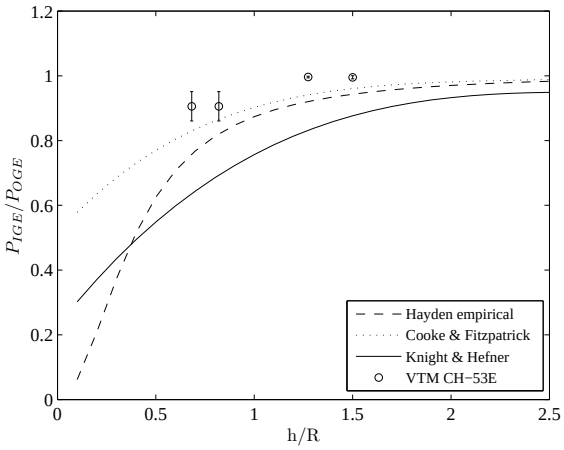

(c) *Rotor from the CH-53E*

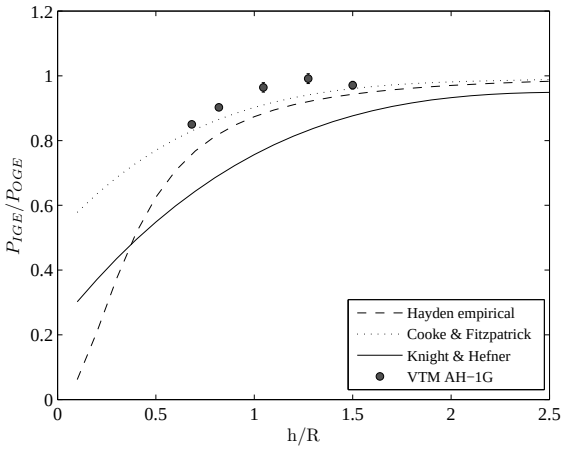

(d) *Rotor from the AH-1G*

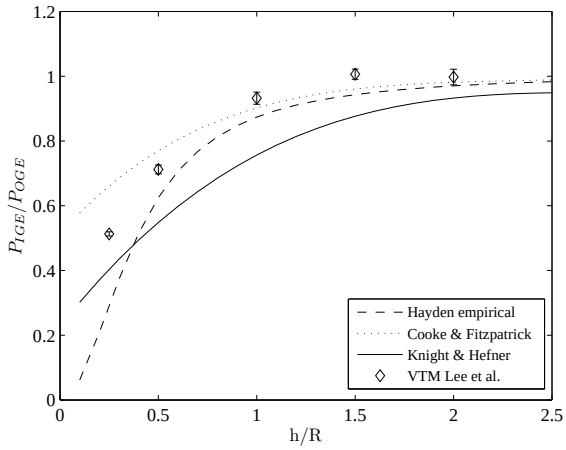

(e) *Rotor described by Lee* et al.

Figure 3.3: *Power required by five different rotors to hover in ground effect over a range of heights.*

As the height of the rotor above the ground increases, the effect of the ground on the power requirements of the rotor decreases and the power ratio tends towards unity. Figures 3.2 and 3.3 also show there to be a variation in the extent to which the ground affects the power requirements of different rotors. The effect of the ground on the power required by the AH-1G rotor, as shown in 3.3 (d), appears to be less than the effect the ground has on the OH-6A rotor, as shown in Figure 3.3 (b), particularly at the lower rotor heights. These differences in power are due to significant differences in the structure of the wakes that are formed by each rotor as is discussed in § 5.4.2.

The power comparison presented in this section shows the ability of the VTM to predict the changes in power associated with rotors hovering in ground effect but also reveals that there is a variation in the extent to which the ground affects the performance of different rotors. This variation between rotors will be investigated in more depth in Chapter 5.

3.2.2 Velocities within the Rotor Wake

During rotor flight IGE, the wake from a hovering rotor expands rapidly as it approaches the ground plane. An experimental investigation was conducted by Lee *et al.* [4] in which the expansion of the rotor wake, when in ground effect, was studied. The associated velocities within the wake were also examined. The experiment involved fixing a two bladed rotor, with a radius of 86mm and chord of 19mm, at a variety of heights above a ground plane to simulate a rotor hovering in ground effect. Flow visualisation, using mineral oil fog as a tracer, was used to examine qualitatively the dynamics of the flow field associated with this rotor while hovering in ground effect. To obtain quantitative information on the dynamics of the flow field, the flow velocities below the rotor were examined using digital particle image velocimetry (DPIV). Velocity profiles at a number of radial positions from the rotor centre were reported.

The VTM has been used to replicate the experiment of Lee *et al.* and comparison of the VTM results with those obtained through experiment allows the ability of the VTM to

predict the velocities within the flow field to be examined. As with the experiment, the rotor was simulated in hover at a range of heights above the ground. The rotor was trimmed to zero pitching and rolling moments and to the same thrust coefficient as was used in the experiment. The value of thrust used was dependent on rotor height as the power of the rotor was kept constant over the range of heights. Quantitative verification of the capabilities of the VTM when predicting the flow field below a rotor can be achieved by comparing velocity data found through experiment to the velocities calculated using the VTM.

Figures 3.4 - 3.6 show the time averaged profiles of velocity, as predicted by the VTM, compared to those obtained through experiment for a number of rotor heights above the ground. The velocity data is shown at three different radial positions of $0.8R$ (Figure 3.4), $1.0R$ (Figure 3.5) and $1.5R$ (Figure 3.6). The velocities are normalised by the estimated average induced velocity through the rotor OGE ($\upsilon_h = \sqrt{T/2\rho A}$). This was done to eliminate the effects of varying the thrust since the value of thrust to which the rotor was trimmed varied with the height of the rotor above the ground. In general, the velocities calculated using the VTM compare well to those obtained through experiment. The increase in velocity associated with the radial wall jet shown by experiment, which is most obvious when the rotor is higher above the ground plane, is also predicted by the VTM. The VTM does slightly underpredict the velocities within the flow field close to the ground plane when the rotor is at the greatest height, as seen in Figures 3.4 - 3.6 (a), and slightly overpredicts the velocities close to the ground plane when the rotor is at a height of $0.5R$ and $0.25R$ (Figures 3.4 - 3.6 (c) and (d)). When explaining these differences in velocity between the experimental data and that predicted by the VTM, the Reynolds number of the flow must be considered. The slight overprediction of the data when the rotor is simulated at the lower rotor heights could be due to the viscosity within the flow. The model rotor used in the experiment was very small resulting in the Reynolds numbers in the flow being quite low. This suggests that, to replicate the experiment exactly, a viscous flow field would have to modelled. The VTM assumes the flow field to be inviscid however, as described in § 2.2. This difference

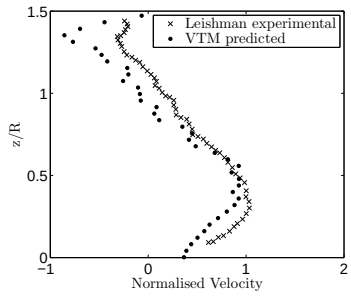

(a) *h/R = 1.50*

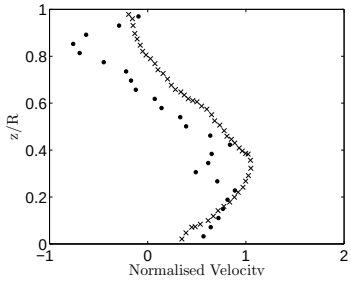

(b) *h/R = 1.00*

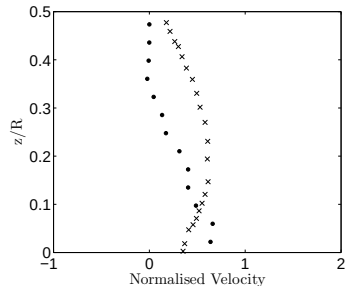

(c) *h/R = 0.50*

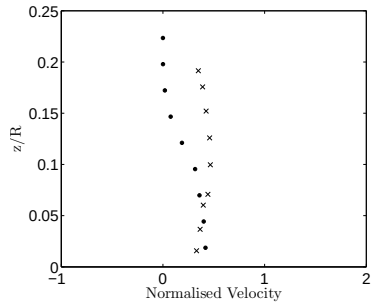

(d) *h/R = 0.25*

Figure 3.4: *Radial velocity profiles at* $x/R = 0.8$.

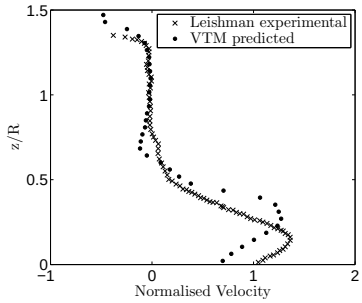

(a) *h/R = 1.50*

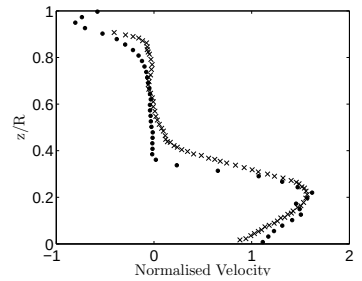

(b) *h/R = 1.00*

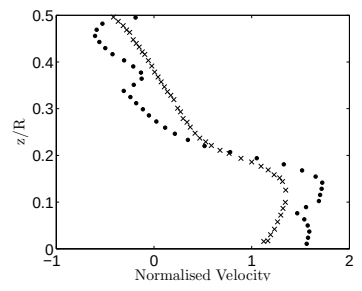

(c) *h/R = 0.50*

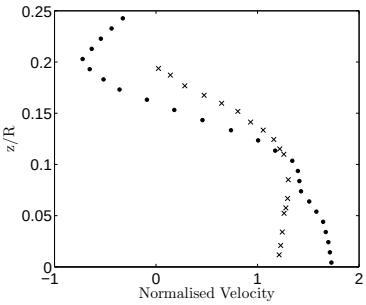

(d) *h/R = 0.25*

Figure 3.5: *Radial velocity profiles at* $x/R = 1.0$.

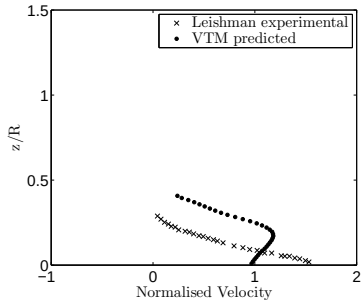

(a) *h/R = 1.50*

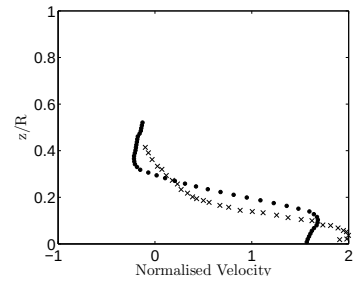

(b) *h/R = 1.00*

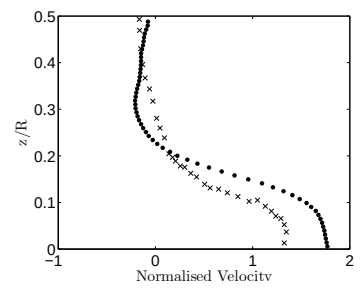

(c) *h/R = 0.50*

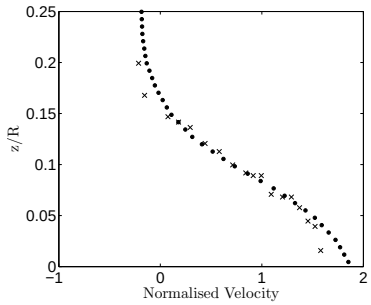

(d) *h/R = 0.25*

Figure 3.6: *Radial velocity profiles at* $x/R = 1.5$.

means that the viscous diffusion experienced by the rotor wake in the experiment causes the vorticity to diffuse thus weakening the velocity field more quickly than is predicted by the VTM. Another factor to consider is the way in which the ground plane has been modelled. The no-slip condition that would be present in the experiment is not simulated in the VTM. Thus, the secondary vorticity that would form at the ground plane in the experiment will not be predicted by the VTM. The lack of these additional vortical structures and thus the less complex behaviour of the wake close to the ground as predicted by the VTM may result in the velocities along the ground plane that are calculated using the VTM being slightly greater in many cases than found through experiment. At the greatest rotor heights and furthest outboard radial position the VTM is seen to underpredict the velocities within the rotor wake, however. This may be due to the simulation having not been run long enough for the wake to have developed fully at the outermost positions.

The discrepancies between the experimental and computational results are small however. This comparison nevertheless shows that the VTM is capable of predicting well the velocities within the flow field below a rotor operating in ground effect.

3.2.3 Tip Vortices

When using computational methods to predict the flow field surrounding a rotor, and particularly if there is interest in simulating particle entrainment, accurate prediction of the vortical structures found within the wake of the rotor, especially the tip vortices, must be achieved. Results as calculated using the VTM have been compared to results obtained from experimental studies to determine the ability of the VTM to predict such vortical structures within the rotor wake and to capture their positions.

3.2.3.1 Structures Within the Rotor Wake

In the experiment conducted by Lee *et al.*, as described in § 3.2.2, the flow field was visualised using mineral oil fog as a tracer. This visualisation revealed the main features present

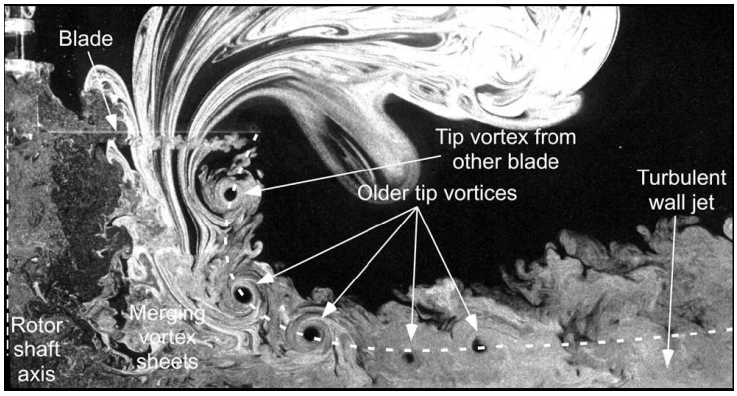

(a) *Smoke flow visualisation of the wake produced by a two bladed rotor in ground effect. Image taken from Lee* et al. *[4]*

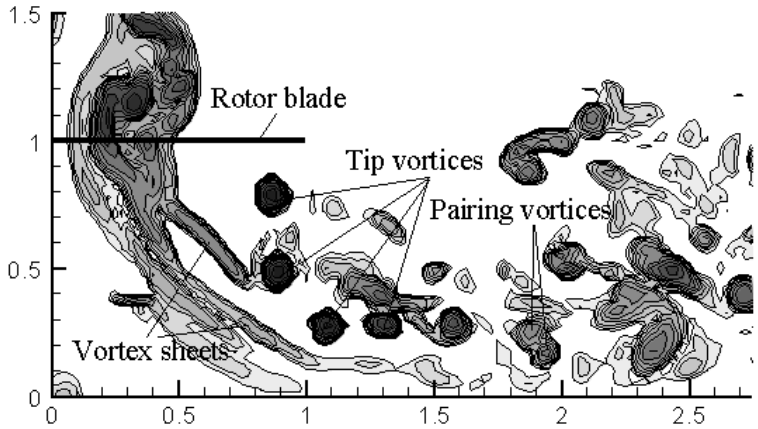

(b) *Vorticity distribution from a two bladed rotor in ground effect as calculated using the VTM.*

Figure 3.7: *Comparison of the experimentally observed and VTM predicted flow field produced by a rotor hovering at one radius above the ground.*

in the wake below a rotor hovering in ground effect. A qualitative verification of the computed flow field can be made by comparing the wake predicted by the VTM to that observed in the experimental flow visualisation. Snapshots of the flow fields generated in the experiment and as predicted by the VTM are presented in Figure 3.7. The snapshots show the wake on a vertical plane through the longitudinal centreline of the rotor. In both the experiment and the computation the rotor is positioned at a height of one rotor radius above the ground. The flow visualisation (Figure 3.7 (a)) shows that the most prominent features of the rotor wake are the tip vortices which are trailed from the rotor blades. The presence of the ground

plane causes these tip vortices to travel radially outwards away from the rotor as the wake approaches the ground. Also visible are the vortex sheets inboard of the tip vortices. Examination of the snapshot of the calculated rotor wake (Figure 3.7 (b)) shows these prominent features within the flow field also to be predicted by the VTM. As mentioned in § 3.2.2 the viscosity of the flow may have had a considerable effect on the wake that was generated during the experiment. Viscosity is not modelled in the VTM and, as a result, the vorticity does not diffuse as quickly as in the experiment. Thus, in the results of the VTM, the tip vortices exist as coherent structures for a slightly greater period of time. This preservation of vorticity also explains why the region of more turbulent vorticity, present beyond $x = 2R$, predicted by the VTM is greater in height than shown by experiment. This qualitative comparison between the structures found within the wake of a hovering rotor through experiment and as calculated using the VTM shows the VTM to be capable of predicting well the dominant features in the flow field below a hovering rotor.

3.2.3.2 Vortex Trajectories

When a rotor is operating above a ground plane, the trajectory of the tip vortices differs from the trajectory that they would follow with the rotor out of ground effect. As the tip vortices approach the ground, the axial descent rate of the vortices decreases while the radial distance of the vortices from the centre of the rotor increases. Further, quantitative, verification of the flow field calculated using the VTM can be obtained by comparing its prediction of the trajectory of the tip vortices generated by a rotor hovering IGE with experimental data provided by Light [28]. The data collected by Light was for a full scale Lynx tail rotor mounted above a ground plane. The distance between the rotor and the ground could be altered which allowed the tip vortex trajectories at various ground clearances to be recorded. The same four-bladed rotor was modelled using the VTM. The flow field produced by the rotor positioned at the same ground clearances as were defined by Light was calculated. At each different height above the ground the rotor was trimmed to zero disc tilt and to the same

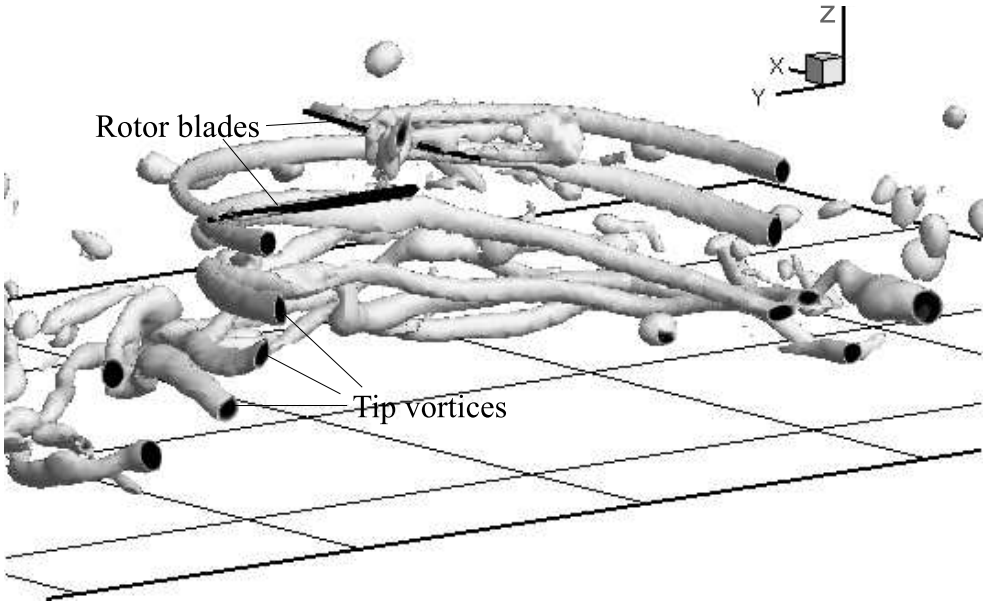

Figure 3.8: *Wake from a VTM simulation of Light's rotor hovering at a height above the ground of 0.84R. Wake is sliced through the centreline of the rotor to show positioning of the vortices.*

thrust coefficient as measured during Light's experiment. During the experiment a number of shadowgraph images were captured at each rotor height. The positions of the vortices on the shadowgraphs were obtained using semi-automated data reduction which allowed the axial and radial distances to the vortex positions to be recorded. When obtaining the vortex positions predicted by the VTM, the region of highest vorticity was selected as the centre of the vortex. These positions were extracted from a vertical plane through the centreline of the rotor. This somewhat subjective method of selecting the centre of the tip vortices may result in a slight discrepancy between the experimental and computational results. Figure 3.8 shows an example of the positioning of the tip vortices. Only half of the rotor wake is shown and the positions of the vortices on the plane through the centreline of the rotor are highlighted.

A comparison between the experimental data collected by Light and the tip vortex positions as predicted by the VTM is shown in Figures 3.9 and 3.10. The vortex locations extracted from the shadowgraphs are represented in the figures by small squares. It can be seen that there is some variability in the trajectory of the vortices, particularly at older wake

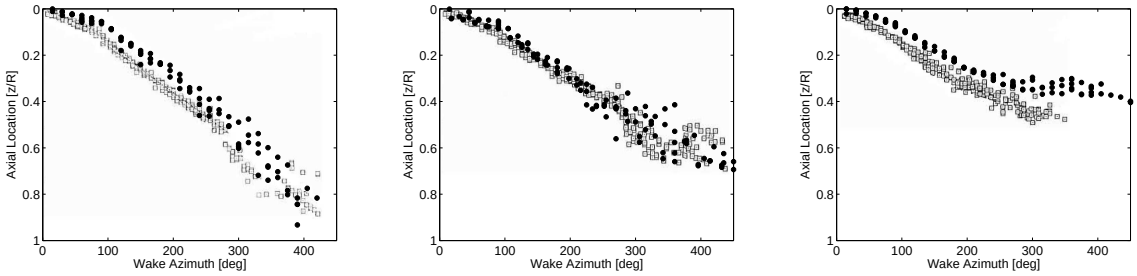

(a) *Rotor hovering OGE*

(b) *Rotor hovering at a height above the ground of 0.84R*

(c) *Rotor hovering at a height above the ground of 0.52R*

Figure 3.9: *Axial locations of the tip vortices produced by a hovering rotor. (Dark circles are data predicted by the VTM, squares are experimental data of Light.)*

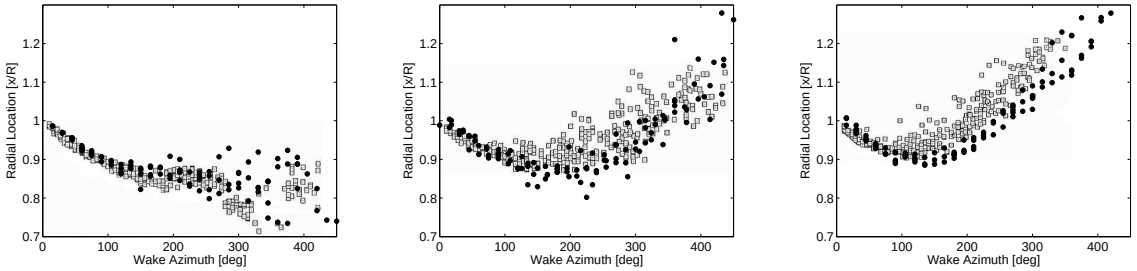

(a) *Rotor hovering OGE*

(b) *Rotor hovering at a height above the ground of 0.84R*

(c) *Rotor hovering at a height above the ground of 0.52R*

Figure 3.10: *Radial locations of the tip vortices produced by a hovering rotor. (Dark circles are data predicted by the VTM, squares are experimental data of Light.)*

ages. Thus, to investigate how well the VTM reproduces this fluctuation, the positions of the vortices, as calculated using the VTM, are recorded for a number of different instances in time. The vortex positions as predicted by the VTM are plotted as dark circles on top of the experimental data. In general the VTM predicts well the trajectory of the tip vortices in both the axial and radial directions. Examination of the axial location of the vortices shows that the descent rate of the vortices stays constant up to a wake age of 90° after which time the rate increases. The azimuthal position of this change in descent rate corresponds with the first blade passage of the four-bladed rotor. The descent rate is then constant until approximately 270° where, at this age, the trajectory of the vortices becomes more erratic than at earlier wake ages. Examination of the radial trajectory of the tip vortices for the rotor IGE

(Figure 3.10 (b) and (c)) reveals that the rotor wake contracts initially as is the case when the rotor is OGE (Figure 3.10 (a)). However, as the vortices approach the ground, the rotor wake expands. The VTM is shown to predict these features of the flow field and the vortex positions correspond well to those obtained through experiment. There is, however, a slight divergence of the computed data from the experimental data which occurs when the rotor is at a height of $0.52R$ above the ground and thus is in very strong ground effect. The rate of change of vortex position in both the axial and radial directions should be faster than is predicted by the VTM. This is particularly true after a wake age of 100°. A small divergence from the experimental data is also apparent in the axial direction when the rotor is out of ground effect. The overall results do, however, show that the VTM is capable of calculating with reasonable accuracy the trajectory of the tip vortices when the rotor is operated either in or out of ground effect.

3.3 Forward Flight

Up to now the effect of a ground plane on the rotor performance and behaviour of the wake of hovering rotors has been considered. However, the presence of a ground plane can also significantly alter the behaviour of the wakes that are generated by rotors operating at low forward flight speeds and close to the ground. The ability of the VTM to predict changes in wake structure and behaviour of rotors operating in ground effect can thus be examined further by comparing the predictions of rotors simulated in forward flight to observations made through experiment.

3.3.1 Flow Regimes

Sheridan and Wiesner [19] conducted wind tunnel experiments to examine the structure of the wake which forms below the front of a rotor during forward flight whilst operating in ground effect. They showed that a vortex exists which forms on the ground plane ahead of

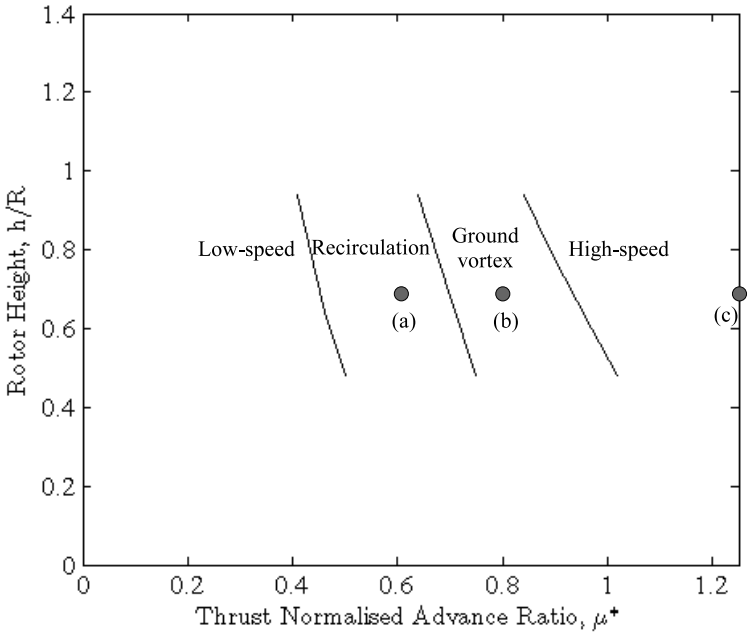

Figure 3.11: *Schematic showing the boundaries of the recirculation and ground vortex regimes. Positions (a), (b) and (c) correspond to the cases shown in Figure 3.12.*

the rotor in low speed forward flight. This vortex was found to move gradually aft of the rotor as the flight speed increases. A more detailed investigation was conducted by Curtiss *et al.* [20] in which an isolated four-bladed model rotor was moved through still air to represent a rotor in forward flight. They too found a vortex to form on the ground plane but described the flow field as existing in two distinct regimes - namely the recirculation regime and the ground vortex regime. The occurrence of these regimes was shown to be dependent on the advance ratio of the rotor and its height above the ground, as shown in Figure 3.11. At the lowest advance ratios the structure of the rotor wake is similar in form to that produced when the rotor is in hover, with the wake extending out along the ground plane in all directions around the rotor. A small increase in the advance ratio causes the extension of the wake in front of the rotor to decrease. By increasing the advance ratio towards $\mu^\star = 0.5$, the rotor enters the recirculation regime where circulation of the wake around the front of the rotor starts to occur. The rotor can be described as being within the ground vortex regime when, at approximately $\mu^\star = 0.7$, the wake no longer recirculates through the rotor disc but instead

forms a horseshoe shaped vortex on the ground plane below the front of the rotor. As the advance ratio is increased further, beyond $\mu^\star = 0.9$, the ground vortex moves below and to the aft of the rotor and subsequently is swept downstream resulting in the effect of the ground plane on the structure of the rotor wake being considerably weakened.

To investigate the ability of the VTM to capture the dependence of the structure of the wake on the forward speed of the rotor, simulations were run in which the experimental setup of Curtiss *et al.* was replicated. The structure of the wake that forms below the front of the rotor when operating at different advance ratios, as predicted by the VTM, is compared to the structure of the wake as described by Curtiss *et al.* The rotor was simulated at heights of $0.46R$ and $0.68R$ above the ground and over a range of thrust normalised advance ratios. The advance ratio is normalised using the rotor inflow velocity ($\mu^\star = \mu/\sqrt{C_T/2}$) to ensure that the gross characteristics of the flow, e.g. the skew angle of the wake, are maintained independently of the disc loading of the rotor. This normalisation allows the wakes produced at the same μ^* to be compared more directly than if the rotors were just simulated at the same μ. Figure 3.12 shows snapshots of the vorticity distributions within the flow at three different advance ratios with the rotor at a height above the ground of $0.68R$. These particular flight conditions are shown on the boundary plot in Figure 3.11. Figure 3.12 (a) shows the wake geometry at a low advance ratio and reveals significant recirculation of the wake through the front of the rotor disc. At the slightly higher advance ratio shown in Figure 3.12 (b), a much more stable ground vortex forms below the rotor. As the advance ratio is increased further, the ground vortex moves backwards below the rotor until it is eventually swept downstream to yield the wake geometry shown in Figure 3.12 (c). These changes in computed wake geometry are entirely consistent with the existence of the flow regimes that were described by Curtiss *et al.*, as shown in Figure 3.11, and thus show that the VTM, at least qualitatively, reproduces the expected transition between these different flow states as the forward flight speed of the rotor is increased.

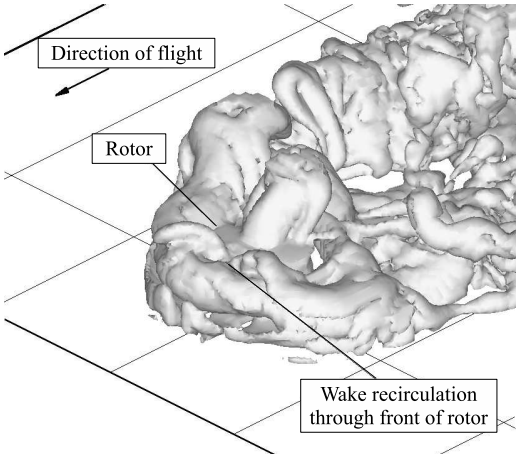

(a) *Recirculation regime ($\mu^\star = 0.61$).*

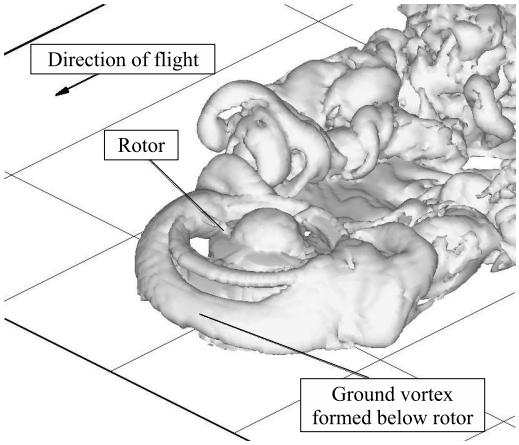

(b) *Ground vortex regime ($\mu^\star = 0.8$).*

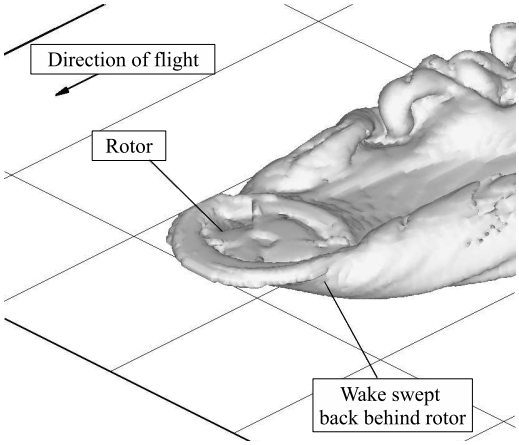

(c) *High-speed regime ($\mu^\star = 1.3$).*

Figure 3.12: *Rotor wake geometry at various forward speeds (rotor at height of $0.68R$ above ground.)*

3.3.2 Power Required in Forward Flight

The results of the previous section show that in forward flight, as the advance ratio of the rotor is altered, the geometry of the rotor wake changes. These changes in wake geometry in turn effect the performance of the rotor. In a previous study by Cheeseman and Bennett [16] it was reported that, during flight in ground effect, as the advance ratio of the rotor increases, the effect that the ground has on the power requirements of the rotor decreases. Thus, as the advance ratio increases, the power required to maintain a constant thrust also increases. Sheridan and Wiesner [19] also reported that the power required by a rotor to operate in ground effect is lower than that required out of ground effect. Numerous reports have also stated that, as the height of the rotor above the ground increases, the effect that the ground has on the power requirements of the rotor decreases. To investigate these changes in power required by a rotor operating in ground effect, the VTM was used to model an isolated, two-bladed rotor, based on that studied experimentally by Lee *et al.* [4] as described in § 3.2.2. The rotor was simulated at three different heights above the ground and over a range of advance ratios. The power required to maintain a constant thrust, as calculated using the VTM, was recorded for each flight condition and is shown in Figure 3.13. In this figure the power required by the rotor at each advance ratio and height IGE is normalised by the power that would be required for flight OGE at the same advance ratio. A superficial examination of the graph reveals the expected trend: as the advance ratio is increased, the power ratio tends towards unity as the effect of the ground reduces. The figure also shows the expected increase in the power required by the rotor when the operating height of the rotor is increased.

The change in power with forward speed for the rotor at a height of $0.5R$ above the ground is shown more clearly in Figure 3.14. The figure reveals a sudden jump in the power between $\mu^\star = 0.2$ and $\mu^\star = 0.3$. As the advance ratio increases from $\mu^\star = 0.3$ to $\mu^\star = 0.7$ the increase in power required is small. Further increases in forward speed beyond $\mu^\star = 0.7$ result in larger changes in power than the changes experienced at lower advance ratios (between $\mu^\star = 0.3$ and 0.7), and the power required IGE tends towards that required OGE.

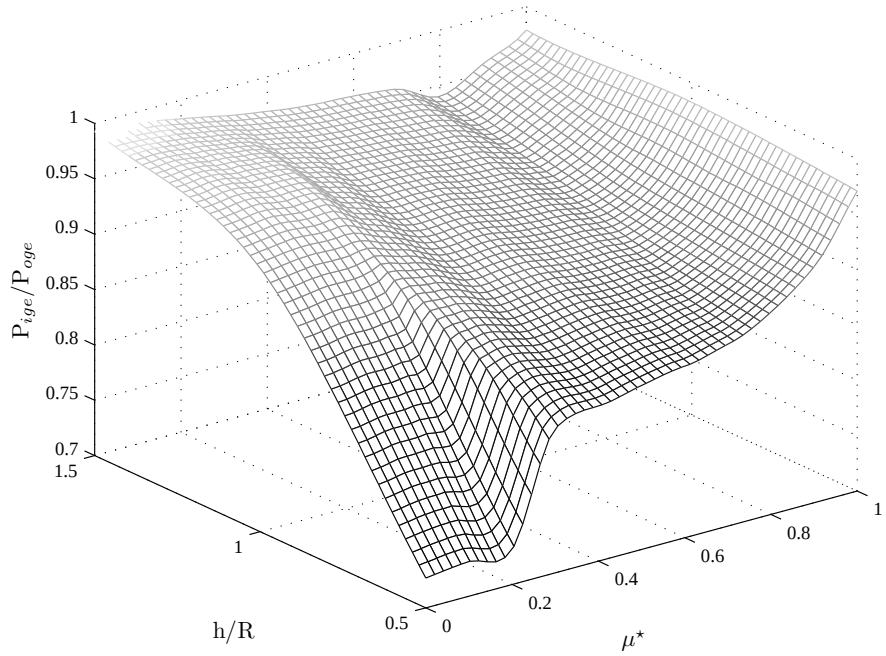

Figure 3.13: *Relation between rotor advance ratio and height above the ground and the power required to maintain a constant thrust, as predicted by the VTM, for the two-bladed rotor described by Lee* et al.

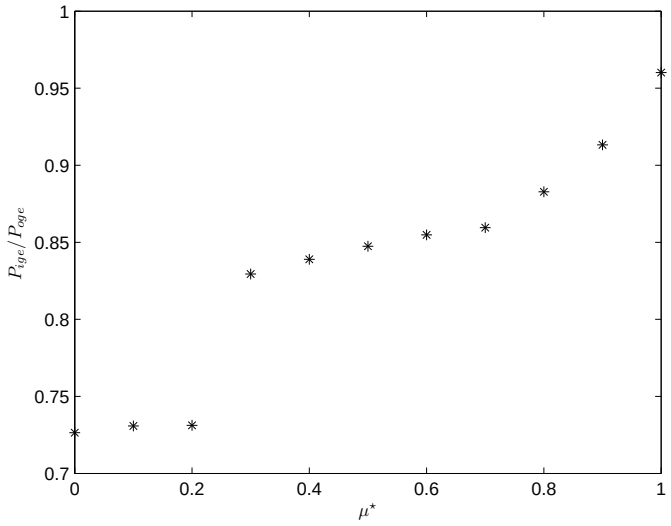

Figure 3.14: *Plot showing the development of the power required by Lee's rotor operating at a height of $0.5R$ above the ground as the advance ratio of the rotor increases.*

To explain these more subtle changes in power required, the development of the rotor wake, as the advance ratio increases, is shown in Figure 3.15. The figure presents the vorticity distribution around the rotor. The vorticity that intersects a plane through the longitudinal centreline of the rotor is shown. The vorticity shown has been averaged over approximately 30 rotor revolutions to reveal the dominant characteristics of the flow. When the rotor is in hover or travelling at very low advance ratio, the power requirements of the rotor are the lowest. The change in power with advance ratio can be explained by examining the development of the wake, as shown in Figures 3.15, and the corresponding velocity normal to the plane of the rotor disc, as shown in Figure 3.16. Figures 3.15 (a) to (c) show that, at the lowest speeds, the flow field extends some distance out in front of the rotor and that there is an upwards flow of vorticity through the centre of the rotor. This vorticity forms a large plume above the rotor disc. Examination of the velocity component normal to the plane of the rotor disc when the rotor is simulated at $\mu^* = 0.1$, shown in Figure 3.16 (a), reveals that this formation of the plume corresponds to a positive velocity up through the centre of the rotor disc. This positive velocity reduces the overall inflow through the rotor disc thus minimising the power required by the rotor. As the advance ratio increases (e.g. to $\mu^\star = 0.3$ as in Figure 3.15 (d)) the extent of the wake in front of the rotor reduces. The large region of vorticity above the rotor disc also reduces in size and streams back behind the rotor. At this advance ratio, on the region of the disc below the plume, the upwards velocity through the rotor disc reduces compared to that at the lower advance ratio while the downwards velocity increases (Figure 3.16 (b)). These changes in wake behaviour and velocity through the disc correspond with the jump in power shown in Figure 3.14. The changes in the wake behaviour with further increase in forward speed are more subtle. The extent of the wake in front of the rotor reduces further and forms a more compact and persistent ground vortex while the region of strong vorticity trailed from the rear of the disc gradually moves away from the ground plane. The vorticity that forms above the rotor disc concentrates into a smaller region and the upwards velocity through the rear of the rotor disc reduces. As the advance ratio is increased beyond $\mu^\star = 0.7$

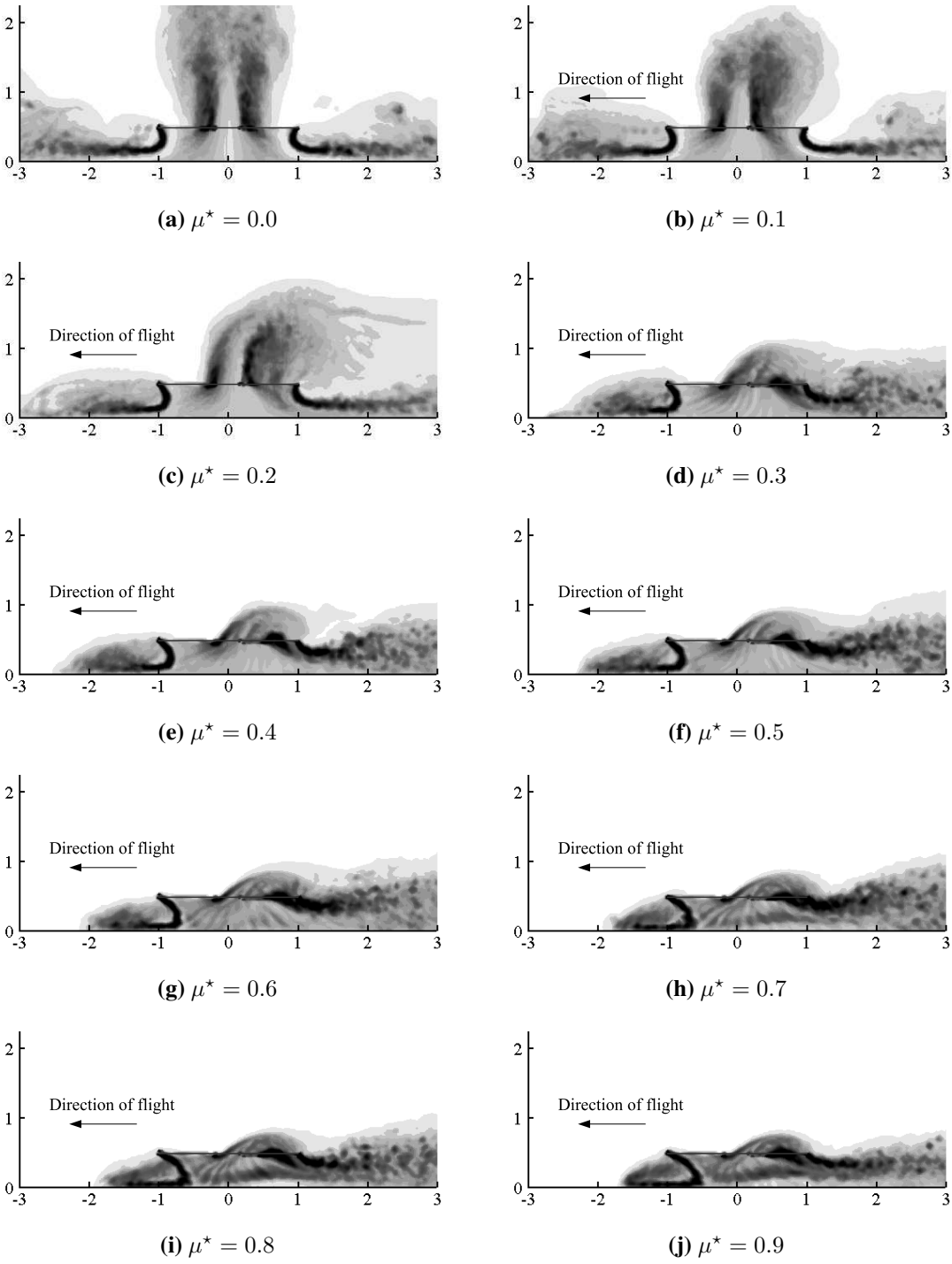

(a) $\mu^\star = 0.0$ **(b)** $\mu^\star = 0.1$

(c) $\mu^\star = 0.2$ **(d)** $\mu^\star = 0.3$

(e) $\mu^\star = 0.4$ **(f)** $\mu^\star = 0.5$

(g) $\mu^\star = 0.6$ **(h)** $\mu^\star = 0.7$

(i) $\mu^\star = 0.8$ **(j)** $\mu^\star = 0.9$

Figure 3.15: *Development of the wake around Lee's rotor operating at a height of $0.5R$ above the ground as the advance ratio of the rotor increases.*

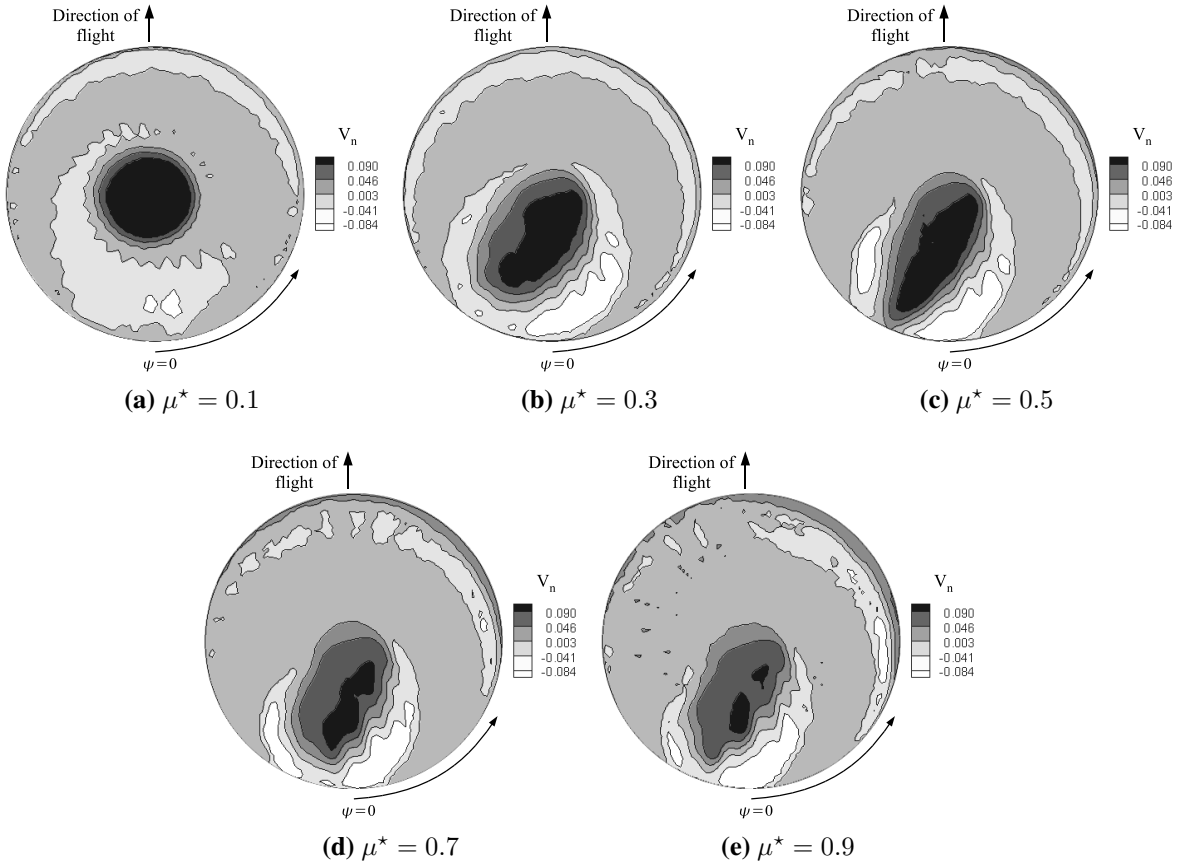

(a) $\mu^\star = 0.1$ **(b)** $\mu^\star = 0.3$ **(c)** $\mu^\star = 0.5$

(d) $\mu^\star = 0.7$ **(e)** $\mu^\star = 0.9$

Figure 3.16: *Velocity normal to the plane of the rotor disc as calculated by the VTM for Lee's rotor at a height of 0.5R above the ground. Darker contours represent positive velocity i.e. up through the rotor disc.*

(Figures 3.15 (i) & (j) and 3.16 (e)) the majority of the wake that forms above the rotor travels back down through the rear of the rotor disc. This transport of the wake increases the downwards component of velocity through the disc which indicates an increased inflow through the rotor disc, compared to lower advance ratios, and thus the power required by the rotor increases.

3.3.3 Rotor Trim

When operating a rotor in ground effect, the cyclic pitch angles required to trim the rotor are altered compared to those required when the rotor is operating out of ground effect. Figure 3.17 shows the lateral and longitudinal cyclic pitch angles required to trim the rotor

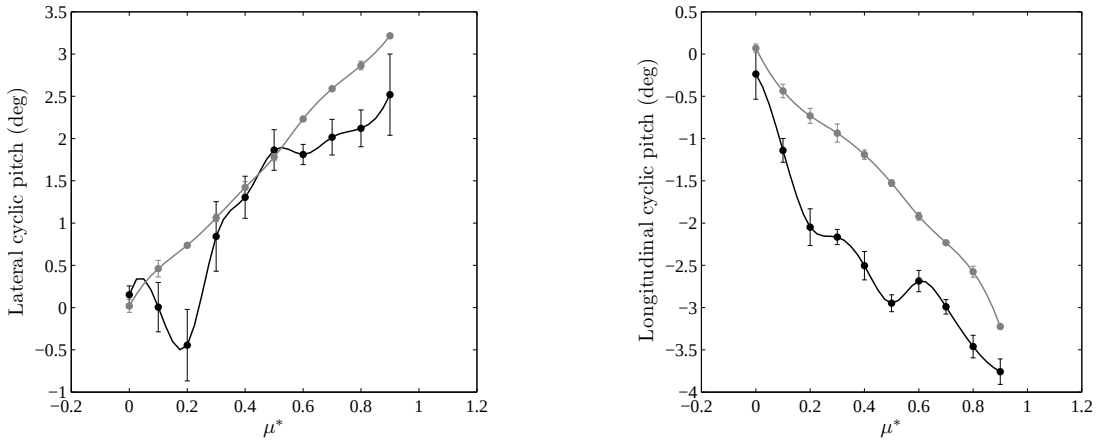

(a) *Lateral cyclic pitch* **(b)** *Longitudinal cyclic pitch*

Figure 3.17: *Lateral and longitudinal cyclic pitch angles for the rotor in forward flight. The grey line represents the cyclic pitches required OGE and the black line represents the cyclic pitches required IGE with the rotor at a height of 0.5R above the ground. Rotor trimmed to zero pitching and rolling moments.*

to zero pitching and rolling moments, when operating both in and out of ground effect, over the range of advance ratios that were shown in Figure 3.15. Out of ground effect, as the advance ratio of the rotor increases, there is an increase in the lateral cyclic pitch required to counteract the upwards flapping motion of the rotor blades on the retreating side of the disc. This upwards flapping motion is induced by rotor coning and the longitudinal inflow gradient that develops as a result of the induced velocities of the tip vortices. An increasing amount of longitudinal cyclic is also required to balance out the backwards flapping motion of the blades that would otherwise result from the imbalance in lift over the advancing and retreating sides of the disc. An example of the velocity distributions over the rotor disc when operating OGE is given in Figure 3.18 where the overall velocity components normal to and parallel to the disc, when the rotor is operating at $\mu^\star = 0.5$, are shown. In both plots, the velocity distribution is almost uniform and thus the required changes to the cyclic pitch angles are determined predominantly by the velocity of the oncoming flow and the change in the relative velocity of the blades around the rotor disc.

Unlike the cyclic pitch changes required by the rotor OGE, the changes in cyclic pitch

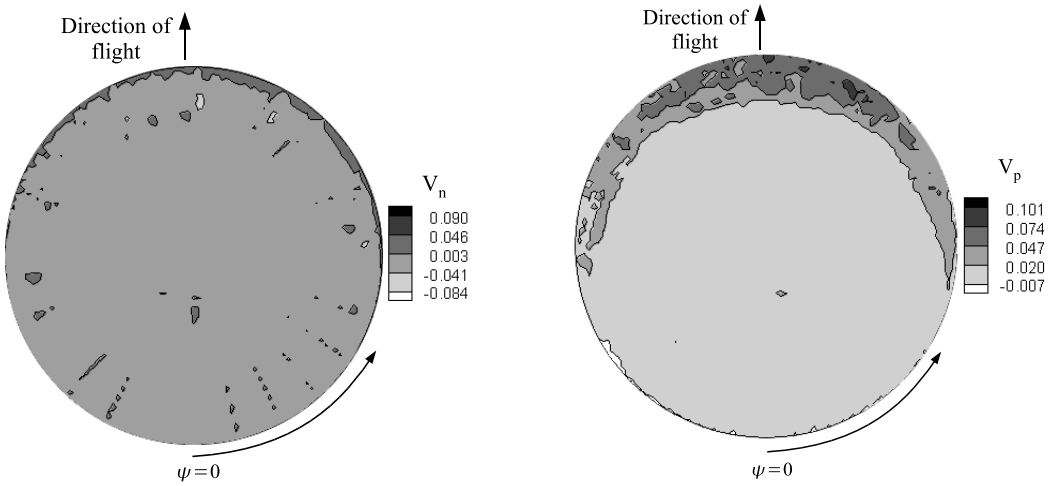

(a) *Component of velocity normal to rotor disc.*

(b) *Component of velocity parallel to rotor disc.*

Figure 3.18: *Components of velocity normal to and parallel to the rotor disc as calculated for Lee's rotor when operating OGE and at* $\mu^\star = 0.5$.

with advance ratio required IGE are not linear (Figure 3.17). Examination of the lateral cyclic pitch reveals that the pitch required to trim the rotor IGE is, in general, less than that required OGE. At the lowest advance ratios, the lateral cyclic pitch is affected by circulation of the wake through the front of the rotor disc. This circulation of the wake increases the inflow (Figure 3.16 (a) & (b)) and reduces the angle of attack of the blades around the front of the disc. Thus, a downward flapping motion on the retreating side of the disc would result if not counteracted by a reduction in the amount of positive lateral cyclic pitch required to trim the rotor. As the advance ratio increases, the plume of vorticity that forms above the disc significantly alters the flow field around the disc compared to the flow field that is generated around the rotor OGE (Figure 3.18 (a)). As shown in Figure 3.16 (b), the upflow from the plume moves over the rear of the disc. The greater forward speed also causes the plume to stream back towards the rear of the rotor and results in a region towards the very back of the disc through which the velocity of the flow is downwards. These flow patterns through the rear of the disc are primarily responsible for the changes in the lateral cyclic pitch angles as the advance ratio of the rotor increases. As the advance ratio increases beyond $\mu^\star = 0.5$,

a ground vortex forms below the front of the rotor. The induced velocity from this ground vortex reduces the inflow through the front of the disc, as shown in Figure 3.16 (c) to (e). This reduction in inflow results in an increase in the angle of attack of the blades at the front of the disc which would cause them to flap up over the retreating side if not counteracted by an increase in the positive lateral cyclic required to trim the rotor. However, this flapping motion is balanced out by the upflow through the rear of the disc. This upflow increases the angle of attack of the blades and causes them to flap up over the advancing side thus reducing the lateral cyclic pitch required to trim the rotor to zero rolling moment. A similar reduction in lateral cyclic pitch when operating in ground effect was reported by Sheridan and Wiesner [19].

The increase in longitudinal cyclic pitch required to trim the rotor IGE compared to that required OGE, as shown in Figure 3.17 (b), can be explained by examining the velocity of the flow parallel to the plane of the rotor disc. Out of ground effect, as the advance ratio increases, there is an increase in the longitudinal cyclic pitch required to trim the rotor due to an imbalance in lift experienced over the advancing and retreating sides of the disc. As shown in Figure 3.18 (b) the velocity distribution parallel to the rotor disc OGE is almost uniform and thus this difference in lift is due to the difference in the relative velocity of the blades as they travel around the rotor disc. A similar change in the relative velocity of the blades around the rotor disc is experienced IGE however the difference in velocity over the advancing side and the retreating side of the disc is exaggerated. Figure 3.19 shows the effect of the plume and ground vortex on the velocity parallel to the plane of the disc. These two wake structures increase the velocity over the front and rear of the disc. This increase in velocity, compared to that experienced OGE, results in a greater difference between the relative velocity of the blades over the advancing and retreating sides of the disc. This, in turn, results in a greater imbalance in the lift generated by the rotor IGE compared to the lift OGE and thus a larger longitudinal cyclic pitch is required to trim the rotor.

The results presented in this section show that the behaviour of the rotor wake in ground

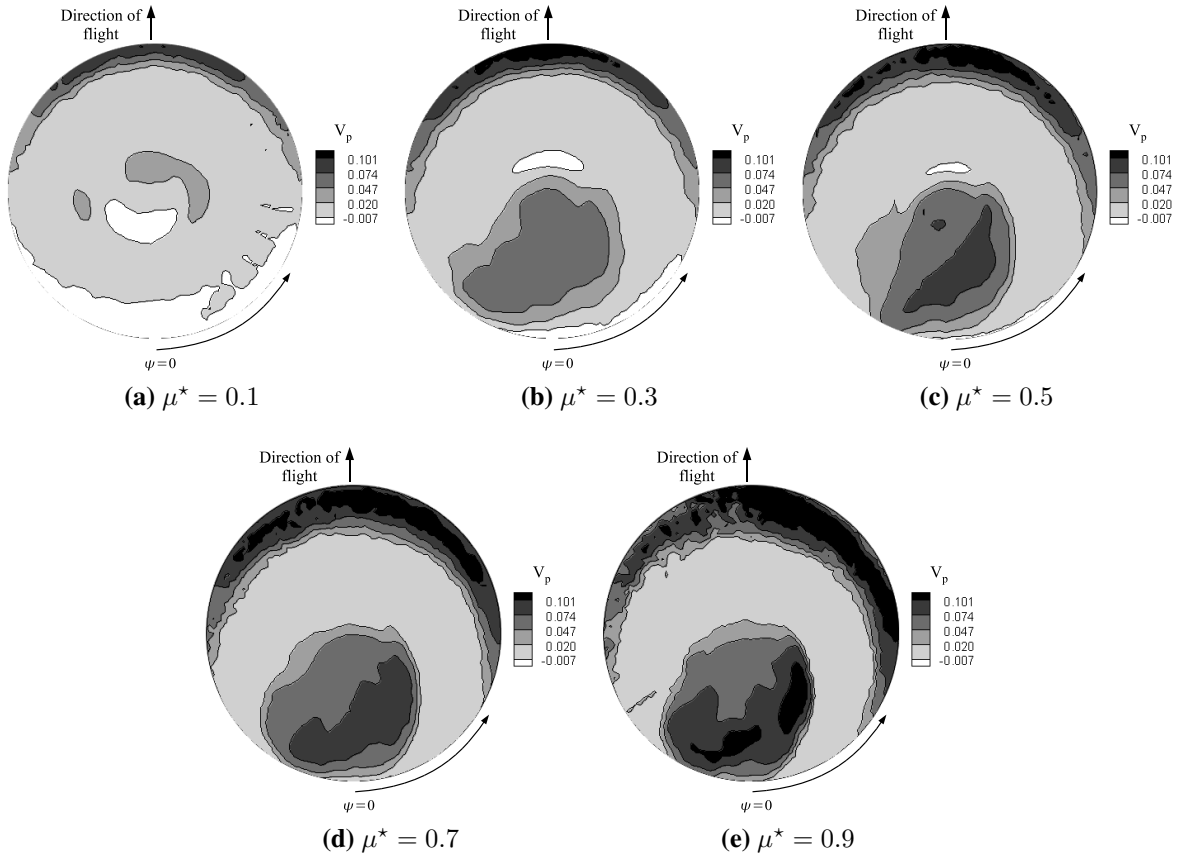

(a) $\mu^\star = 0.1$ **(b)** $\mu^\star = 0.3$ **(c)** $\mu^\star = 0.5$

(d) $\mu^\star = 0.7$ **(e)** $\mu^\star = 0.9$

Figure 3.19: *Overall velocity parallel to the plane of the rotor disc as calculated by the VTM for Lee's rotor at a height of 0.5R above the ground. Positive velocity is towards rear of rotor disc.*

effect during forward flight is very complex. The VTM has been shown, however, not only to be capable of predicting the expected changes in rotor wake geometry during forward flight, but also to capture changes in both the power requirements of a rotor and cyclic pitch angles required to trim the rotor while operating in ground effect.

3.4 Summary

By comparison with flight test and experimentally obtained data, it has been shown that the VTM is capable of predicting well the features associated with rotor flight close to the ground in both hover and forward flight. Qualitative comparisons have been presented which

highlight the ability of the VTM to predict the very detailed structures within the rotor wake. The verification was augmented by using available quantitative experimental data to allow the accuracy of the VTM in predicting both the trajectory of the tip vortices below a rotor hovering above a ground plane and the induced velocities within the wake to be investigated more rigorously. Good agreement between the computed and experimental data is found in both comparisons. Further results have shown that the VTM is capable of capturing the changes in power required by rotors when operating in ground effect but it has been revealed that the amount by which the power requirements change appears to be rotor dependent. The simulation of rotors in forward flight has shown that the VTM captures well the changes in the structure of the rotor wake that were described previously from experimental observations. The results from both the hover and the forward flight simulations provide confidence in the ability of the VTM to predict accurately the wake of a rotor when operating in ground effect which is essential for the correct modelling of brownout.

Chapter 4

Particle Transport Model

4.1 Introduction

When helicopters are operated at low speeds and close to the ground in dusty or snowy environments, there is a high possibility that the aircraft will suffer from the potentially dangerous condition known as brownout or whiteout. This condition occurs when particles of dust or snow are entrained by the rotor wake into the air flow surrounding the helicopter. Under certain flight conditions this entrainment can cause the pilot's view to become obscured, and this may result in a loss of situational awareness. To allow the VTM to simulate these conditions and to be able to predict the behaviour of the clouds of particles that can become entrained into the flow field, a model for the entrainment of the particles and transport within the air flow has been integrated into the VTM. This dissertation focuses on the evolution of dust clouds produced by helicopters in desert environments, thus, the particle entrainment and transport models that are integrated into the VTM are models which describe the behaviour of particles of dust. To simulate snowy environments, the entrainment model which determines how many particles enter the flow field would have to be modified to be representative of snow rather than dust. In this chapter the entrainment and transport models, used to simulate transport of particles within the flow field, is described.

4.2 Entrainment and Transport Models

When simulating the transport of particles within the flow field around a helicopter, there are two different methods that can be used. The first is a Lagrangian based approach in which the trajectory of individual particles are modelled, as described by Keller *et al.* [31]. In this approach, the dynamics of a large number of individual dust particles is tracked as they are carried along in the flow. The properties of the resultant dust cloud are then inferred from this representative set of particles. If an accurate measure of the dust density within the flow field is to be obtained then a very large number of particles need to be modelled thus resulting in this approach becoming very computationally expensive. The second method, and that which is adopted within the VTM, is to model the transport of particulates using an Eulerian based approach. In this method the dynamics of the particle distribution in the flow surrounding the helicopter is modelled directly, and the dust density distribution is evolved through time using suitable transport equations. This Eulerian formulation allows a particle transport model to be run alongside the VTM without excessive additional computational expense. The initial entrainment of the dust from the ground plane into the flow field is modelled using semi-empirical methods taken from the field of sedimentology. In this section the Eulerian based method of calculating particle transport is described as are the processes through which the dust is entrained into, and settles out of, the flow field.

4.2.1 Particle Transport

In the Lagrangian frame of reference, the dynamics of a single particle (with mass m) is given by Newton's second law

$$m\frac{dv_p}{dt} = F \tag{4.1}$$

where F is the force applied to the particle and v_p is the velocity of the particle. If gravity and aerodynamic drag are assumed to be the dominant forces on the particle, then Rayleigh's

expression

$$F(u) = -\frac{1}{2}\rho|u|u\frac{\pi d^2}{4}C_D + mg \tag{4.2}$$

provides a good approximation to the force experienced by the particle when aerodynamic lift is not a significant contributor. The diameter of the particle is d, and $u = v_p - v$ is the particle velocity v_p relative to the air velocity v. The drag coefficient C_D of the particle is generally a function of u (i.e. of the particle Reynolds number Re). When simulating the dust clouds that form around helicopters, the particle sizes of interest are in the range where Stokes' law holds. Thus, taking Stokes' well known expression for the drag of a sphere moving through a viscous fluid and including the force due to gravity, the overall force on a particle can be described by

$$F(u) = -3\pi\rho\nu ud + mg \tag{4.3}$$

Combining this with Eq. 4.2 results in $C_D = 24/Re$ for very small particles.

The most robust approach to deriving the equation that governs the transport of a large number of suspended particles in the ground or helicopter-fixed Eulerian frame of reference, results from adopting the formalism of classical statistical mechanics. Let the spectrum of particles within the flow be defined by some variable ς representing the 'species' of any particle as distinguished by its mass, size or other relevant physical characteristics. Define the particle probability density function as $\Phi(x, v, \varsigma, t)$ so that $\Phi(x, v, \varsigma, t)\Delta x\Delta v\Delta\varsigma$ is the probability of finding a particle of species within the range $\Delta\varsigma$ containing ς, travelling with velocity within the range Δv containing v, within the region of space Δx surrounding x at time t. As such, the probability density function Φ can be considered as a time-parameterised scalar function on the multi-dimensional phase space σ with coordinates (x, v, ς). Assume that the particles are sufficiently dilute once they are suspended within the air for collisions to be rare (so that the forces associated with collisions do not need to be accounted for) and so that the reaction of the particles on the air can be neglected. Assume also that the particles do not break up or merge so that the species distribution of the particles does not change with

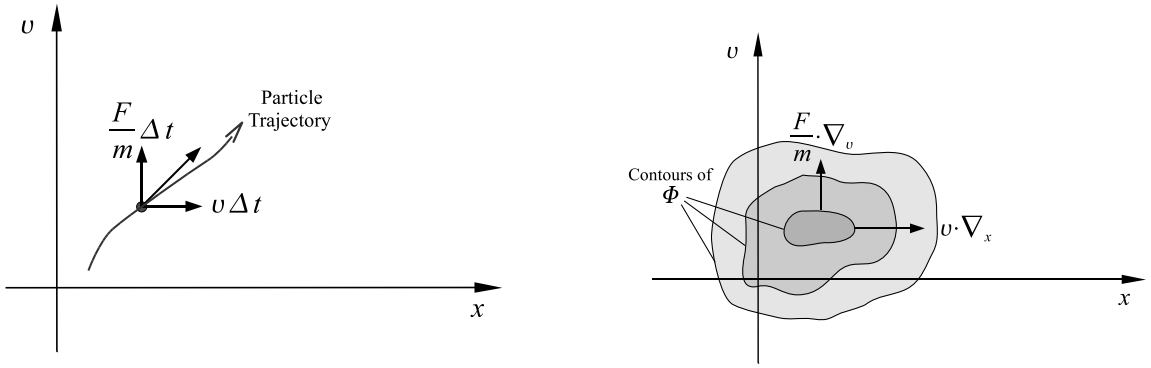

(a) *Schematic of Newton's second law expressed in terms of the trajectory of a single particle on the particle phase space σ.*

(b) *Schematic of Newton's law expressed in terms of the evolution of the probability density function Φ on the particle phase space σ.*

Figure 4.1: *Representation of Newton's law in terms of (a) a single particle and (b) the evolution of the probability density function Φ on the particle phase space.*

time. Newton's second law can then be expressed in terms of the evolution of the particle probability density function as

$$\Phi(x + v\Delta t, v + F\Delta t/m, \varsigma, t + \Delta t) = \Phi(x, v, \varsigma, t) \tag{4.4}$$

where $F(x, v, m)$ is the force experienced by a particle with mass $m(\varsigma)$ and velocity v travelling through the point x and is therefore given by Eq. 4.1. This evolution of the probability density function by Newton's second law is represented in the phase space σ as shown in Figure 4.1. Figure 4.1 (a) shows the evolution of a single particle in the flow field while Figure 4.1 (b) shows the evolution of the probability density function for an ensemble of such particles. It can be seen that changes in the location of the particle in the spatial (x) dimensions of phase space are due to the fluid velocity whereas changes in the location of the particle in the velocity (v) dimensions are due to the force on the particles. Using Taylor series, and considering that both x and v are vectorial in nature, expansion of Eq. 4.4 reduces to the Liouville equation, in the infinitesimal limit $\Delta t \rightarrow dt$,

$$(\partial/\partial t + v \cdot \nabla_x + F/m \cdot \nabla_v)\Phi(x, v, \varsigma, t) = 0 \tag{4.5}$$

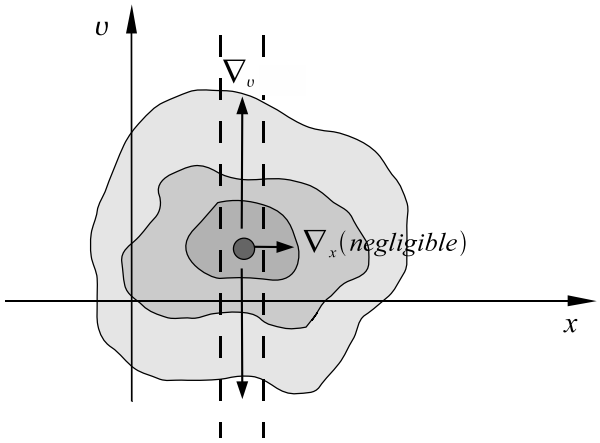

Figure 4.2: *Representation of the particle phase space showing a slice, parallel to the velocity dimensions, on which, over short periods of time, the change in Φ in the spatial (x) dimension can be assumed negligible in comparison to the change in Φ in the velocity (υ) dimension.*

For the purposes of predicting brownout, the assumption is then made that the evolution of the particle distribution is governed by two physical processes that have highly disparate timescales. Specifically, it is assumed that the convective motion of the particles as they are carried along by the air flow is slow compared to the accelerations of the particles in response to any imbalance in the forces acting upon them, or, in other words, if $\dot{u} \neq 0, \dot{u} \gg \dot{v}$ no matter what the acceleration of the flow $\dot{v}$. Given the structure of Eqs. 4.2 and 4.3 this assumption implies that the particles will remain in near equilibrium under the action of the aerodynamic forces that are generated by the particle as they move relative to the air (i.e. the dynamics of any individual particle is such that the net force F acting on any particle remains small). This near equilibrium assumption is justified later in the context of the typical particle sizes involved in creating the dust cloud that is responsible for brownout.

Over short periods of time, this assumption allows any changes in the particle probability density in the spatial dimensions of phase space, due to convection of the flow, to be assumed negligible in comparison to the changes in the velocity dimensions, that are due to the force on the particle (Figure 4.2). In the Eulerian frame of reference, the assumption of near equilibrium thus allows Eq. 4.5 to be factored into a 'fast' equation residing on the velocity

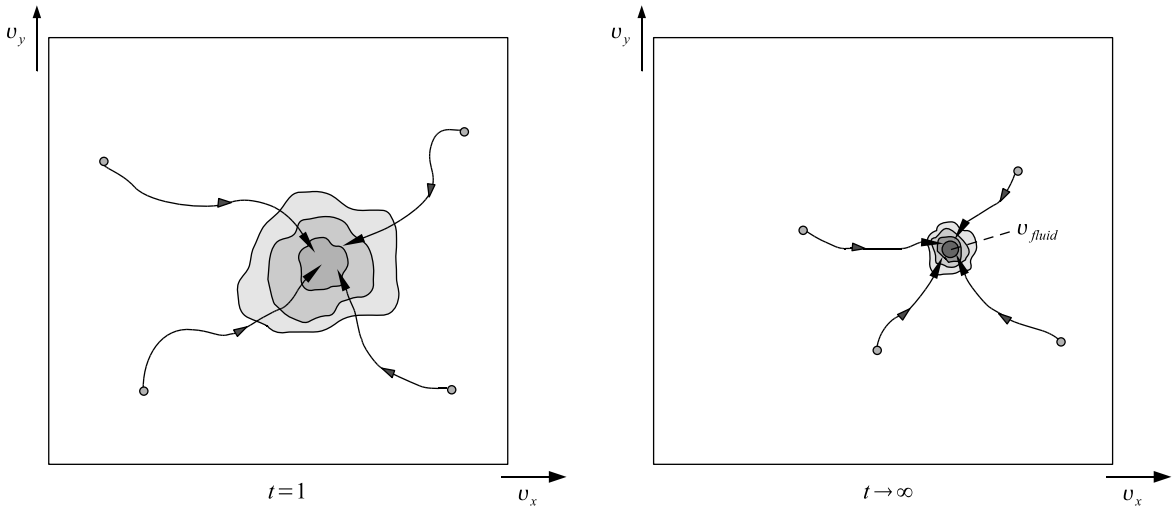

(a) *The initial particle probability density function on a slice parallel to the velocity dimensions of phase space will be spread out. Individual particle trajectories are governed by Newton's second law.*

(b) *As time proceeds, the particle probability density function, as governed by Eq. 4.6, concentrates more closely on the fluid velocity.*

Figure 4.3: *Schematic showing the evolution of the particle probability density function on the velocity dimensions of phase space. Through time, the particles concentrate on the flow velocity due to any imbalance in the forces acting on them.*

dimensions of σ, which accounts for the effect of the forces acting on the particles:

$$(\partial/\partial t + F/m \cdot \nabla_v)\Phi(x, v, \varsigma, t) = 0 \tag{4.6}$$

and a 'slow' equation residing on the spatial dimensions of σ, where the spatial convection of the probability density function is governed by the flow velocity:

$$(\partial/\partial t + v \cdot \nabla_x)\Phi(x, v, \varsigma, t) = 0 \tag{4.7}$$

To obtain a solution to the fast equation, the evolution of the particle probability density function in the velocity dimensions of the particle phase space, as represented by Figure 4.3, is considered. The evolution in this three-dimensional space is dependent on the force imbalance experienced by the particles, and on considering aerodynamic drag models of the form of Eq. 4.2 the force imbalance can be seen to reduce as the particle velocity approaches

the fluid velocity. The solution to the fast equation is thus a particle probability density function that concentrates ever more closely on the equilibrium Lagrangian particle velocity $\upsilon_p = \upsilon - \upsilon_g$ as time proceeds. That is, as $t \to \infty, \Phi(x, \upsilon, \varsigma, t) \to 0$ for all $\upsilon \neq \upsilon_p$. This equilibrium velocity can be defined by first considering the movement of a particle as described in a Lagrangian sense. Exact equilibrium of the particle is attained when the forces experienced by it become zero, i.e. from Eq. 4.3,

$$-3\pi\rho\nu(\upsilon_p - \upsilon)d + mg = 0 \tag{4.8}$$

Substitution for the mass of the particle allows Eq. 4.8 to be rewritten as

$$\upsilon_p - \upsilon = \frac{gd^2\rho_s}{18\nu\rho} \tag{4.9}$$

The right hand side of the expression is Stokes' settling velocity of a particle falling through a viscous fluid under the action of gravity. The particle equilibrium velocity can then be written as $\upsilon_p = \upsilon - \upsilon_g$, where υ_g is the 'fallout velocity' of the particle due to gravity. The solution to the fast equation can be returned to the full phase space σ by reintroducing the spatial dimensions x and using the slow equation to represent the convection of the particles.

Given any function $\psi(x, \upsilon, \varsigma, t)$ defined on the particle phase space, the projection operator Π, from phase space to physical space, can be defined by

$$\Pi\psi(x, \Sigma, t) = \int_{-\infty}^{\infty} \int_{\varsigma^-}^{\varsigma^+} \psi(x, \upsilon, \varsigma, t) d\varsigma d\upsilon \tag{4.10}$$

where $\Sigma = [\varsigma^-, ..., \varsigma, ..., \varsigma^+]$ is the band within which the species of interest exists. Thus the number density of particles at point x in the flow with a species within the band Σ can be obtained from the particle probability density function as

$$\rho_p(x, \Sigma, t) = \Pi\Phi \tag{4.11}$$

Applying the projection operator to the slow component, Eq. 4.7, of the Liouville equation gives

$$\Pi\left(\frac{\partial}{\partial t} + v \cdot \nabla_x\right)\Phi = 0 \tag{4.12}$$

which, since Π is linear, can be expanded as

$$\frac{\partial}{\partial t}\Pi\Phi + \Pi(v \cdot \nabla_x \Phi) = 0 \tag{4.13}$$

From Eq. 4.11 the first term in this expression is simply $\partial\rho_p/\partial t$. By the Midpoint Theorem the second term can be written as

$$\bar{v} \cdot \nabla_x \Pi\Phi + \Pi(v' \cdot \nabla_x \Phi) \tag{4.14}$$

which then reduces to

$$\bar{v} \cdot \nabla_x \rho_p + \Pi(v' \cdot \nabla_x \Phi) \tag{4.15}$$

where the species-dependent ensemble velocity

$$\bar{v}(\Sigma) = \frac{\Pi(\Phi v)}{\Pi\Phi} \tag{4.16}$$

Given the structure of the solution to the fast component of the Liouville equation, for a system of particles close to equilibrium, the Lagrangian equilibrium velocity, $\upsilon_p(\Sigma)$, for the particles with species ς is a very good approximation to $\bar{v}(\Sigma)$. This allows the first term of Eq. 4.15 to be interpreted as representing the convection of the particle distribution by the air flow under conditions of force equilibrium. Figure 4.4 represents the trajectory of the particle distribution at the equilibrium fluid velocity as calculated using the slow equation. Figure 4.4 (a) shows slices parallel to the velocity dimensions of the particle phase space, on which the changes in Φ in the spatial dimensions can be assumed negligible. On these slices the particle probability density function moves towards the equilibrium velocity as governed

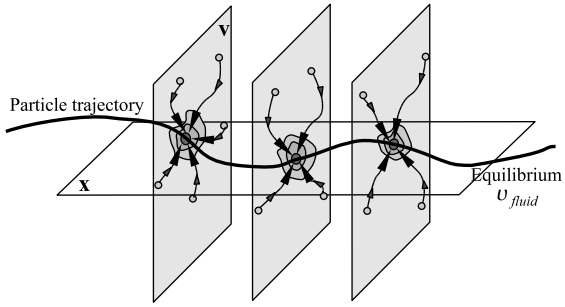

(a) *Slices parallel to the velocity dimensions of the particle phase space, in which changes in x are assumed negligible, showing the probability density function to concentrate on the equilibrium velocity. In the spatial dimensions of the particle phase space the particle probability density function convects at the flow velocity.*

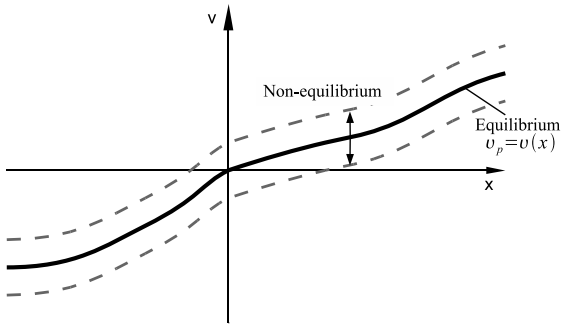

(b) *Schematic snapshot at a particular instant of the probability density function when the system is in equilibrium. A representation of the effect of non-equilibrium of the system is also shown.*

Figure 4.4: *Schematics showing the trajectory of the particle distribution at the equilibrium flow velocity as calculated using the slow equation.*

by the fast equation, Eq. 4.6 as described earlier. Also shown is the trajectory of the particle distribution through the phase space at the flow velocity as determined by the slow equation. A snapshot of the resultant distribution of the probability density function when the system is in equilibrium is shown in Figure 4.4 (b). The broadening of Φ about the fluid velocity due to non-equilibrium of the system is also represented. The transport due to non-equilibrium i.e. due to scatter of particle velocities about their equilibrium values, is represented by the second, 'residual' term in Eq. 4.15. This second term can be modelled in various ways. For instance, if a symmetric distribution of velocities about the equilibrium is assumed, then this term can be represented as an isotropic diffusion term $\nu_p \nabla_x^2 \rho_p$ (but where the diffusion coefficient is species dependent, i.e. $\nu_p = \nu_p(\Sigma)$). Alternatively, a more sophisticated non-isotropic model can be adopted to capture the skew of the particle velocity distribution about the equilibrium, for instance by including a dependence on vorticity gradients in the flow to model centrifugal spin-out of particles from vortex cores.

Thus the transport equation for the particulates within the species band Σ can be written

as

$$\frac{\partial}{\partial t}\rho_p + (\upsilon + \upsilon_g) \cdot \nabla_x \rho_p = S_p + \nu_p \nabla_x^2 \rho_p + \text{ other non-equilibrium terms} \tag{4.17}$$

where the source term $S_p(\Sigma)$ is introduced to allow the addition of particulates into the flow by entrainment from the ground. The assumption of the absence of collisions between particles allows any significant variations in the physical properties of the particulate matter within the flow to be accommodated by grouping the particulates into a number of species bands $\Sigma_1, ..., \Sigma_N$ and solving an independent transport equation for each band.

4.2.2 Equilibrium

For the particle transport equations to yield an adequate description of the movement of the particulates within the flow field while the helicopter is subject to brownout conditions, the principal underlying assumption of the analysis, namely that the airborne particulates exist in a state of near equilibrium with the aerodynamic and gravitational forces acting upon them, must be justified. This can be done as follows. Newton's equation, Eq. 4.1, can be redefined in terms of the relative velocity u between the fluid and the particle as

$$\dot{u} - F(u)/m = -\dot{\upsilon} \tag{4.18}$$

Consider the special case in the absence of gravity, so that particle force equilibrium is achieved when $u = 0$. If the force on the particle is given by Stokes' drag law

$$F(u) = 6\pi\rho\nu\frac{d}{2}u \tag{4.19}$$

then Eq. 4.18 can be rewritten as

$$\dot{u} - \frac{3\pi\rho\nu u d}{m} = -\dot{\upsilon} \tag{4.20}$$

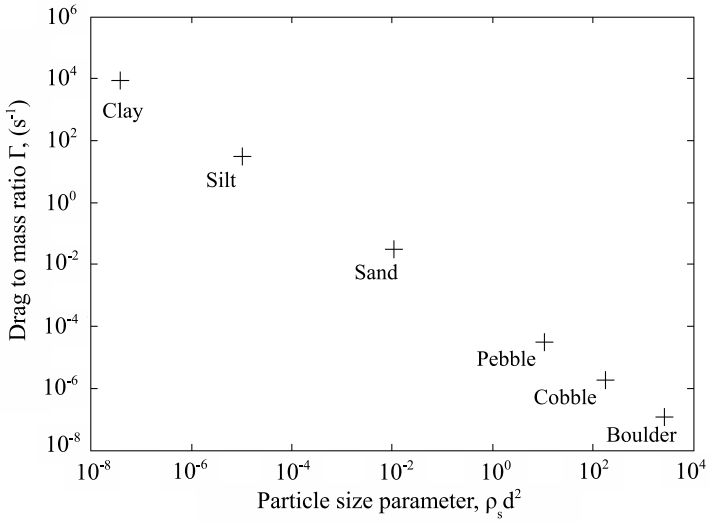

Figure 4.5: *Particle drag to mass ratios for various sizes of particles commonly encountered in the desert environment.*

When the particle velocity is close to the fluid velocity, the relative velocity u is small. Considering the limiting case where the velocity of the particle relative to the fluid remains constant i.e. $\dot{u} = 0$, then

$$u = \dot{v}/\Gamma \tag{4.21}$$

is a solution to Eq. 4.18, where the particle 'drag to mass ratio'

$$\Gamma = 18\frac{\rho}{\rho_s}\frac{\nu}{d^2} \tag{4.22}$$

The relative local deviation of the particle dynamics from equilibrium is thus small if u is small relative to v, in other words if $\Gamma \gg |\dot{v}|/|v|$, that is, if the drag to mass ratio of the particles is large compared to the local acceleration of the flow (scaled by the local velocity of the flow) in the Lagrangian, or particle, frame of reference.

Figure 4.5 shows typical values for the particle drag to mass ratio Γ (assuming the particle drag to be given by Stokes' law - note that this model underestimates the aerodynamic drag of large particles) as a function of the particle size parameter $\rho_s d^2$ for the variety of different particle types that might compose the ground surface below the helicopter when operating in

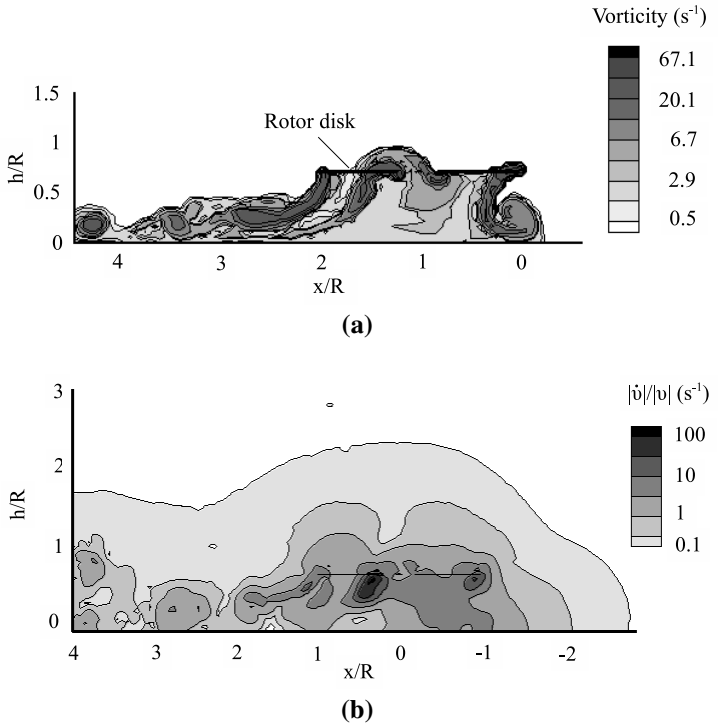

Figure 4.6: *Snap-shots of the instantaneous flow properties on a vertical slice through the centreline of an isolated rotor flying at* $0.68R$ *above the ground at an advance ratio of* 0.05 $(C_T = 0.0048)$. *(a) Contour plot of vorticity magnitude, showing the rotor to be in the ground vortex regime. (b) Plot showing the resultant distribution of the Lagrangian acceleration parameter* $|\dot{v}|/|v|$ *in the rotor wake (data scaled for a Blackhawk-sized aircraft).*

dusty conditions.

For comparison, Figure 4.6 shows a typical distribution of the Lagrangian acceleration parameter $|\dot{v}|/|v|$ within the flow in the wake below an isolated helicopter rotor operating in strong ground effect, as predicted using the VTM. In this example the rotor is flying 0.68 radii above the ground at an advance ratio of 0.05. The data is scaled to be representative of a helicopter in the same size class as a UH-60 Blackhawk. The Lagrangian acceleration parameter is calculated from the Eulerian velocity distribution in the flow surrounding the helicopter according to the equivalence $\dot{v} = \partial v/\partial t + v \cdot \nabla v$. It is important to bear in mind when analysing this figure that the finite resolution of the computation, results in any local maxima in the Lagrangian acceleration parameter being under-estimated. Any non-resolved finer structures in the flow will contribute significantly to the local acceleration through the

term $v \cdot \nabla v$.

Comparing Figures 4.5 and 4.6 shows that the question of the validity of the Eulerian transport equations derived earlier as a model for particulate transport in the helicopter flow field needs to be approached with some care. For given local flow conditions, the assumption of near-equilibrium becomes increasingly valid the smaller and lighter the particulate matter. The analysis of particulate transport using the Eulerian approach presented earlier, even when corrected for non-equilibrium effects by addition of suitable terms to the transport equation, would be somewhat questionable throughout the rotor flow field when the behaviour of large objects such as pebbles, rocks and other debris is important - such as might be encountered in the analysis of helicopter-induced damage and erosion for instance. In these cases, the traditional approach through calculation of the Lagrangian dynamics of individual particles within the flow is likely to remain the most reliable and efficient. Similarly the analysis for particles with intermediate size (e.g. sand) is likely to prove satisfactory only if augmented by terms, as described earlier, representing the non-equilibrium behaviour of the particles. Much anecdotal evidence suggests though that the principal composition of the brownout cloud is extremely fine, powder-like particulate matter. For this application, the comparison presented here suggests that, for realistic helicopter weights and sizes, the near-equilibrium assumption, and hence the analysis of the brownout problem using the particulate transport equations derived earlier, remains well-founded throughout most of the flow surrounding the helicopter - with perhaps the exception being near the cores of the individual vortices that constitute the rotor wake, and very close to the rotor itself.

4.2.3 Entrainment from Ground

In order to model the transport of particulates within the flow field surrounding a helicopter, the particulates must first be introduced to the flow. This is done by means of the source term S_p in the particle transport equation which accounts for the entrainment of particles from the ground into the airflow. In the context of brownout modelling, the model for the

source term provides essentially a 'sublayer'-type description that captures the essence of the complex physics that takes place within the few inches of fluid just above the ground. In much the same fashion as a boundary layer model matches the viscous, possibly turbulent characteristics of the flow near the surface to a simplified model that approximates the fluid behaviour away from the surface, the model for the particle source S_p is used to represent the effect of the physics in the sublayer on the dynamics of the particulate distribution in the flow away from the surface. In particular, within the sublayer, the particulate density can be high and the collisions between particles may assume fundamental importance - in direct variance with the assumption made earlier in deriving the particle transport equations.

According to Bagnold [54], entrainment of dust into the air takes place only if the velocity of the air just above the ground surface exceeds the minimum, or threshold, velocity required to initiate particle motion along the surface. The larger particles then roll and hop along the ground in a motion called 'saltation', and the impact of these saltating particles with the surface causes further particles to be ejected. Instead of returning to the surface, though, the smallest ejected particles become suspended within the flow field above the ground.

Within the helicopter context, the best approach to modelling the initial entrainment of dust from the ground plane into the air is still open to question. To date, published work investigating particle entrainment and the formation of dust clouds in the context of helicopter operations has been limited, thus, the models used to describe the entrainment process are taken from the field of aeolian sedimentology. These models are based around the idea of a threshold velocity on the ground plane. In the context of sedimentology, the flow velocities along the ground can be described as uniform whereas, in the helicopter context, the presence of tip vortices makes the flow along the ground distinctly nonuniform. However, recent investigations [3,5] that have examined the entrainment of particles into the wakes of model rotors have revealed very similar behaviour to that obtained using the numerical approach that has been adopted for the work presented in this dissertation, as shown in § 4.4.

In any case the physics of particle entrainment from the ground into the flow is very

complex. Direct modelling of the dynamics of saltating particles is well beyond the current state of the art, but there exists a number of empirical models for the saltation process that are able to take into account various factors such as surface roughness, soil moisture and soil crusting. Models of this complexity may be useful in capturing the detailed behaviour of the ground surface in specific geographical areas, but in the present work a simpler semi-empirical model [55],

$$v_t = \frac{1}{\kappa}\sqrt{a1\left(\frac{\rho_s}{\rho}gd + \frac{a_2}{\rho d}\right)} \tag{4.23}$$

that represents the threshold velocity for flow over dry, loose soil surfaces is used. On the basis of wind tunnel measurements by Lu and Shao [55], the coefficients a_1 and a_2 are approximately 0.0123 and 3×10^{-4} kgs^{-2} respectively. The factor κ accounts for the presence of surface roughness elements and their effect on the threshold velocity as described by Raupach *et al.* [56]. Many different roughness elements can be present in an actual desert environment but to simplify the model only one type is considered in the calculations presented in this dissertation. It is assumed simply that there are fragments of rock present that armour the surface and inhibit the entrainment of particulates into the flow. According to MacKinnon *et al.* [57], the value of κ for this type of surface is 0.44. d is the diameter of the saltating particles which Zender *et al.* [58] state are sand sized and therefore $d > 60\mu$m. For simplicity, the results presented in this dissertation were generated after adopting a single representative value of saltating particle diameter $d = 70\mu$m which, according to Yin *et al.* [59], has a density $\rho_s = 2650$kgm^{-3} for typical desert conditions where the particles are primarily composed of silica. Hence a uniform threshold velocity over the entire ground surface is assumed.

The overall source of particulate matter into the flow is dependent on the flux of saltating particles along the ground. The saltation or horizontal particle flux, Q, is determined using the theory of White [60] where the horizontal particle flux is related to the flow velocity v

just above the surface by

$$Q = Ecv^3 \frac{\rho}{g} \left(1 - \frac{v_t}{v}\right) \left(1 + \frac{v_t^2}{v^2}\right) \tag{4.24}$$

where v_t is the threshold velocity calculated from Eq. 4.23. Empirically, $c = 0.261$, and E is the ratio of erodible to total surface area, taken for simplicity to be unity in the calculations presented in this dissertation.

The particle flux from the surface into the airflow above the surface then consists of those dust particles that are released by the saltation process and remain in suspension in the air above the ground. The amount of dust that is released into suspension is dependent on the number of very small sized particles present within the erodible surface. Marticorena and Bergametti [61] suggest for instance that the ratio of the particle flux into the air to the saltation flux is dependent in the percentage of clay within the surface. In the current model, the empirical relationship

$$S_p = Qe^{13.4f-6.0} \tag{4.25}$$

described in Ref. [61] is used to relate the source S_p of particulate matter into the flow to the saltation flux. This relationship applies for erodible surfaces with clay fractions f less than 0.2; all results presented in this dissertation were generated using $f = 0.1$.

4.2.4 Fallout Model

The fallout velocity v_g in Eq. 4.17 accounts for the tendency of the suspended particulate matter to settle out from the flow under the influence of gravity. Referring again to Zender *et al.* [58], the size of particles which become entrained into, and suspended within, the flow are those which are clay-sized ($d < 2.5\mu$m) and silt-sized ($2.5 < d < 60\mu$m). Reference [2] presents data, obtained during flight tests, on the composition of the dust clouds produced by helicopters in desert conditions. During the flight tests a number of different helicopters were flown over a dusty surface and the dust that became entrained into the air was collected at

various stationary points on the ground. The particle sizes reported by Zender *et al.* compare well to the size of the particles collected during the flight tests, where the greatest number of particles, in terms of the number of particles in suspension within the dust clouds, were those with a diameter less than 50μm.

The model that was used to calculate the fallout velocity for the calculations presented in this dissertation is based on the work by Cheng [62] which extends Stokes' solution for the settling velocity of spherical particles to the case where the particle Reynolds number is greater than one. The dimensionless particle diameter, $d_\star$, is first defined as

$$d_\star = d\left(\frac{gb}{\nu^2}\right)^{(1/3)} \tag{4.26}$$

where $b = (\rho_s - \rho)/\rho$ and d is the diameter of the particles for which the fallout velocity is to be calculated. The fallout velocity of the particles is then given by

$$v_g = \frac{\nu}{d}\left(\sqrt{25 + 1.2d_\star^2} - 5\right)^{1.5} \tag{4.27}$$

For all the results presented in this dissertation, the particle diameter used when calculating the fallout velocity is 2μm. This particle size is representative of some of the smallest particles that become suspended within the flow field. By selecting this value for the diameter of the particles, the density of the dust cloud that is predicted by the VTM will be greater than if the particles were assumed to be larger, as smaller particles tend to remain suspended within the flow for greater lengths of time than larger particles. The difference in the dust clouds produced by the helicopter rotor when the particles that become suspended in the flow field are modelled as different sized particles is shown in Figure 4.7. The dust density distribution in the flow field around a rotor hovering in ground effect, as calculated for two different diameters of the suspended particles, is shown. Figure 4.7 (a) shows the contours of the dust density distribution, averaged over approximately 30 rotor revolutions, that are produced when the particle diameter used for calculating the fallout velocity is set to

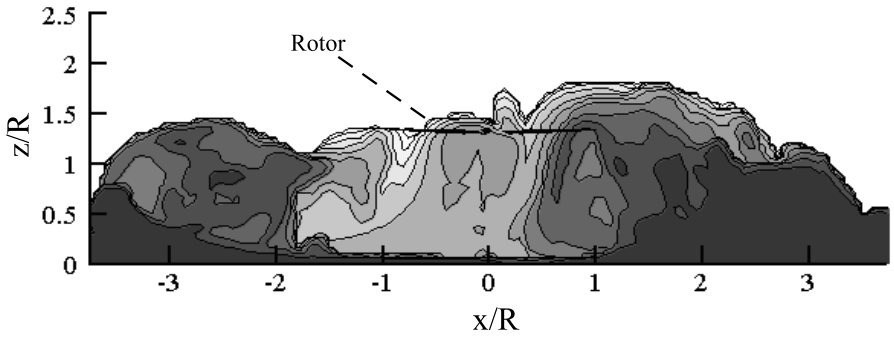

(a) *Particle diameter* $d = 2\mu m$

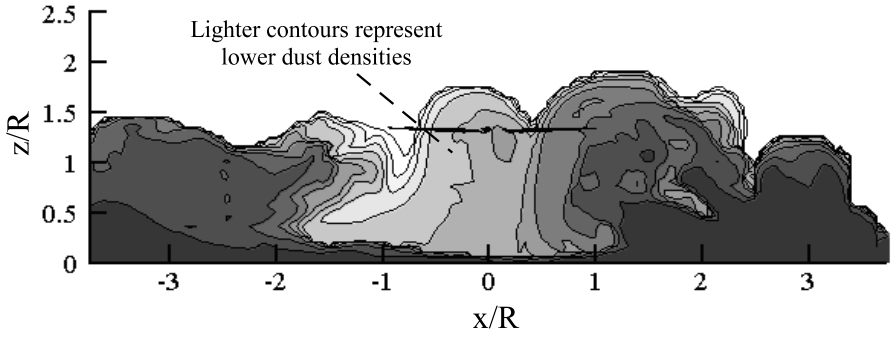

(b) *Particle diameter* $d = 20\mu m$

Figure 4.7: *Comparison of the dust density distributions which result from calculating the particle fallout velocity using two different particle diameters. Rotor from a CH-53E modelled in hover at a height of 1.274R above the ground.*

$d = 2\mu$m (the same as the diameter used for all the simulations presented elsewhere within this dissertation), while, for Figure 4.7 (b), $d = 20\mu$m. The darker contours represent higher dust densities and thus it is shown that the higher dust densities, in the region around the rotor, are produced when the smaller particle size is modelled. Although there is a difference in the density of the dust clouds that are generated, qualitatively the results are very similar. This difference in the detail of the dust distribution is of interest if simulating the distribution around an actual helicopter system. The composition of the dust on the ground plane below the helicopter and the size of the particles that become suspended within the flow must of course be known if an accurate prediction of the density of dust within the cloud produced by a specific helicopter under specific conditions is required. The particle entrainment and

fallout models used within the VTM can be tuned to specific site conditions but this is contrary to the intention of the research presented in this dissertation. The research presented in this dissertation focuses on the more fundamental questions of particle entrainment in an attempt to understand the underlying physics that governs the formation of dust clouds around helicopters rather than attempting to replicate specifics of the brownout phenomenon that is generated by any particular rotor system at any particular geographic location and hence representative properties of the particles are used.

4.3 Computational Implementation

When implementing the particle transport model, it is important that any extra computational expense required to run the VTM together with the particle transport model is kept to a minimum. On comparing the mathematical form of the vorticity transport equation, Eq. 2.8, and the particle transport equation, Eq. 4.17, it can be seen that there are obvious algebraic similarities between them. Both equations (when taken at face value) represent the passive advection of some quantity by a background velocity field, and allow for a localised source of the advected quantity. In the case of the vorticity transport equation an additional stretching term appears simply to account for the fact that the advected quantity (the vorticity) is fundamentally vectorial in nature rather than scalar as in the case of the particulate density. The similarity in structure between the two transport equations allows the procedure that is used within the VTM to calculate the evolution of the vorticity within the flow simply to be generalised slightly if the combined evolution of the flow and particulate density is to be calculated. For the combined particulate-vorticity transport model, define the vector of conserved variables $\Omega(x,t) = (\omega, \rho_p^1, ..., \rho_p^N)$ where $\rho_p^i(x,t)$ is the local density of particles in species band Σ_i at time t. The object-oriented structure of the VTM allows the augmented vector Ω of conserved variables simply to be defined as a generalised form of the vector of conserved quantities ω that is used by the original, fluid-only version of the code. The

VTM uses an operator-splitting approach, as described in § 2.3.2.1, to evolve the equations of motion for the coupled system. The source of Ω into the computational domain is first calculated by evolving the equation

$$\frac{\partial}{\partial t}\Omega = S \tag{4.28}$$

over time Δt, using the initial condition $\Omega(x,t)$ to yield the intermediate solution $\Omega^*(x)$. The combined particulate/vorticity source $S = (S_\omega, S_p^1, ..., S_p^N)$ is constructed using the appropriate physical model for each component. The advection equation

$$\frac{\partial}{\partial t}\Omega + V \cdot \nabla\Omega = 0 \tag{4.29}$$

is then advanced through Δt, using Ω^* as initial condition, to yield the revised intermediate solution Ω^{**}. The advection velocity $V = (\upsilon, \upsilon + \upsilon_g)$, and the operator $a \cdot \nabla b$ is over-loaded so that $(a,b) \cdot \nabla(c,d) \equiv (a \cdot \nabla c, b \cdot \nabla d)$. This part of the calculation is performed using Toro's Weighted Average Flux method, as described earlier, which allows tight control to be maintained over any spurious diffusion of vorticity or particulate density from cell to cell as a result of numerical truncation errors.

Finally the vorticity distribution is corrected for the effect of stretching by advancing the solution to

$$\frac{\partial}{\partial t}\omega - \omega \cdot \nabla\upsilon = 0 \tag{4.30}$$

through Δt using Runge-Kutta integration, and initial conditions ω^{**}, to obtain the solution ω^{***}. The vector $(\omega^{***}, \rho_s^{1**}, \rho_s^{N**})$ is then a second order accurate approximation to $\Omega(x, t + \Delta t)$ as long as Ω^* and Ω^{**} are both second order accurate approximations to the solutions of their own differential equations. The process is then repeated for subsequent timesteps. The similarity of this approach to that used by the fluid-only version of the VTM can be assessed by comparing this sequence of operations to that described in § 2.3.2.1.

In the calculations presented in this dissertation, no non-equilibrium processes were ac-

counted for but these could be included in the calculation through an additional computational step that has similar form to that used to evolve the solution to Eq. 4.28.

4.4 Verification of the Particle Transport Model

Before the particle transport model can be used with any degree of confidence, the dust density distribution as predicted by the VTM must first be compared to available experimental data to show that the results from the VTM are realistic and accurate. To date, limited experimental data has been published against which the ability of the VTM to predict the dust distribution around a helicopter is desert conditions can be compared. There is, however, data available in the open literature from a flight test conducted in the 1960s in which a Piasecki H-21 was hovered above a dusty surface [1]. During the flight test, dust that was entrained and transported within the flow field was collected at a number of sampling stations mounted at various positions on the aircraft. This flight test was replicated using the VTM to investigate whether the dust distribution as calculated by the VTM resembled that generated during the flight test. The comparison is hindered to a significant extent because the flight test data was somewhat limited and specification of the composition of the surface, to the level required for accurate characterisation of the entrainment of dust, was not available. The tandem rotor configuration of the aircraft was simulated, but the fuselage of the helicopter was not represented. Figure 4.8 shows a comparison between the dust concentrations measured during the flight test and those calculated using the VTM. The mass of dust collected at sampler stations positioned along the length of the starboard side of the fuselage during the flight test was used to determine the concentration of dust within the flow field which is shown in the figure. The density of dust as predicted by the VTM at the same positions as the sampler stations is also shown.

To investigate the effect of the diameter of the suspended particles, and thus fallout velocity, on the dust distributions that were calculated, two separate simulations, one with a

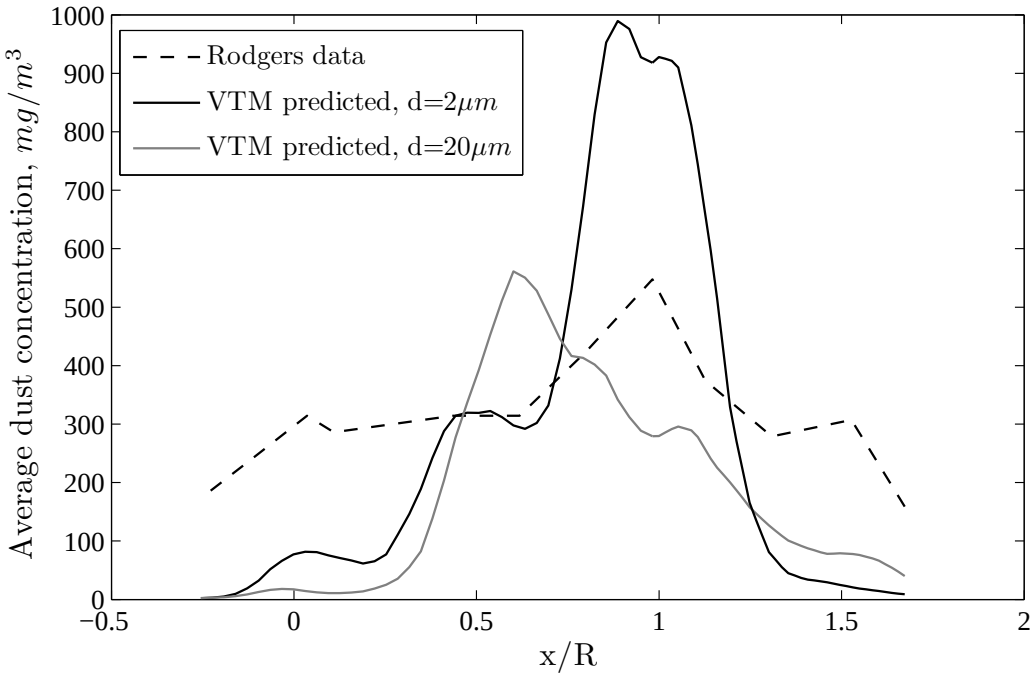

Figure 4.8: *Dust concentration along the length of the fuselage of a Piasecki H-21 collected during the flight tests described by Rodgers [1], compared to that calculated using the VTM.*

suspended particle diameter of 2μm and another with 20μm were conducted. The distribution of dust along the length of the fuselage as calculated using the VTM is similar to that determined from the flight test with the maximum concentration, for the particle diameter of 2μm, occurring at much the same position. The difference between the maximum and minimum dust concentrations is, however, somewhat larger than the difference in the data from the flight test. When the size of the particles that were simulated is increased there is a significant decrease in the maximum dust concentration that is calculated. The behaviour of the dust once in the flow is thus shown to depend strongly on the particle diameter as the larger the size of the suspended particles the greater the fallout velocity. Thus larger particles will settle out of the flow more quickly than smaller particles. The amount of dust that is initially entrained into the flow field is also very sensitive to particle size and to the model that is used to represent the entrainment of dust from the ground plane. As the flight test was not conducted in a controlled environment, it is likely that a wide range of particle sizes were

present in the soil. To compute the dust concentrations accurately, the particles sizes used when calculating the threshold velocity of the particles that are on the ground plane and when calculating the fallout velocity of the particles that are suspended within the flow, would have to be adjusted until the required spectrum of dust concentration is achieved. Thus, to obtain a true understanding of the ability of different computational models to predict the distribution of dust within the flow field around a rotor, a controlled experiment must be conducted in which the particles are all of a known diameter. The properties of the particles used in such an experiment could then be specified directly in the computational models. Comparison of the predictions of the density of dust within the flow field around the rotor with results from the experiment would thus allow the ability of the computational models to predict accurately the phenomenon of brownout to be established. Experiments to this level of rigour have however still to be attempted.

When investigating the formation of the dust cloud in the flow field around a rotor, if the focus is on understanding the general physics that govern the particle entrainment and transport processes then matching the global characteristics of the cloud is of greater interest than predicting accurately the spectrum of dust density. A recent experimental study was carried out at the University of Glasgow [3] in which the global characteristics of the dust cloud generated by a rotor were examined. This experiment has provided data against which the dust distributions, as predicted by the VTM, can be compared. This comparison has allowed greater confidence in the predictions of the VTM to be gained. The experiment involved placing fine particles on the floor of a wind tunnel below a small model rotor to simulate the dynamics of the dust particles that would be entrained into the flow around a rotor in a brownout situation. Although the exact sizes of the particles were not known, this wind tunnel experiment focused on a very small region of the flow field and provided insight into the behaviour of the dust along the ground plane and transport of this dust once entrained into the flow. The motion of the particles as they were transported through the flow surrounding the rotor was recorded using high-speed photography. Figures 4.9 (a) and (b) show typical

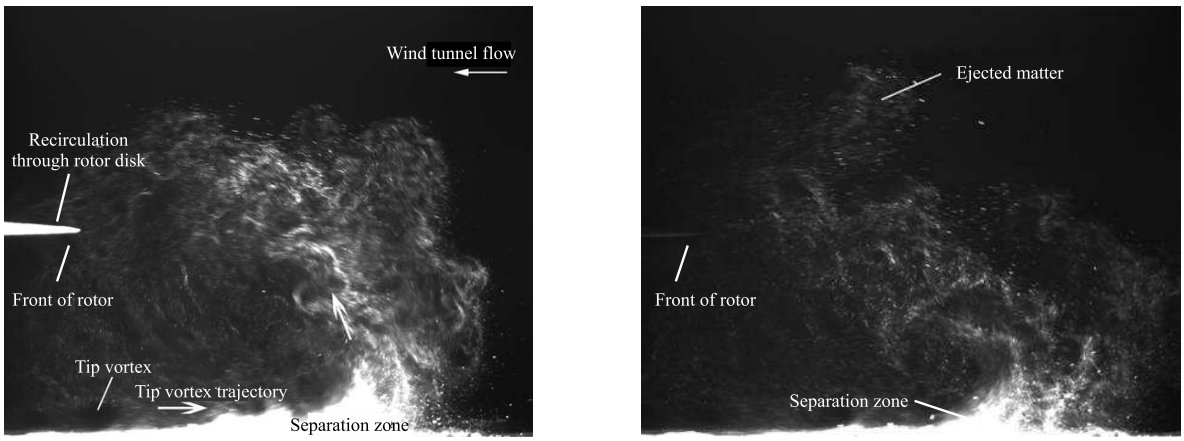

(a) **(b)**

Figure 4.9: *Snapshots showing the particulate distribution around a rotor during wind tunnel simulations of brownout [3]. Blade tip visible at middle left. (a) Image showing the recirculation of fine particulates through the front of the disc and the existence of a well-defined 'separation zone' above the ground plane. (b) Image showing the escape of a cloud of particles from the main recirculatory flow.*

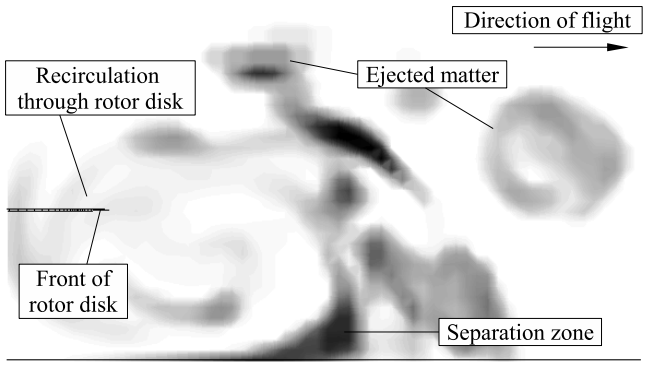

Figure 4.10: *VTM-predicted particulate density distribution on a vertical slice through the rotor centreline under the same flight conditions as Fig. 4.9, showing qualitatively the same features as the experiment.*

snapshots of the particle distribution in front of the model rotor when it was placed at one radius above the ground and the tunnel speed was set to represent a thrust-normalised advance ratio of 0.65. For comparison, Figure 4.10 shows a representative snapshot of the particle density distribution in front of the rotor that is predicted by the VTM under similar flight conditions. The experiment reveals a wedge-shaped area in the flow some distance upstream of the rotor, termed the 'separation zone' by Nathan and Green [3], in which the particle density is very high as a result of the existence of a flow stagnation line in the mean flow on the surface below. The process governing the build-up of dust in this area is described as 'sediment trapping' by Johnson, Leishman and Sydney [5]. Figure 4.10 shows the location and size of this zone to be represented well by the VTM. Figure 4.9 (a) shows a significant proportion of the suspended particulate matter to be recirculated through the front of the rotor disc under the operating conditions of the experiment, but Figure 4.9 (b), captured at a later time during the same experiment, shows that clouds of particles that do not recirculate through the rotor are also ejected sporadically from the separation zone. Figure 4.10 shows both these characteristic features of the dynamics of the dust cloud surrounding the rotor to be captured by the VTM.

The ability of the VTM to predict the behaviour of the particles of dust when a rotor wake interacts with a ground plane is illustrated further by Figures 4.11 and 4.12. Figure 4.11 shows numerically generated vorticity and dust density distributions produced using a higher resolution grid than was used for Figure 4.10 while Figure 4.12 shows a snapshot of the dust distribution from the experiment described above. This comparison between numerical and experimental dust distributions reveals that, qualitatively at least, the VTM reproduces the key features within the flow. The rotor tip vortices are shown, in both the numerical and experimental images, to travel along the ground plane with a small wedge shaped zone of dust forming in front of each individual vortex as a result of the local increase in velocity and subsequent turning of the flow away from the ground plane. This comparison suggests that, although there may be some controversy over how applicable models from the field

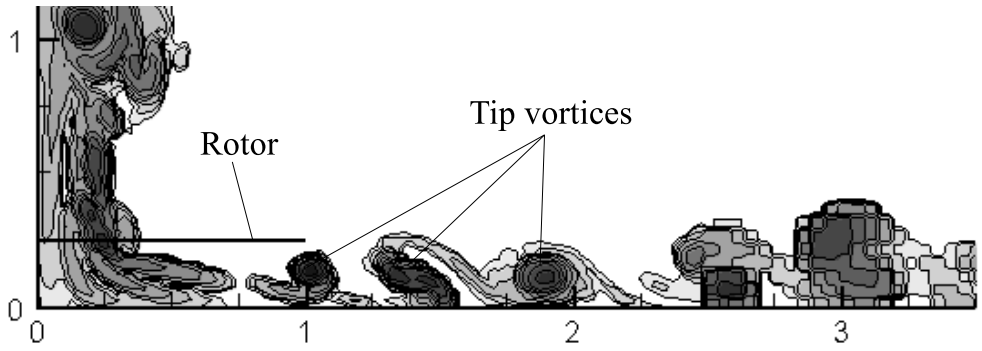

(a) *Contours of vorticity distribution*

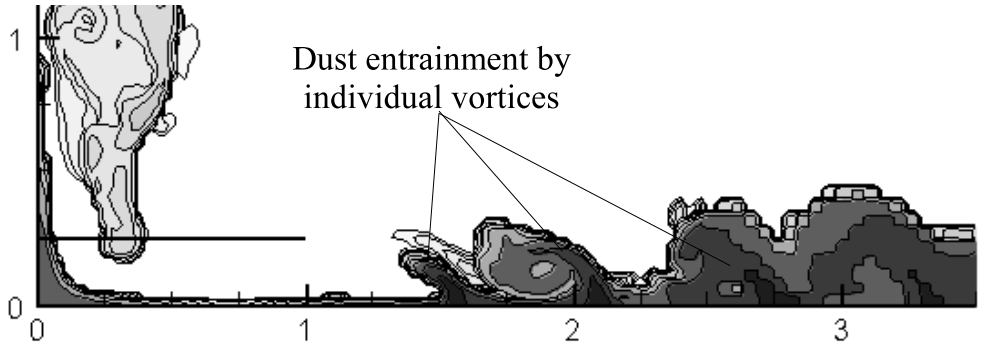

(b) *Contours of dust density distribution*

Figure 4.11: *Vorticity and corresponding dust density distributions in the flow field below a rotor in ground effect as predicted using the VTM.*

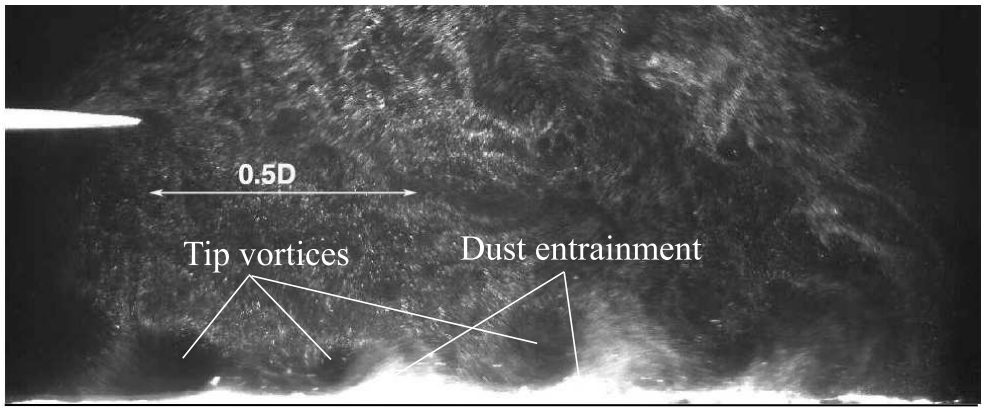

Figure 4.12: *Snapshot showing the effect of the tip vortices on the particle distribution along the ground plane. Image from wind tunnel experiment conducted by Nathan and Green [3].*

of sedimentology are in the helicopter context, the empirical models used to describe the entrainment of particles from the ground plane, as outlined in § 4.2.3, may well be capable of representing the physics of particle entrainment and transport in the context of helicopter brownout.

Although a more quantitative verification of the numerical approach awaits further refinement of the experimental technique, the good qualitative agreement between the particulate density distribution that are predicted by the VTM and the distribution of particulates that were observed in this simple experiment suggests that the VTM is capable of producing credible simulations of the evolution of the dust cloud surrounding the helicopter under brownout conditions.

4.5 Summary

Modification of the VTM has allowed the calculation of particle entrainment and transport for the simulation of helicopter operations in brownout conditions. The assumptions made when employing an Eulerian based approach to model the particle transport have been shown to be justified for the smallest particle sizes. The majority of the particles found in the dust clouds produced by helicopters are of these smaller sizes. The initial entrainment of particles from the ground plane into the flow field surrounding the helicopter involves very complex physics. This process is modelled using semi-empirical methods taken from the field of sedimentology. A threshold velocity must be reached before the saltation of larger particles across the ground is initiated. The saltation of larger particles releases smaller particles from the ground which then become suspended within the flow. Once in the flow field, these small particles are transported with the flow. An additional fallout velocity is introduced when calculating the trajectory of the particles to account for the effects of gravitational settling. Initial qualitative comparisons with experimental simulations and basic quantitative comparisons with flight test data provide confidence in the predictions of the VTM.

Chapter 5

Variation of Wake Structure with Rotor Configuration

5.1 Introduction

When helicopters are operated in close proximity to the ground, the presence of the ground plane can influence the geometry of the wake that is generated by the rotor. Out of ground effect, the wake is transported downstream and away from the rotor. In ground effect, however, when at low enough forward speeds, the ground plane impedes the transport of the wake below the rotor. The changes in wake structure that occur, as described by Curtiss *et al.* [20] and discussed in § 3.3.1, can often result in the rotor operating within its own wake. When examining the wake geometries that are generated by different rotors in ground effect, although each wake is composed of vorticity that is shed and trailed from the blades, the overall structure of the wake that forms appears, from the calculations performed during the course of this study, to be rotor dependent. Presented in this chapter are results from an investigation into how the configuration of the rotor influences the geometry of the wake that is produced and how the changes in wake geometry, in turn, effect the development of the dust cloud that results. Presented first is a comparison of the geometry of the wakes produced

by a number of isolated rotors hovering at various heights above the ground. These rotor systems differ in terms of their number of blades, the twist of the blades of the rotors and the thrust coefficient to which the rotor is trimmed. Also presented is a comparison between the wake generated by a single rotor helicopter and that generated by a tandem rotor helicopter. Data regarding the number of helicopter accidents encountered by the US Army as a direct result of brownout [63,64] suggests that helicopters with rotors in a tandem configuration are more susceptible to brownout than single rotor helicopters. The comparison between the two configurations is done to determine whether this difference between single rotor helicopters and tandem rotor helicopters is due to the behaviour of the rotor wake rather than the operational procedures of the helicopters. For the comparison both systems are trimmed to the same overall thrust coefficient. The connection between the rotor wake and the dust cloud that is generated is then established. Finally, the dust clouds generated by the generic single rotor and tandem rotor configurations are compared to determine whether the tandem configuration is indeed more prone to inducing the brownout condition.

5.2 Effect of Grid Resolution

The formation and development of the dust cloud around a helicopter is strongly linked to the dynamics of the flow field surrounding the helicopter as is discussed in § 5.5.3. To determine to what extent the grid resolution of the calculations conducted using the VTM affects the detail captured in both the rotor wake and dust distribution, a comparison is made between two simulations run with different grid resolutions – one for a rotor in forward flight and one for a rotor in hover. Figures 5.1 and 5.2 show instantaneous snapshots of the vorticity and dust density distributions in the flow field around a rotor in forward flight calculated when the resolution of the grid is set to 20 and then to 40 cells per rotor radius. The figure shows the distributions on a plane that intersects the longitudinal centreline of the rotor. The rotor that was modelled was that used in the experiment of Lee *et al.* [4] as described in § 3.2.2. The

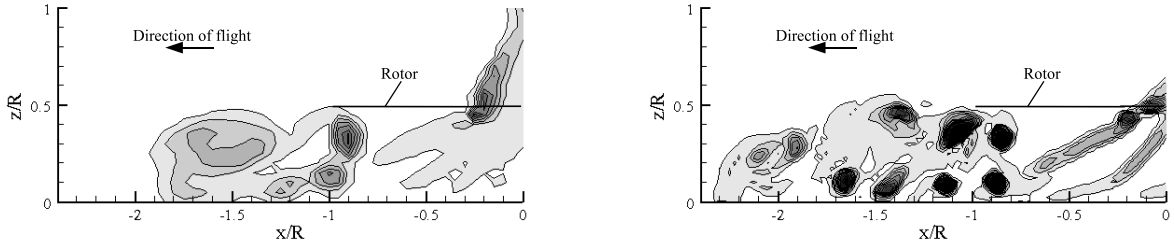

(a) *Resolution of 20 cells per blade radius.* **(b)** *Resolution of 40 cells per blade radius.*

Figure 5.1: *Comparison of snapshots of the instantaneous vorticity distribution in the wake of Lee's [4] rotor during forward flight calculated using different grid resolutions.*

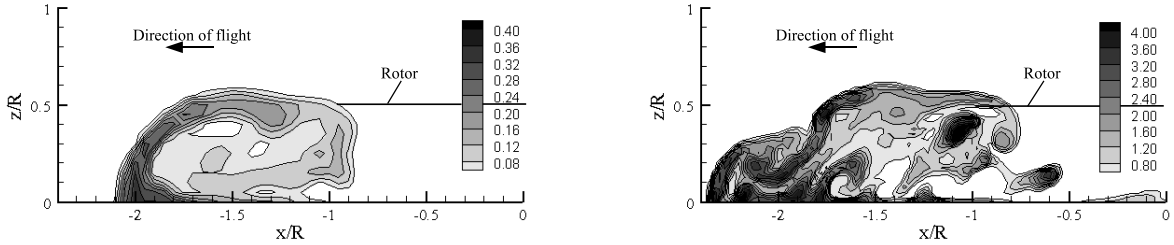

(a) *Resolution of 20 cells per blade radius.* **(b)** *Resolution of 40 cells per blade radius.*

Figure 5.2: *Comparison of snapshots of the instantaneous dust density distribution in the flow field around Lee's rotor during forward flight calculated using different grid resolutions.*

rotor was simulated at a height above the ground of $0.5R$ and at a forward speed $\mu^\star = 0.4$.

Examination of the snapshots of the vorticity distribution calculated at each grid resolution, shown in Figure 5.1, reveals that, in both cases, the wake travels down below the leading edge of the rotor and extends out along the ground plane in front of the rotor to approximately $x/R = -2$. As expected however, at the higher grid resolution there is greater resolution of the individual tip vortices than when the vorticity distribution is calculated at the lower grid resolution. Figure 5.2 shows this to result in a difference in the dust density distribution that is calculated by the VTM using the two different grid resolutions. At both resolutions there is large build-up of dust which forms at approximately $x/R = -2$ where the radial velocity of the tip vortices is no longer great enough to penetrate any further into the oncoming flow. Once in the flow field, the dust in transported back inwards towards the rotor disc. At the higher resolution, the small scale structures of dust that form around the in-

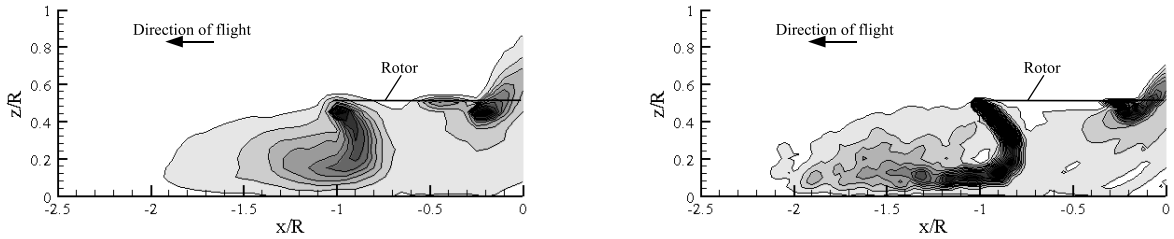

(a) *Resolution of 20 cells per blade radius.* **(b)** *Resolution of 40 cells per blade radius.*

Figure 5.3: *Comparison of the average vorticity distribution in the wake of Lee's rotor during forward flight calculated using different grid resolutions.*

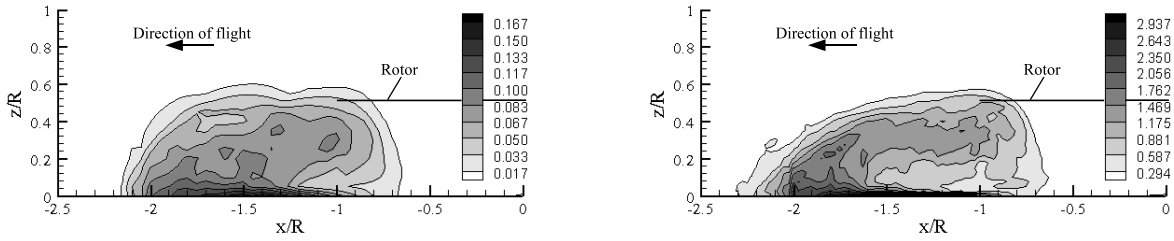

(a) *Resolution of 20 cells per blade radius.* **(b)** *Resolution of 40 cells per blade radius.*

Figure 5.4: *Comparison of the average dust density distribution in the flow field around Lee's rotor during forward flight calculated using different grid resolutions.*

dividual tip vortices are resolved, whereas at the lower resolution these small scale structures are not shown.

Although the instantaneous snapshots of the flow field that were calculated using the two different grid resolutions appear quite different, by averaging the distributions over a number of revolutions it is revealed that the overall behaviour of the wake is very similar, as shown in Figures 5.3 and 5.4. The vorticity distribution that is calculated at each resolution shows the wake to travel down from the leading edge of the rotor and to form a vortical structure that extends out to approximately -2R along the ground plane below the front of the rotor. The strength of the averaged vorticity which extends down from the rotor is however slightly greater at the higher resolution. Close examination of the averaged dust distributions, shown in Figure 5.4, reveals that, although the size and geometry of the dust clouds calculated at the two different resolutions appear very similar, there is in fact a significant difference

between the density of dust contained within the clouds. At the higher resolution, the density of dust is much greater than at the lower resolution. This difference is a result of the non-linear relationship between the induced velocity along the ground plane and the amount of dust that becomes entrained into the flow, as shown by Eq. 4.24. Thus, as the individual tip vortices are better resolved at the higher grid resolution, and as each individual vortex induces a velocity field around itself, as these vortices travel along the ground plane they entrain more dust than is predicted at the lower resolution. As the work in this dissertation focuses on understanding the general characteristics of the formation of the dust cloud, and not on predicting accurately the spectrum of dust around any particular rotor, the fact that each individual vortex entrains a small region of dust is of more interest than the increase in the density of the dust cloud that forms as a result.

The vorticity and dust density distributions as predicted by the VTM to be generated by the rotor of an OH-6A when in hover are shown in Figures 5.5 and 5.6. These figures show iso-surfaces of the vorticity and dust distributions around the rotor when hovering at a height of $1.5R$ above the ground. As with the forward flight simulations, a comparison of the distributions that are calculated when the resolution of the grid is set to 20 and to 40 cells per rotor radius is shown in each figure. These instantaneous snapshots of the distributions are extracted once the rotor wake has settled into its long-term behaviour. To reveal the internal details of the flow field, the distributions have been sectioned through the longitudinal centreline of the rotor.

Examination of the vorticity distributions generated by the VTM at the different grid resolutions, shown in Figure 5.5, reveals that, at both resolutions, the wake tube is predicted to stream down from the rotor disc before turning and travelling radially outwards as it approaches the ground plane. The figures do, however, show there to be a significant difference in the detailed structure of the rotor wake that is predicted by the VTM when run at the different grid resolutions. At the higher resolution (Figure 5.5 (b)), the individual tip vortices that are trailed from the rotor blades are resolved. As these vortices travel across the ground,

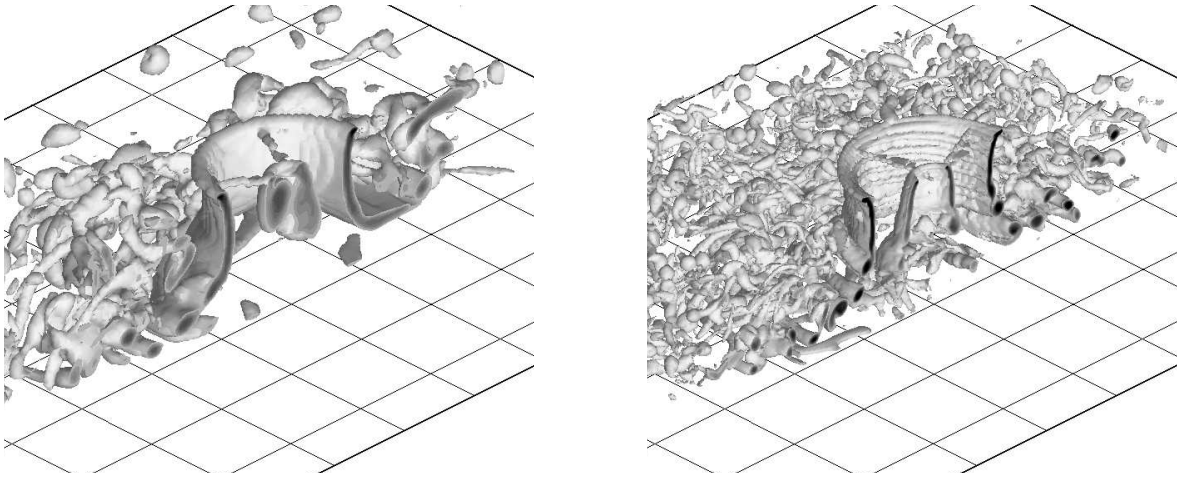

(a) *Resolution of 20 cells per blade radius.* **(b)** *Resolution of 40 cells per blade radius.*

Figure 5.5: *Comparison of the vorticity distribution in the wake of an OH-6A rotor in hover calculated using different grid resolutions.*

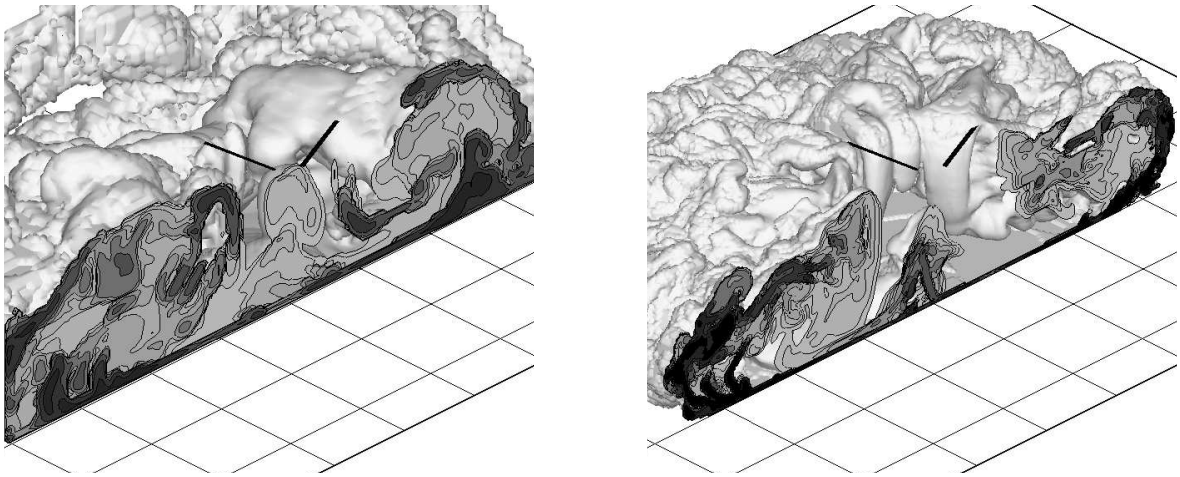

(a) *Resolution of 20 cells per blade radius.* **(b)** *Resolution of 40 cells per blade radius.*

Figure 5.6: *Comparison of the dust density distribution in the flow field around an OH-6A rotor in hover calculated using different grid resolutions.*

instability in the wake causes them to break down into a large number of small scale structures. At the lower resolution (Figure 5.5 (a)) the finer scale features of the individual tip vortices are not resolved as the wake streams down from the rotor. It is also apparent that, as the wake extends along the ground plane, the breakdown of the vortical structures formed by the tip vortices does not result in such a large number of small scale structures.

The effect that the change in grid resolution has on the dust distribution that is generated by the rotor is shown in Figure 5.6. As with the vorticity, the main features of the distributions are the same in that there is a build-up of dust below the centre of the rotor and a large cloud that forms close to the tips of the rotor blades. At the furthest reaches of the dust cloud a separation zone (described in more detail in § 5.5.3), where the dust density is highest, forms. This build-up of dust occurs where the radial velocity of the tip vortices is no longer great enough to allow them to extend any further out into the flow field. The dust from the separation zone is then transported within the flow field by the induced velocities within the wake and travels back inwards towards the rotor.

As with the flow field generated during forward flight, the instantaneous snapshots of the flow field generated in hover, that were calculated by the VTM when the resolution of the grid was set to 20 and separately to 40 cells per rotor radius, in particular the vorticity distribution, appear quite different. By averaging the distributions over a number of revolutions however, it is revealed that the overall behaviour of the wake is very similar, as shown in Figures 5.7 and 5.8. The calculation conducted at each resolution shows the vorticity within the flow field to travel down towards the ground plane then radially away from the rotor. It can also be seen that the extent of the wake along the ground plane is very similar at both resolutions with the iso-surface of vorticity shown here extending to approximately $2.5R$ from the centre of the rotor. There is still, however, some difference in the number of smaller scale vortical structures that are resolved at each resolution. The averaged dust distributions shown in Figure 5.8 are perhaps somewhat misleading in that there appears to be more dust present within the flow field in the simulation at the lower resolution compared to the forward flight

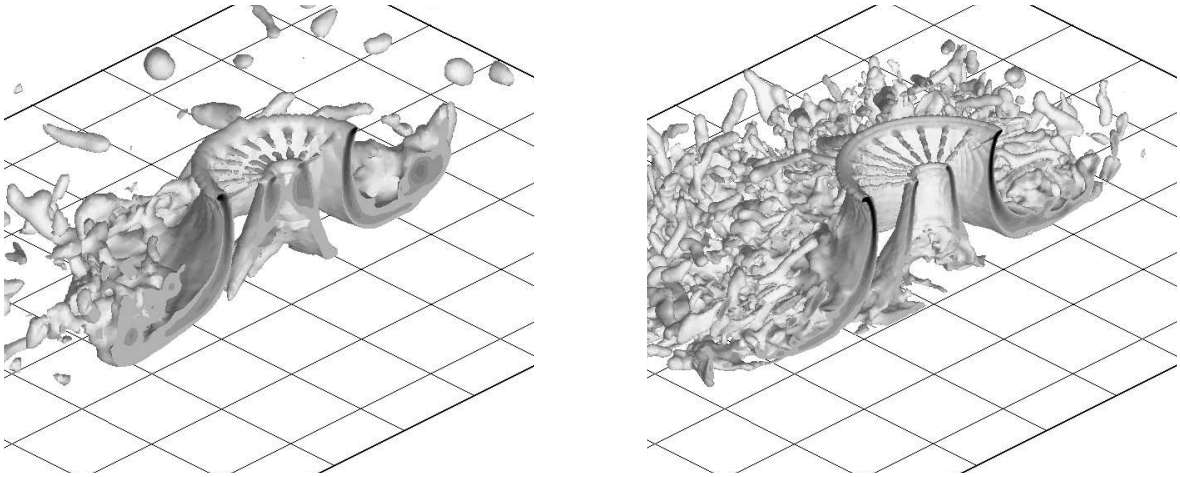

(a) *Resolution of 20 cells per blade radius.* **(b)** *Resolution of 40 cells per blade radius.*

Figure 5.7: *Comparison of the average vorticity distribution in the wake of an OH-6A rotor in hover calculated using different grid resolutions.*

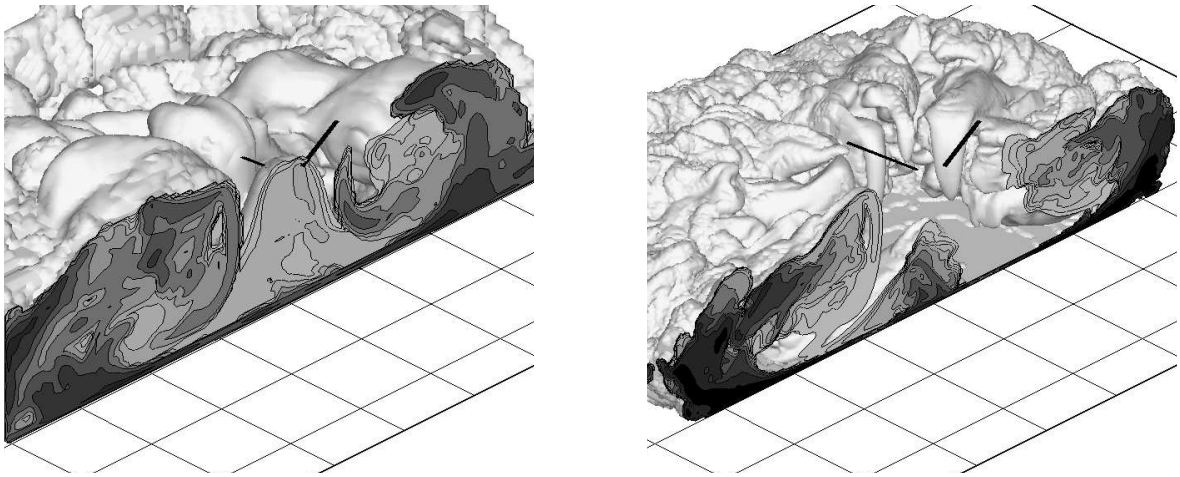

(a) *Resolution of 20 cells per blade radius.* **(b)** *Resolution of 40 cells per blade radius.*

Figure 5.8: *Comparison of the average dust density distribution in the flow field around an OH-6A rotor in hover calculated using different grid resolutions.*

simulation where more dust was generated at the higher resolution. In forward flight the increase in dust was a result of the individual tip vortices being resolved. In hover, however, the increase in dust is the result of the infinite supply of dust on the ground plane. The calculation at lower resolution takes a greater number of rotor revolutions for the wake to settle into its long term behaviour. Thus, to ensure that the long term behaviour of the wake is captured, the average must be taken using the dust distribution generated at rotor revolutions which occur later in the simulation. As there is no limit to the amount of dust that can be sourced from the ground in the current model, in hover the dust continues to accumulate within the flow field as the simulation progresses. Thus, at later revolutions there is more dust within the flow field surrounding the rotor. A comparison of the dust distributions at the two grid resolutions does however show that the behaviour of the dust in both cases is comparable. The separation zone forms at a similar location and, once in the flow field, the dust is transported in towards the rotor and circulates through the rotor disc.

Examining the effect of the grid resolution on the vorticity and dust distributions that are calculated in forward flight and in hover has revealed that, although at the lower resolution the wake may take longer, in terms of rotor revolutions, to reach its long term behaviour, the main, large scale features of the distributions are similar to the features revealed by the calculation run at the higher resolution. When conducting simulations, if the focus is primarily on examining the overall formation of the wake and dust distribution, for example those generated by a single rotor and a tandem rotor helicopter, and resolving only the gross features of the flow is sufficient, then a lower grid resolution may be used. If, however, there is interest in simulating the individual tip vortices and in generating the wake in more detail, then a higher grid resolution is obviously required. There is, however, a trade off between grid resolution and computational time. For this reason, the majority of the results presented in this dissertation were calculated using a grid resolution of 40 cells per rotor radius but, given the extra computational time required to calculate fuselage interactions, the simulations which include a fuselage were calculated using 20 cells per rotor radius. Care

must however be taken when comparing the dust distributions generated by different rotors at different grid resolutions. It has been shown that the main structures of the distributions are the same at different grid resolutions but the details differ. In light of the aims of the research in this dissertation, where the focus is on understanding the physics that governs the entrainment of dust, as long as the main structures within the distribution are predicted then the differences in the detail are not as important. It should also be noted that, as discussed in § 4.4, the amount of dust suspended within the flow field depends very much on the particle characteristics and the entrainment models used and hence will also affect the details of the dust distributions. Care must also be taken when examining the dust distributions generated by different hovering rotors. It must be ensured that the rotor revolutions over which the data is examined is consistent for each rotor simulation.

5.3 Averaging the Flow Fields

In ground effect, the wakes generated by rotors can be highly unsteady – particularly when the rotor is operating at very low forward speeds. This unsteadiness can result in one snapshot of the vorticity field at a particular instant looking very different to another snapshot taken a short time later. Throughout the remainder of this dissertation the vorticity and dust distributions generated by different rotors are compared. This poses a problem in how best to present such unsteady flow fields. To overcome this problem the average of a series of instantaneous snapshots of the wake is often plotted instead of plotting the individual snapshots themselves. The number of snapshots used to generate the average is large enough to reveal the persistent features of the flow whilst the more unsteady structures weaken. In all cases, where an averaged plot is shown, the snapshots used to generate the average were taken far enough into the simulation to allow the initial transients of the system to have dissipated.

Figure 5.9 shows an example of an averaged flow field in comparison to an instantaneous snapshot. Three-dimensional images of the vorticity and dust density distributions found

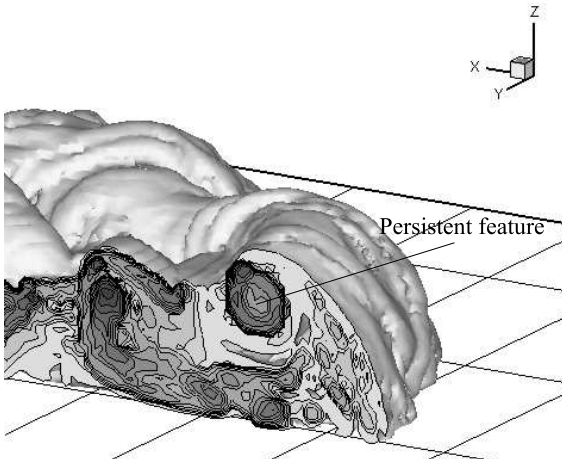

(a) *Instantaneous vorticity distribution*

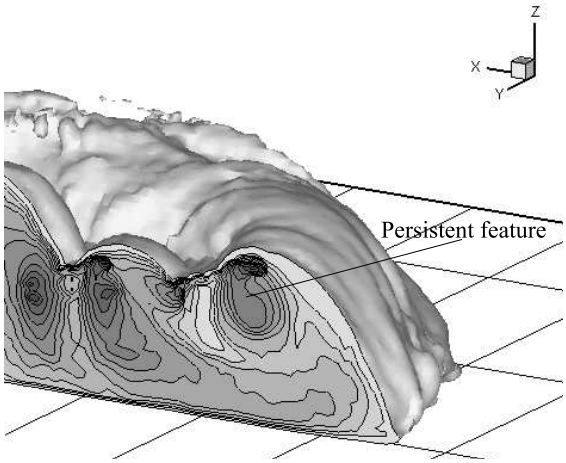

(b) *Vorticity distribution averaged over 40 rotor revolutions*

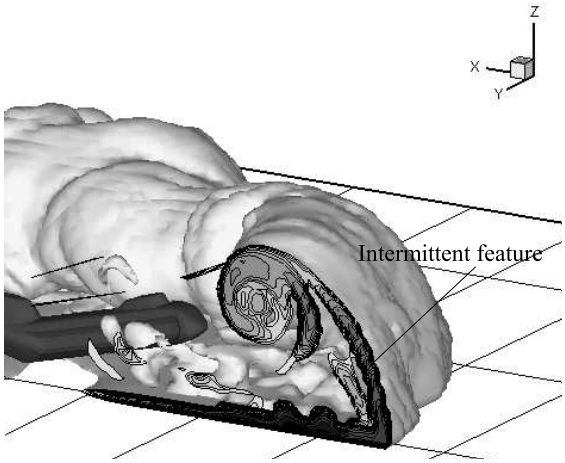

(c) *Instantaneous dust density distribution*

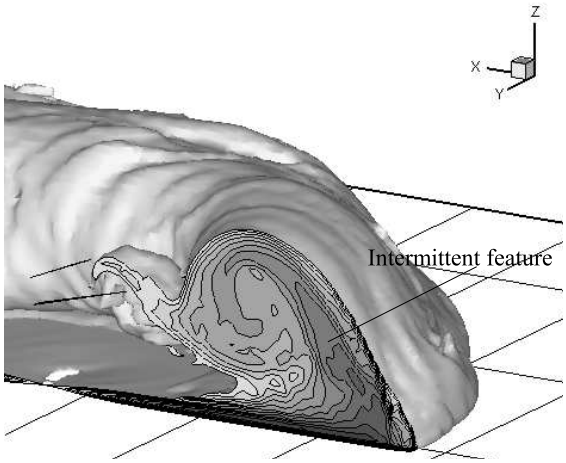

(d) *Dust density distribution averaged over 40 rotor revolutions*

Figure 5.9: *Vorticity and dust distributions in the flow below a tandem rotor helicopter at* $\mu^\star = 0.29$ *(*$\mu = 0.025$*). Darker contours represent higher values of the variable within each plot.*

in the flow field around the front of a tandem rotor configuration at an advance ratio of $\mu^\star = 0.29$ are presented. The fuselage of a generic tandem rotor helicopter is shown in Figure 5.9 (c) solely to give clarity to the positioning of the rotors. The distributions have been sectioned through the longitudinal centreline of the helicopter to reveal the internal details of the flow field. Parts (a) and (c) of the figure show the rather disordered structure of the instantaneous vorticity and dust distributions whereas the mean distributions reveal the more persistent features of the flow field. The averaged distributions contain two types of feature, namely persistent features and intermittent features. For example, one such persistent feature is the circulation of vorticity around the leading edge of the front rotor as highlighted in Figure 5.9 (b). The position and geometry of a persistent feature appear very similar in almost all of the snapshots included in the average and the strength of these features is similar in strength to the equivalent structure in the snapshots.

Also revealed by the averaging are intermittent features where the structure is more a gross representation of the flow in a particular region and may not necessarily be resembled exactly in any one snapshot. An example of one such intermittent feature is the wide band of dust travelling up from the separation zone in Figure 5.9 (d). When comparing the dust density in this region to the density in the equivalent region in the snapshot, it is revealed that the band of dust in the snapshot is much narrower than that in the average. This suggests that the path of the dust through this region differs slightly between snapshots whilst the overall structure remains fairly constant. Thus the size of the intermittent feature in the average will be larger than the structure found in the same region of any one of the snapshots. The strength of the intermittent feature will also be weaker than any individual structure as the strength will be spread over the region by the averaging process.

5.4 Wakes Generated by Hovering Rotors

As shown in § 3.2.1, when a rotor hovers above a ground plane, the effect of the ground on the power required by the rotor reduces with increasing height until, at approximately $2R$, the rotor is effectively out of ground effect. However, it was also shown that the effect of the ground on the power required by the rotor is dependent on its geometry. To determine why there is this difference between the behaviour of different rotor geometries, the flow fields which form around a variety of rotors while hovering at a range of heights above a ground plane are examined and presented.

5.4.1 Models Used

To investigate the variation in wake geometries produced by different rotors when hovering in ground effect, the VTM has been used to simulate five different rotor systems. The rotors that were simulated were the same five that were used in the investigation of power required to hover described in § 3.2.1. These rotors are those of the CH-53E, OH-6A, AH-1G, a five bladed rotor based on that of the EH-101, and the rotor used in the experiment of Lee *et al.* [4] as described in § 3.2.2. The main parameters of each rotor system are given in Table 5.1. Each rotor was simulated at various different heights above the ground, ranging from $0.5R$ to $1.5R$, to investigate how ground clearance affects the development of the wake. The thrust coefficient to which each rotor system was trimmed, except for that described by Lee *et al.*, is specified in Table 5.1. These values were held constant over the range of heights. In the experiment of Lee *et al.* the thrust of the rotor was dependent on the height of the rotor above the ground. Thus, in each individual simulation the rotor was trimmed to the thrust coefficient of the experimental system.

	Lee *et al.*	CH-53E	OH-6A	AH-1G	5-bladed
$R(m)$	0.086	12.04	4.013	6.706	9.296
$c(m)$	0.019	0.744	0.172	0.686	0.724
N_b	2	7	4	2	5
Twist (°)	0	20	8	10	8
Root cutout$/R$	0.15	0.27	0.2	0.2	0.25
$\Omega R(ms^{-1})$	27.02	223.11	203	227.38	208.23
σ	0.141	0.138	0.055	0.0651	0.124
C_T	0.013-0.019	0.0072	0.00419	0.00464	0.012

Table 5.1: *Rotor parameters of the five rotor systems used to investigate differences in wake geometries.*

5.4.2 Wake Characteristics

When considering the wake below a rotor hovering in ground effect, most views of the flow field that have been presented in the literature show the wake to extend radially outwards away from the centre of the rotor as it impinges on the ground plane. This is seen in the results from the study conducted by Lee *et al.*, as described in Chapter 3 and the corresponding simulation of the same rotor using the VTM (Figure 3.7). However, the results presented in this section show the wakes generated by a number of different rotors when hovering in ground effect, and suggest that the structure of the wake can in fact be very different to the structure that is typically presented. Although there are very few published experimental studies which detail the structure of the wake below a variety of hovering rotors, the simulations of the VTM suggest that differences in wake structure may be one of the key factors in explaining why the performance, and brownout characteristics, of different rotors can be so different.

The results presented in this section have been averaged over a number of instantaneous snapshots to reveal the most persistent features within each rotor wake, as discussed in § 5.3. Figures 5.10 to 5.14 show the averaged vorticity distributions in the flow field around each rotor when simulated at various heights above the ground. Simulation of each individual rotor system reveals clear differences in the structure of the wake. The wake that the VTM

predicts to be generated by Lee's rotor is shown in Figure 5.10. The figure reveals that the structure of the wake remains similar when the height of the rotor is altered. The tip vortices generated by the rotor blades travel down from the rotor towards the ground plane before they turn and travel radially outwards as they approach the ground. Interpretation of the averaged plots would suggest that this initial trajectory of the tip vortices could be described as a persistent feature of the flow. At approximately 1.5 radii away from the centre of the rotor the trajectory of the tip vortices becomes more unsteady. This region would be described as containing intermittent features as the structures within the flow are the same but follow a different path at different instances in time.

As shown in Figure 5.11, the wake generated by the rotor of the AH-1G is similar in structure to that generated by the rotor used by Lee *et al.* The wake generated by the rotor of the CH-53E (Figure 5.12) appears, however, to be different and shows the wake to transition between two very different structures as the rotor height changes. At the greatest rotor height of $1.5R$, the wake is similar in nature to that of the previous rotors, at the lower heights however, the structure of the wake changes. When the rotor is at a height above the ground of $1.5R$ the tip vortices stream down from the rotor towards the ground plane before moving radially outwards away from the rotor. At the lower rotor heights of $0.82R$ and $0.68R$, the transport of the tip vortices along the ground plane and away from the rotor does not occur. Instead, it would appear that, at these lower rotor heights, the wake transitions to form a different structure where the tip vortices have a tendency to recirculate in the region below the edge of the rotor disc rather than to travel out along the ground plane. A similar transition of the wake structure with rotor height is found when examining the vorticity distribution around the rotor of the OH-6A (Figure 5.13). At the greatest rotor height, the tip vortices travel downwards and away from the rotor. At the lower heights, as with the CH-53E rotor, the tip vortices appear to stay within close proximity to the rotor disc. With the OH-6A, however, the vortices form a small, recirculating region around the tips of the rotor blades rather than extending further down into the flow below the rotor disc as with the rotor of the

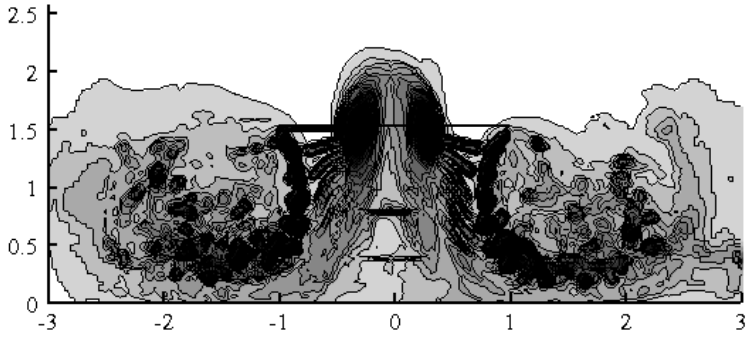

(a) *Rotor height = 1.5R above the ground.*

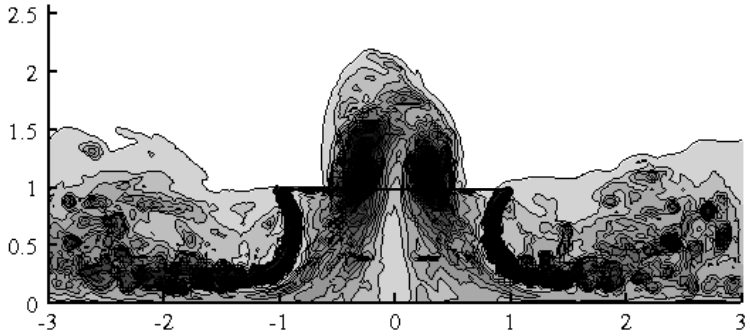

(b) *Rotor height = 1R above the ground.*

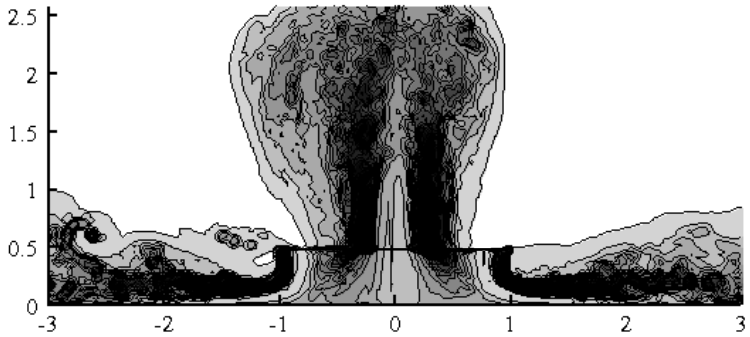

(c) *Rotor height = 0.5R above the ground.*

Figure 5.10: *Vorticity distribution around the rotor described by Lee* et al. *[4] hovering at various heights above the ground.*

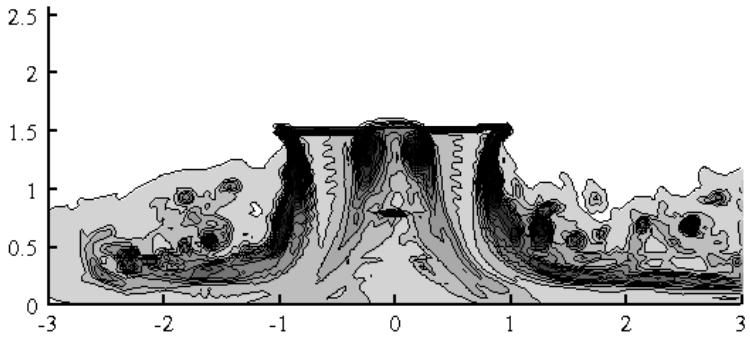

(a) *Rotor height = 1.5R above the ground.*

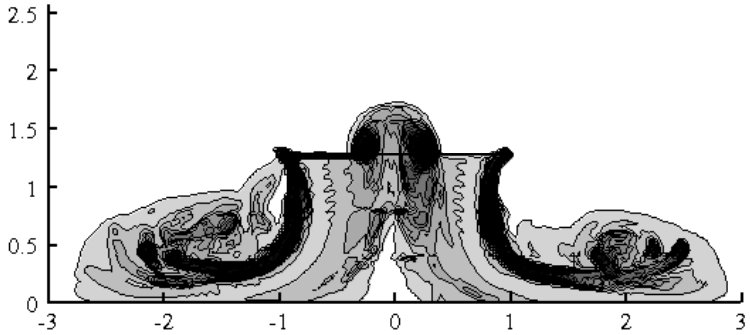

(b) *Rotor height = 1.274R above the ground.*

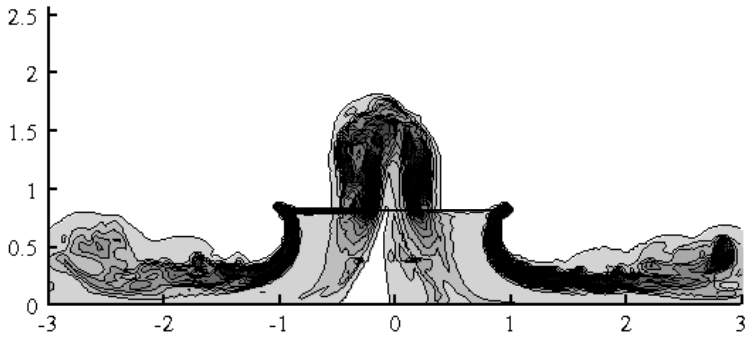

(c) *Rotor height = 0.82R above the ground.*

Figure 5.11: *Vorticity distribution around an AH-1G rotor at various heights above the ground. Height of rotor when wheels are on the ground is 0.562R.*

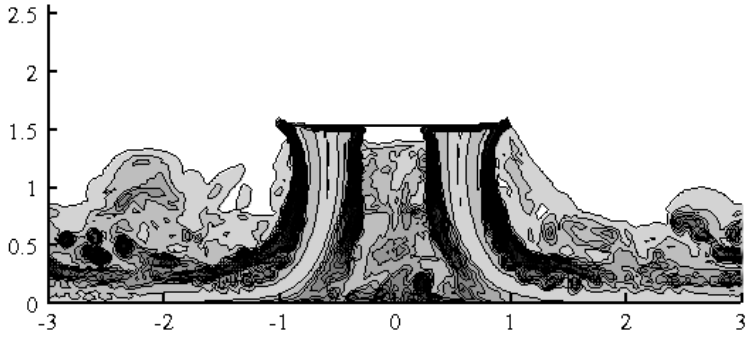

(a) *Rotor height = 1.5R above the ground.*

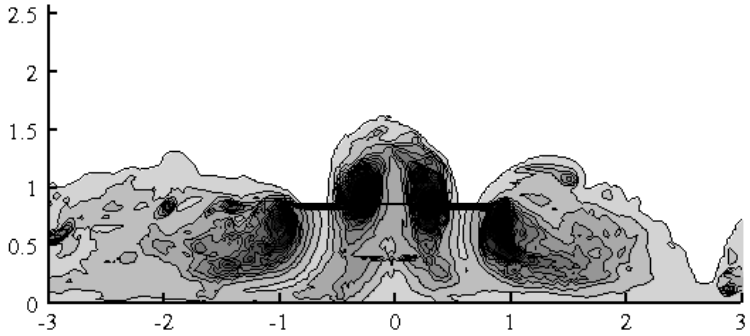

(b) *Rotor height = 0.82R above the ground.*

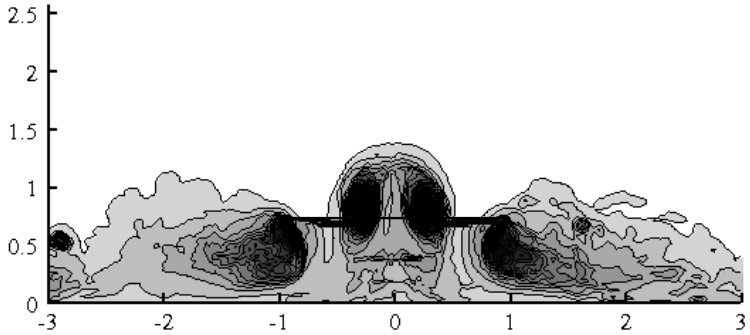

(c) *Rotor height = 0.68R above the ground.*

Figure 5.12: *Vorticity distribution around a CH-53E rotor at various heights above the ground. Height of rotor when wheels are on the ground is 0.68R.*

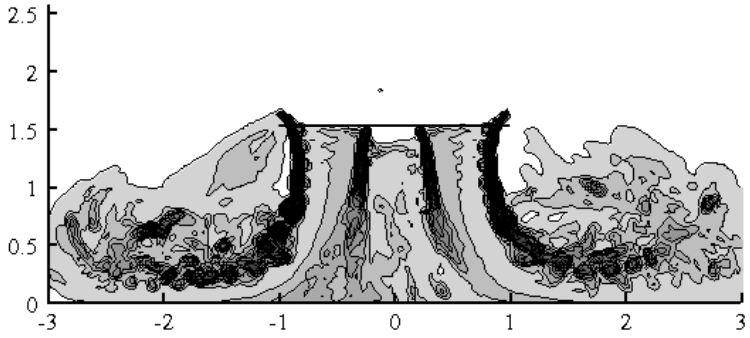

(a) *Rotor height = 1.5R above the ground.*

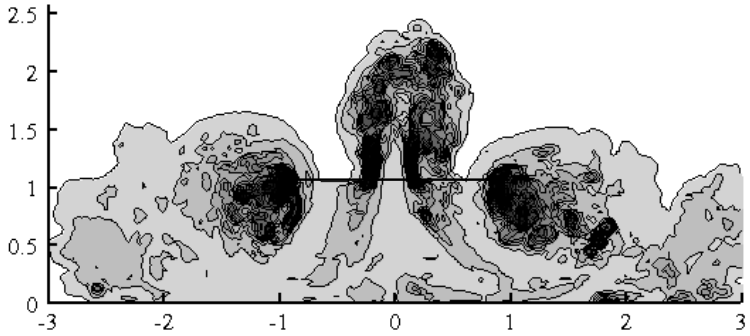

(b) *Rotor = 1.012R above the ground.*

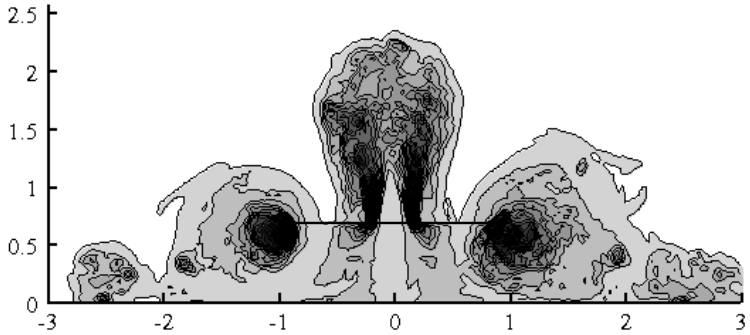

(c) *Rotor height = 0.65R above the ground.*

Figure 5.13: *Vorticity distribution around an OH-6A rotor at various heights above the ground. Height of rotor when wheels are on the ground is 0.65R.*

CH-53E.

The final rotor that was simulated, namely the generic five-bladed rotor, generates a vorticity distribution in which the predominant behaviour of the flow involves the tip vortices recirculating around the rotor blade tips regardless of the height of the rotor above the ground plane, as shown in Figure 5.14. These differences in the structure of the wakes that are generated by the various rotors appear to originate from instabilities in the wake filaments that occur very early on in the simulations. A similar breakdown in the structure of the wake is experienced when a rotor operates within the vortex ring state, as described by Ahlin and Brown [65]. Examination of the first few rotor revolutions reveals that the vorticity distributions from all five rotors are initially very similar. In all cases the tip vortices move away from the rotor disc and travel down towards the ground plane before turning and travelling radially away from the rotor. However, within the first 20 revolutions, an instability in the trajectory of the tip vortices can develop. This instability results in the very different wake structures described above. To show the development of these different wake structures, snapshots of the wake generated by the OH-6A rotor hovering at heights of $1.012R$ and $1.5R$ above the ground are shown in Figure 5.15. The snapshots are taken from the first 25 rotor revolutions of the simulation. The initial development of the wake generated by the rotor at the two different heights is similar, as shown in Figure 5.15 (a). As the calculation proceeds, the radial trajectory of the tip vortices as they approach the ground continues indefinitely when the rotor is simulated at the greater height. At the lower height, however, after approximately 16 rotor revolutions, this trajectory breaks down and the tip vortices travel back up towards the rotor and circulate in the region around the tips of the blades. This difference in the development of the wakes can be seen in Figure 5.15 (b) to (d). A similar breakdown of the initial flow structure is also found in the wake of the five-bladed rotor but this occurs at all the rotor heights that were simulated. Although the precise cause of this wake instability is still to be fully determined, the differences in the root vortex system of the rotor that are experienced when the rotor is operated in close proximity to a ground plane, combined with

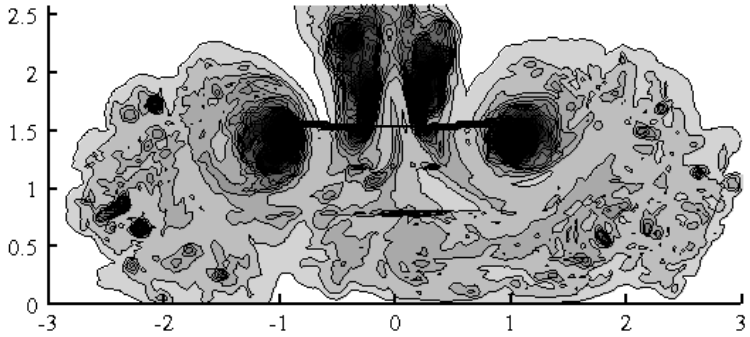

(a) *Rotor height = 1.5R*

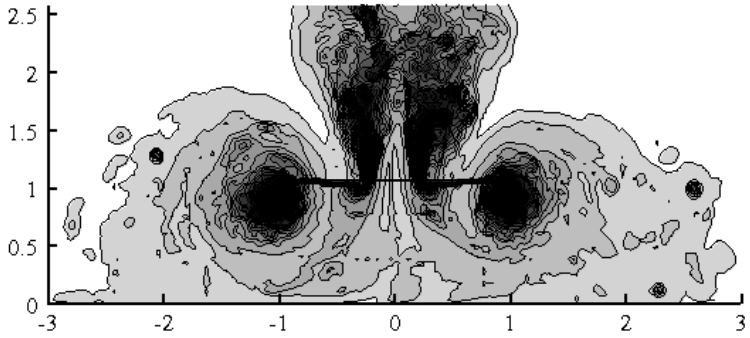

(b) *Rotor height = 1R*

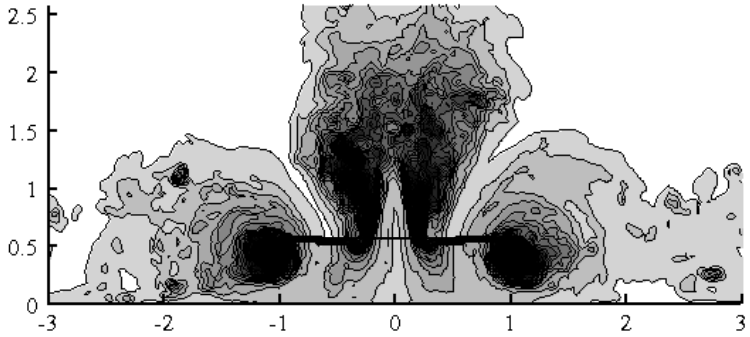

(c) *Rotor height = 0.5R*

Figure 5.14: *Vorticity distribution around the generic five-bladed rotor.*

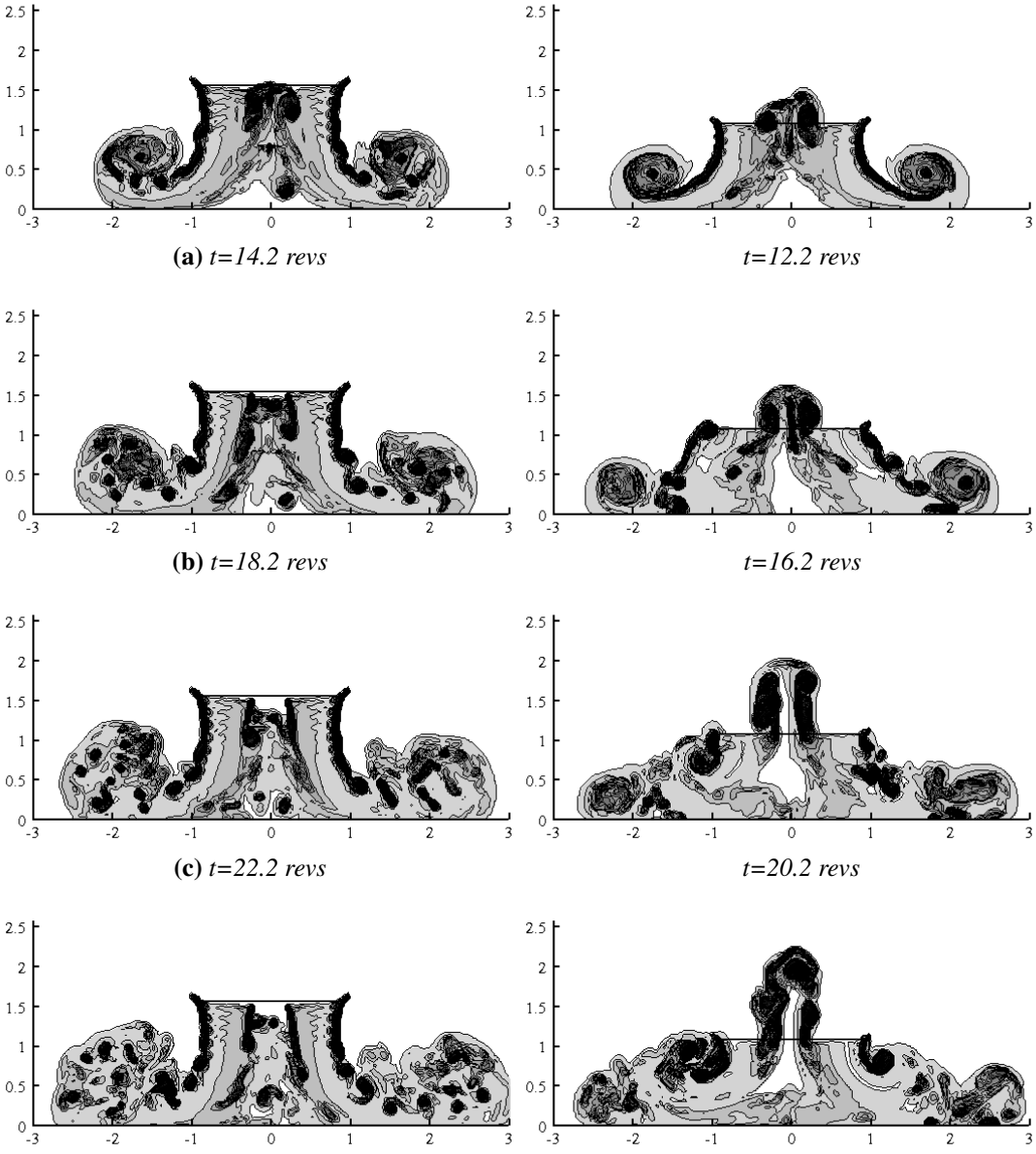

Figure 5.15: *Difference between early wake development of the OH-6A rotor when simulated at two different heights above the ground. Vorticity distribution around the rotor at height above the ground of $1.5R$ shown on the left and $1.012R$ on the right.*

changes in the velocity distribution within the wake, are most likely the reason why some rotors develop the instability while others do not.

The predictions of the VTM have shown clear differences to exist in the structure of the wakes generated by different rotors when hovering in ground effect. There are, however, no published experimental studies available in which the wake structures of different hovering rotors are examined. It would therefore be very worthwhile if such an experimental verification of the different wake structures, as described above, was conducted and made available.

5.5 Comparison of Single Rotor and Tandem Rotor Configurations

Anecdotal evidence suggests that, when carrying out a landing manoeuvre in desert conditions, helicopters with a tandem rotor configuration generate a dust cloud that is much larger and more difficult to see through than that which is produced by a typical single main rotor helicopter. The tandem rotor Chinook was involved in 30% of all brownout accidents incurred by the US Army between 2002 and 2005 yet operations involving the aircraft made up only 7% of the total helicopter flight hours [63, 64]. Thus, to investigate the effects of helicopter configuration on the structure of the wake that is generated, and the size and density of the dust cloud that forms around the helicopter, a comparison between the rotor wakes and dust distributions that are generated by a helicopter with a single main rotor and a helicopter with rotors in a tandem configuration has been conducted. Both generic tandem and single rotor configurations have been simulated at a number of advance ratios to be representative of a helicopter approaching a landing. The differences between the wakes generated by the two helicopter configurations are examined and the link between the rotor wake, induced velocity along the ground and dust entrainment is established. To determine whether helicopters in a tandem rotor configuration are indeed more prone to inducing brownout, the

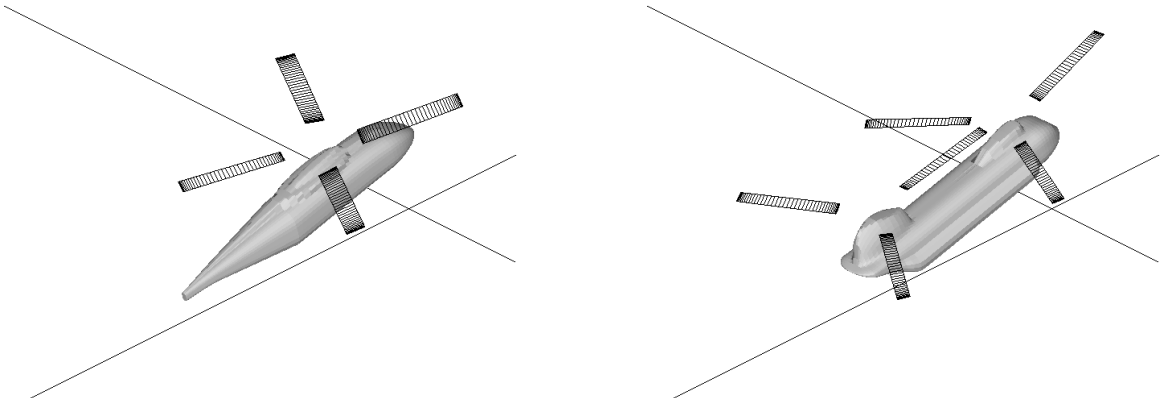

(a) *Single main rotor configuration.* **(b)** *Tandem rotor configuration.*

Figure 5.16: *Simulated helicopter geometries.*

clouds that are generated by the two rotor configurations over a range of advance ratios are then presented.

5.5.1 Model Setup

Two generic helicopter configurations were modelled, the first comprised of a single four-bladed rotor and the second with two three-bladed rotors located one behind the other. For the comparison of the dust distributions generated by the two configurations, presented in § 5.5.4, a fuselage was also simulated in each case as shown in Figure 5.16. The investigation focused on identifying the differences in wake geometries and dust distributions produced by the two configurations, thus it was required that the strength of the rotor wake produced in both cases was comparable. The two configurations were defined with the same rotor diameter and overall blade area, and both configurations were trimmed to an overall thrust coefficient of 0.0145. The systems thus have the same blade loading and thus should produce wakes of very similar strength. To be representative of helicopters during the late stages of a landing manoeuvre, both rotor configurations were simulated with a nose-up pitch attitude of 15°. To account for the centre of gravity of the aircraft being located towards the rear of the helicopter, the rear rotor of the tandem helicopter was trimmed to a slightly higher disc

loading than the front rotor. The rotors of both systems were modelled with articulated blades and trimmed to zero pitching and rolling moments about the hub. This is perhaps unrealistic in the case of the tandem rotor where a more authentic setup would require the yawing moment, experienced when the two rotors are operating at different thrust coefficients, to be trimmed out. However, only a very small overall yawing moment is experienced by the system when the two rotors are trimmed individually. The rotor blades all had a linear twist of 8°. The height of the rotors above the ground and the pitch attitude of the rotors was kept constant throughout the simulations. This is also perhaps somewhat unrealistic when considering the approach of a real helicopter to landing. However, by considering the flow fields produced by the rotors over a number of different advance ratios ($\mu^\star = 0.8, 0.47, 0.29, 0.12$), this method does give some insight into the characteristics of the dust clouds that may be produced by helicopters during landing manoeuvres.

5.5.2 Wake Structure

The role of the flow field below the helicopter in establishing the dust cloud that forms around the rotor under brownout conditions can best be understood by analysing the aerodynamics of isolated rotors in ground effect and the resultant particle dynamics. For this comparison the fuselage was not simulated so as to avoid complicating the interpretation of the flow field that is produced by the rotors. The flow produced by the two rotor configurations, as described in § 5.5.1, were simulated to examine the differences in the wakes that are generated by the two systems.

Figure 5.17 shows the vorticity distribution within the wake of the single rotor configuration at four different advance ratios ranging from $\mu^\star = 0.8$ to 0.12 to represent the rotor performing a landing manoeuvre while Figure 5.18 shows the vorticity distribution within the wake of the tandem rotor configuration at the same flight conditions as those at which the single rotor was simulated. In these figures the vorticity magnitude on a vertical slice through the longitudinal centreline of the system has been plotted after averaging the vor-

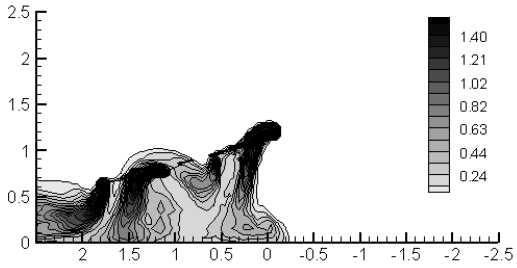

(a) $\mu^\star = 0.8$ *(*$\mu = 0.0681$*)*

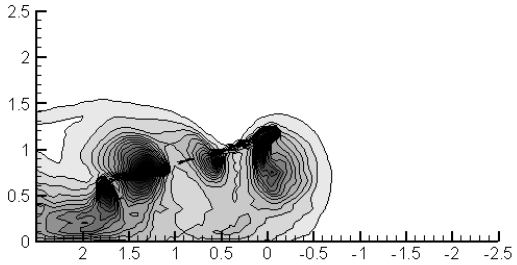

(b) $\mu^\star = 0.47$ *(*$\mu = 0.04$*)*

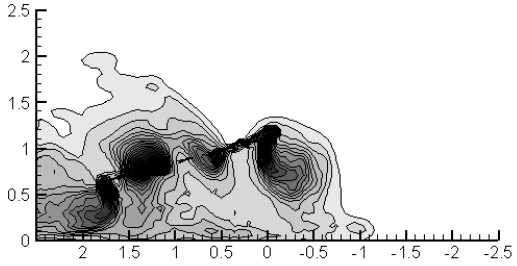

(c) $\mu^\star = 0.29$ *(*$\mu = 0.025$*)*

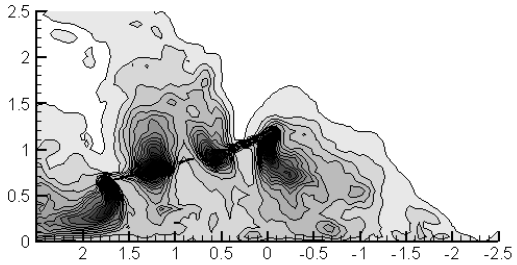

(d) $\mu^\star = 0.12$ *(*$\mu = 0.01$*)*

Figure 5.17: *Vorticity distribution in the flow below a single rotor helicopter at a range of reducing advance ratios. Darker contours represent higher values of vorticity within each plot.*

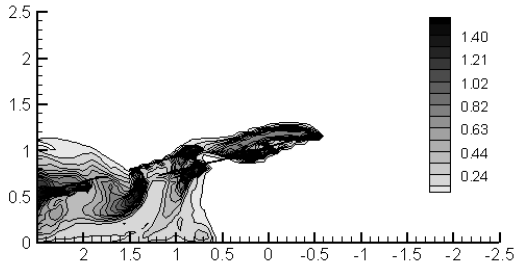

(a) $\mu^\star = 0.8$ *(*$\mu = 0.0681$*)*

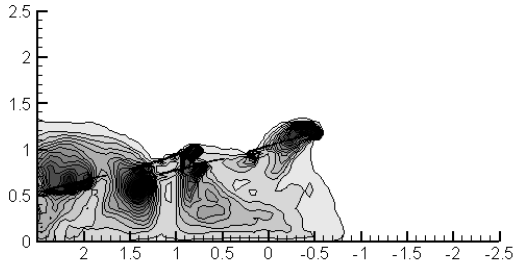

(b) $\mu^\star = 0.47$ *(*$\mu = 0.04$*)*

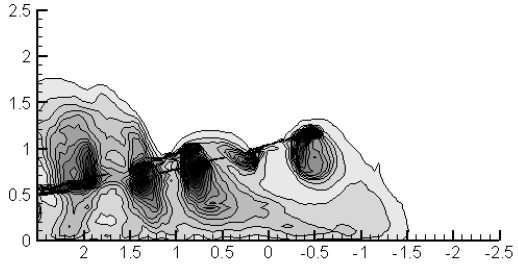

(c) $\mu^\star = 0.29$ *(*$\mu = 0.025$*)*

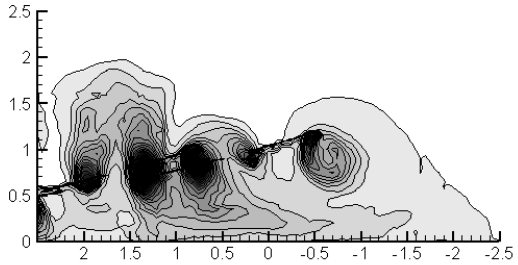

(d) $\mu^\star = 0.12$ *(*$\mu = 0.01$*)*

Figure 5.18: *Vorticity distribution in the flow below a tandem rotor helicopter at a range of reducing advance ratios. Darker contours represent higher values of vorticity within each plot.*

ticity distribution over approximately 40 revolutions. If the fuselage were present, its nose would be located at $x = 0R$.

Examination of the wake generated by the single rotor reveals that, as the advance ratio reduces, the extent of the wake in the region around the front of the rotor increases. At the greatest advance ratio of $\mu^\star = 0.8$ (Figure 5.17 (a)) a very small but steady ground vortex forms below the leading edge of the rotor. According to Curtiss *et al.* [20], an isolated rotor with zero disc tilt would be operating well within the ground vortex regime at this forward speed. It would appear, however, that the tilt of the rotor in the simulation causes the vortex to be very compact and the rotor to be, in fact, operating close to what has been described as the high speed regime. As the advance ratio is reduced, the wake that is generated forms a strong vortex below the leading edge of the rotor. At $\mu^\star = 0.47$ a rotor with zero disc tilt would be operating near the lower bound of the recirculation regime, with the disc tilt however, the rotor appears to be operating well within the recirculation regime. With further reduction in forward speed, the wake below the front of the rotor becomes less persistent. The extension of the wake along the ground plane ahead of the rotor increases and the coherent vortical structures that are visible at faster speeds are no longer apparent.

The vorticity distribution in the flow field surrounding the tandem rotor system is somewhat different to that generated by the single rotor. The tandem rotor was simulated at the same four advance ratios as the single rotor configuration. The vorticity distribution that forms within the flow field is shown in Figure 5.18. At the highest advance ratio, a ground vortex type structure forms similar to that produced by the single rotor. In comparison to the wake generated by the single rotor where the ground vortex forms below the leading edge of the rotor, the ground vortex generated by the tandem rotors is positioned below the leading edge of the rear rotor, well aft of the leading edge of the front rotor. Reducing the advance ratio to $\mu^\star = 0.47$ results in the ground vortex moving forward and forming on the ground plane below the leading edge of the front rotor. Further reduction in the forward speed to $\mu^\star = 0.29$ causes the wake to transfer from the ground vortex regime to the recirculation

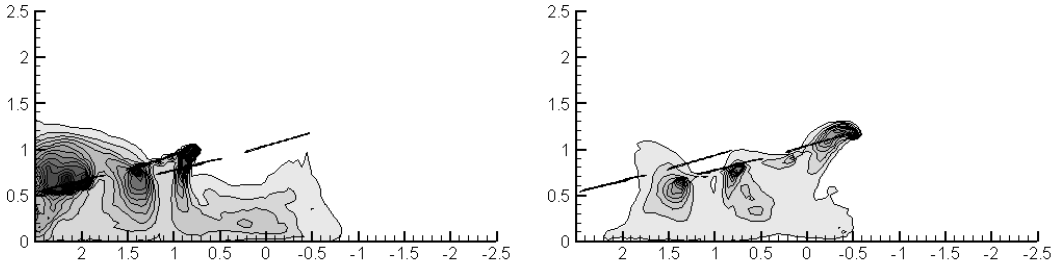

(a) $\mu^{\star} = 0.47$ *(*$\mu = 0.04$*)*

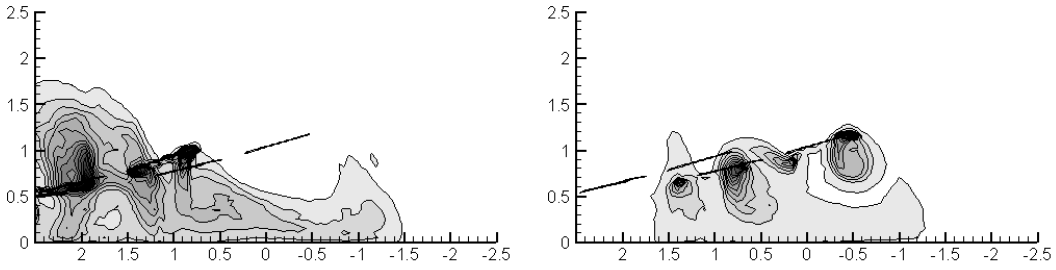

(b) $\mu^{\star} = 0.29$ *(*$\mu = 0.025$*)*

Figure 5.19: *Vorticity distribution generated by each of the two rotors in the tandem configuration. Vorticity generated by the rear rotor is shown on the left and vorticity generated by the front rotor shown on the right.*

regime where a strong vortex forms below the leading edge of the front rotor. At the lowest advance ratio that was simulated, as with the single rotor case, there is greater fluctuation within the flow field and the wake extends much further upstream than at the higher advance ratios.

To examine more closely the differences in the structure of the wake that is generated by the tandem rotor helicopter at different advance ratios, the individual vorticity fields generated by the front and rear rotors of the tandem configuration have been plotted. Figure 5.19 shows the vorticity field generated by the individual rotors when they are simulated at $\mu^{\star} = 0.47$ and 0.29. At the higher advance ratio a prominent ground vortex is formed by the rear rotor. This vortex acts to entrain the vorticity from the leading edge of the front rotor and restricts the movement of the combined vorticity field (Figure 5.18 (b)) towards the front of the helicopter. At the lower advance ratio, the character of the flow is significantly different. The vortex that forms below the leading edge of the front rotor, shown on the right

side of Figure 5.19 (b), is strong enough to entrain a significant amount of vorticity from the rear rotor. The combined vorticity field (Figure 5.18 (c)) also extends a significant distance out along the ground plane beyond the leading edge of the front rotor.

The differences in the wakes that are generated by the single and tandem rotor systems greatly affect the amount of dust that is disturbed and entrained from the ground plane. This, in turn, results in significant differences between the dust clouds generated by the two configurations as is discussed in § 5.5.4.

5.5.3 Connection Between Vorticity, Velocity and Dust Distribution

It has been shown in § 5.5.2 that, when operated in ground effect, the wake structures generated by a single rotor and a tandem rotor configuration are different when the rotors are simulated at the same advance ratio. The effect that these differences in wake structure have on the dust cloud that develops around the rotor is discussed in § 5.5.4. Prior to this however, the link between the wake generated by the rotor and the resulting dust cloud is established. The wake and dust distributions that are generated by the single rotor configuration when operating at $\mu^\star = 0.12$ and by the tandem rotor configuration when operating at $\mu^\star = 0.47$ are examined in closer detail. From this examination, the connection between vorticity, or equivalently, velocity, and dust distribution is determined.

The link between the vorticity distribution in the flow and the process of entrainment of dust from the ground plane into the flow field is revealed by comparing the time-averaged distributions of vorticity and dust in the flow field around the single rotor system, as shown in Figure 5.20. The vorticity distribution around the rotor is shown in Figure 5.20 (a) while the associated time-averaged local velocity of the flow is shown in Figure 5.20 (b). In § 4.2.2 it was shown that if the particles are small enough then their trajectory, neglecting the fallout velocity of the particles, will follow the velocity of the flow field. Figure 5.20 (c) shows a plot of a series of particle trajectories that would exist around the rotor within the time-averaged velocity field. Clearly apparent are the two stationary points immediately adjacent

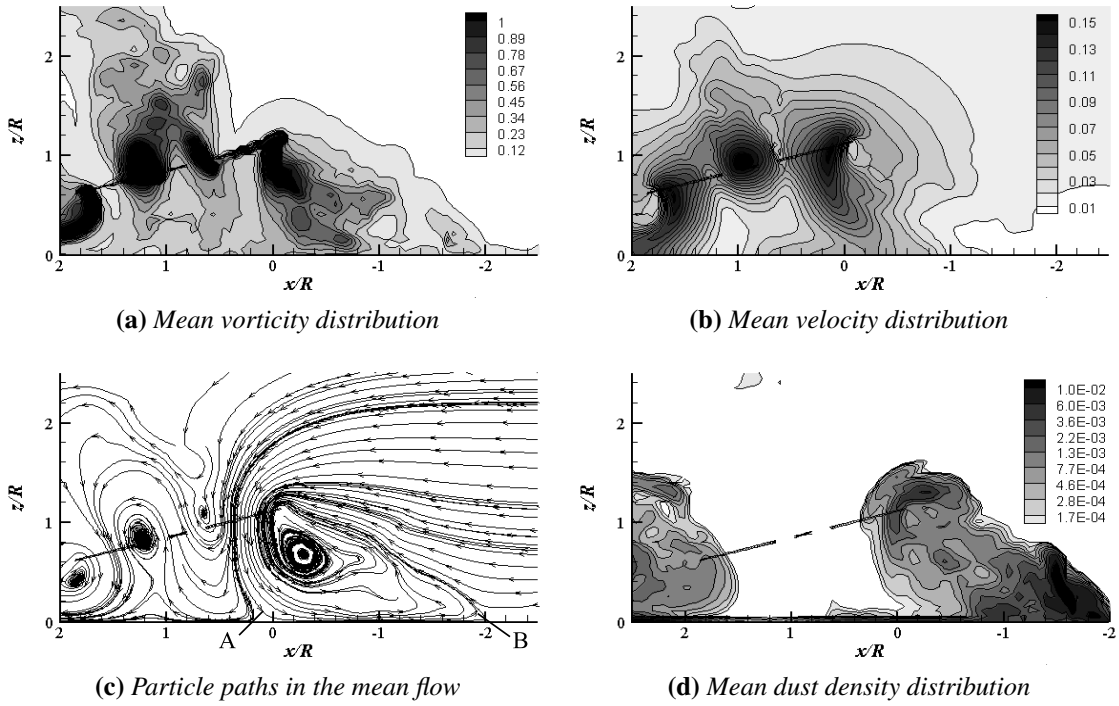

(a) *Mean vorticity distribution*

(b) *Mean velocity distribution*

(c) *Particle paths in the mean flow*

(d) *Mean dust density distribution*

Figure 5.20: *Time-averaged vorticity, velocity and dust density in the flow below a single rotor during a landing manoeuvre – normalised advance ratio* $\mu^\star = 0.12$ *(*$\mu = 0.01$*). Darker contours represent higher values of the variable within each plot.*

to the ground plane, marked A and B in the figure. Bearing in mind the unsteadiness of the flow and hence the difficulty in relating the position of these stationary points in the mean flow to the actual positions of the stagnation points in the instantaneous velocity field, point A is located near to where the rotor downwash attaches to the ground plane and point B is located near to the point at which the flow separates from the ground again. Point B occurs just upstream of the large vortical structure that extends out along the ground plane in front of the rotor. The resultant time-averaged dust distribution in the flow at this advance ratio is shown in Figure 5.20 (d).

At stationary point A the velocity along the ground plane is effectively zero. The velocity increases steadily from point A towards the front of the rotor and, as the velocity exceeds the threshold for entrainment of particles to occur, pick up of dust from the ground plane is initiated. The entrained material initially stays close to the ground plane and forms a thin,

sheet-like layer that increases steadily in density through further entrainment of dust from the ground as it convects forwards towards the front of the helicopter. The sheet-like nature of the dust distribution is maintained by the downwards trajectory of the flow beneath the rotors. As the flow extends beyond $x/R = -0.5$ the velocity decreases and the flow trajectory turns upwards away from the ground plane until, at stationary point B, the velocity is effectively zero and the trajectory is vertically upwards. This change in the flow causes the entrainment of dust to lessen before eventually ceasing, and the layer of dust along the ground plane to thicken forming the characteristic wedge-shaped separation zone of high density dust. Once the dust is lifted off the ground and exits the separation zone, the dynamics of the particles are no longer governed by the entrainment process but rather by the convective properties of the flow field. At the advance ratio represented in Figure 5.20, the relatively strong velocity field just above the separation zone leads to a large amount of dust escaping from the separation zone. The dust is drawn up into the flow and is transported up and around the front of the rotor.

By close examination of the flow field around the single rotor, it has been shown that, when modelling particle transport to simulate the brownout phenomenon, the entrainment of the dust particles from the ground plane and transport within the flow field is very much dependent on the velocities that are induced within the flow. This basic principle is also found when examining the flow field around the tandem rotor helicopter, where, as shown in Figure 5.21, the connection between the different parameters of the flow field is very similar to that of the single rotor. The generic features of the entrainment and transport of the particles into the flow field are described by the schematics shown in Figure 5.22. These schematics represent a model for how the dust cloud around a single rotor helicopter forms, based on the helicopter operating within the ground vortex regime. Representations of the vorticity, velocity and dust distributions within the flow field around the single rotor helicopter, when viewed at two different scales, are shown in the figure. The schematics drawn at the coarse scale represent the distributions that would be revealed in a simulation where the individual

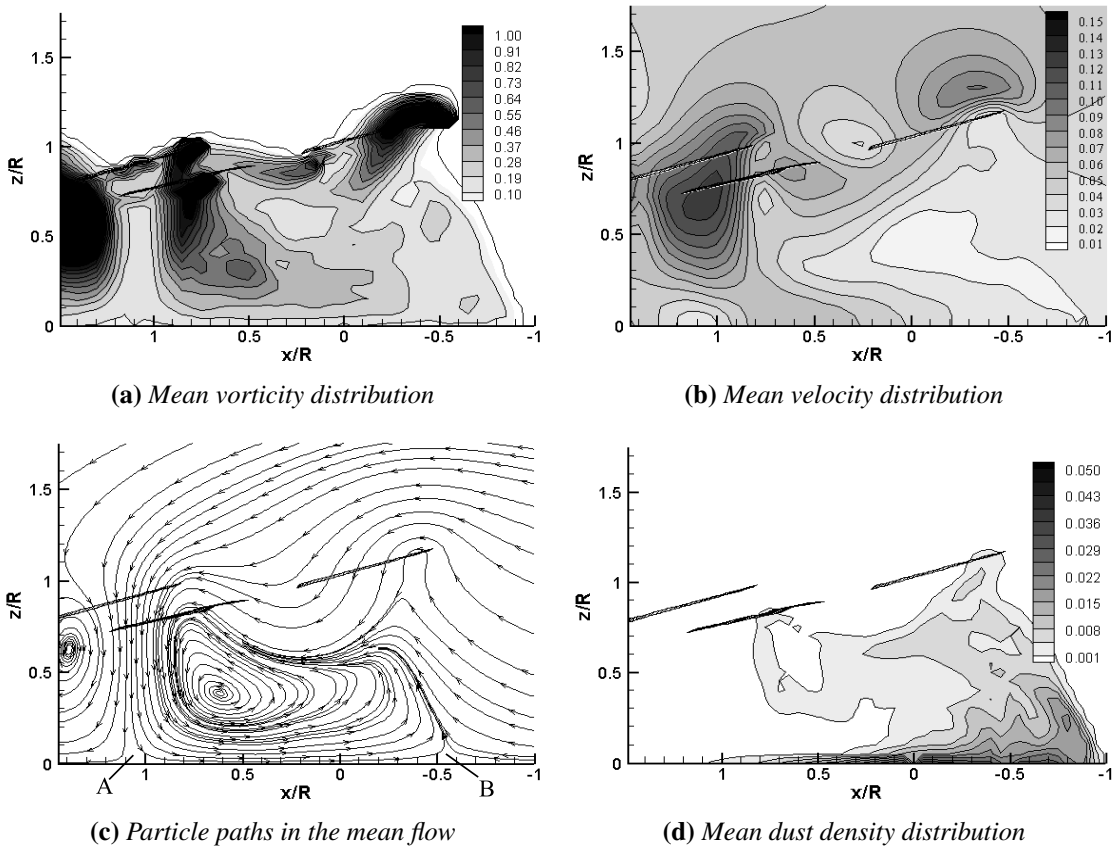

(a) *Mean vorticity distribution*

(b) *Mean velocity distribution*

(c) *Particle paths in the mean flow*

(d) *Mean dust density distribution*

Figure 5.21: *Time-averaged vorticity, velocity and dust density in the flow below a tandem rotor during a landing manoeuvre – normalised advance ratio $\mu^\star = 0.47$ ($\mu = 0.04$). Darker contours represent higher values of the variable within each plot.*

tip vortices are not resolved, while at the finer scale the schematics represent the distributions that would be revealed when the tip vortices are resolved. The tip vortices travel down from the rotor towards the ground plane inducing a velocity along the ground. At the coarse scale (shown in the left hand column of the figure) the individual tip vortices are not resolved whereas at the finer scale they are (Figure 5.22 (a)). The velocity field that is induced by the vorticity is shown in Figure 5.22 (b). There are two stationary points, A and B, where the velocity at the ground is effectively zero. The initial entrainment of dust occurs close to point A, as shown in Figure 5.22 (c), once the velocity of the flow has increased sufficiently to pass the threshold velocity as described in § 4.2.3. The dust is then transported by the flow but stays in close proximity to the ground plane before accumulating at the second station-

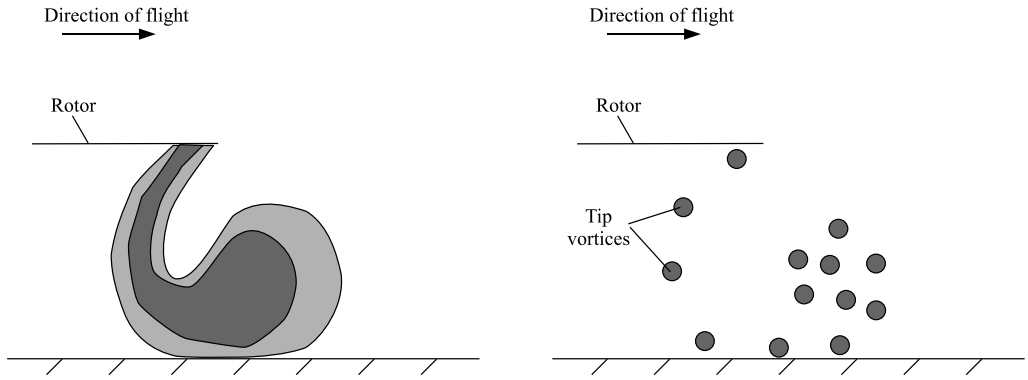

(a) *Vorticity distribution*

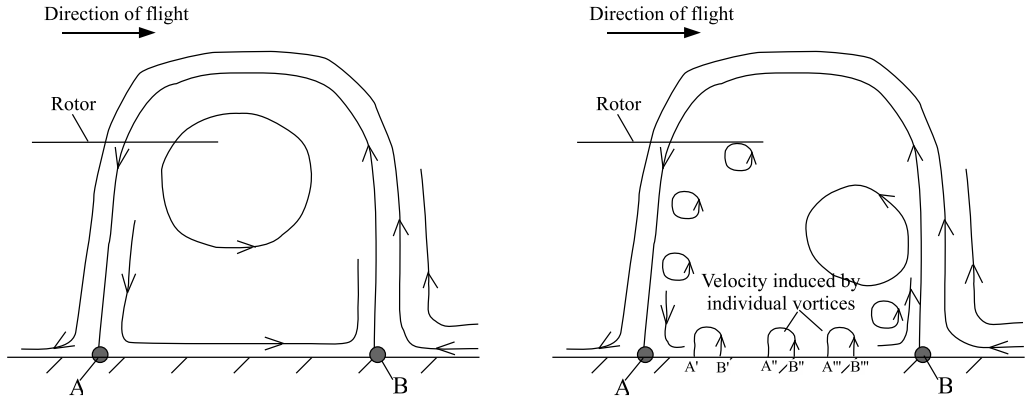

(b) *Velocity distribution*

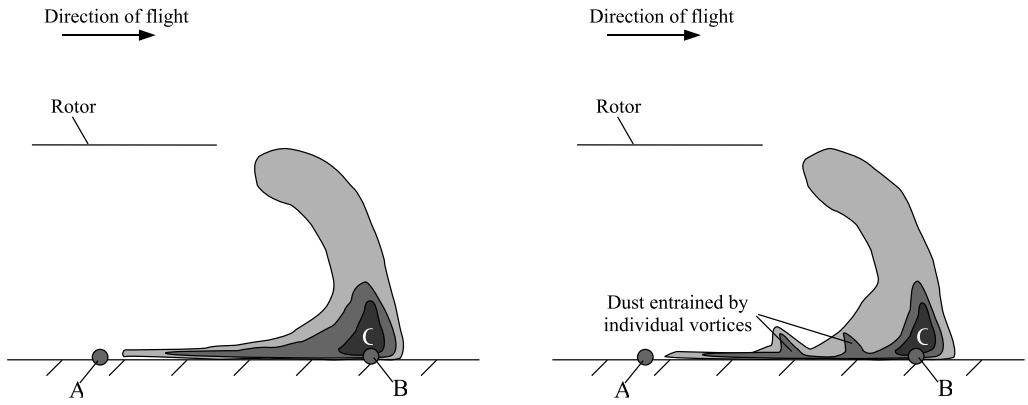

(c) *Dust distribution*

Figure 5.22: *Schematic of the process of dust entrainment along the ground plane for a single rotor helicopter. Flow field represented at coarse scale shown in left hand column and at fine scale shown in right hand column.*

ary point at B which lies within what has been termed the 'separation zone' by Nathan and Green [3], located at position C. This zone is apparent in almost all experimental visualisations of dust clouds generated by rotors operating above dusty surfaces [3, 5] as discussed in § 4.4. When the tip vortices are resolved, each individual vortex induces a velocity around itself. As the vortices travel along the ground plane, dust is entrained into small, wedge-shaped zones in front of each vortex. These small zones of entrained dust accumulate in the separation zone. The dust in the separation zone is then transported into the flow around the rotor by the velocity within the flow field.

The general physics that governs the entrainment of dust from the ground plane when a wake from a single rotor helicopter interacts with it has been shown in Figure 5.22. Schematics representing the flow field around a tandem rotor helicopter are shown in Figure 5.23. The governing physics of the entrainment process below the tandem rotor is the same as that below the single rotor. The only difference between the flow fields generated by the two configurations is the vorticity that is generated by the front rotor in the tandem configuration which becomes entrained into the ground vortex of the rear rotor. The entrainment of dust from the ground plane is governed by the action of the induced velocity within the flow field and thus, the size and density of the resulting dust cloud is dependent on the behaviour of the rotor wake.

5.5.4 Dust Distribution

It was shown in § 5.5.2 that the overall formation of the wakes that are generated by the single rotor and tandem rotor configurations, when operating at the same advance ratio, can vary, while the physics that governs the entrainment of dust from the ground plane into the flow field, as described in § 5.5.3, remains consistent. In this section it will be shown how the differences in wake geometry around the single rotor and tandem rotor configurations affect the size and density of the dust cloud that forms in the flow field around each helicopter.

Both the single rotor and tandem rotor geometries have been simulated in ground effect

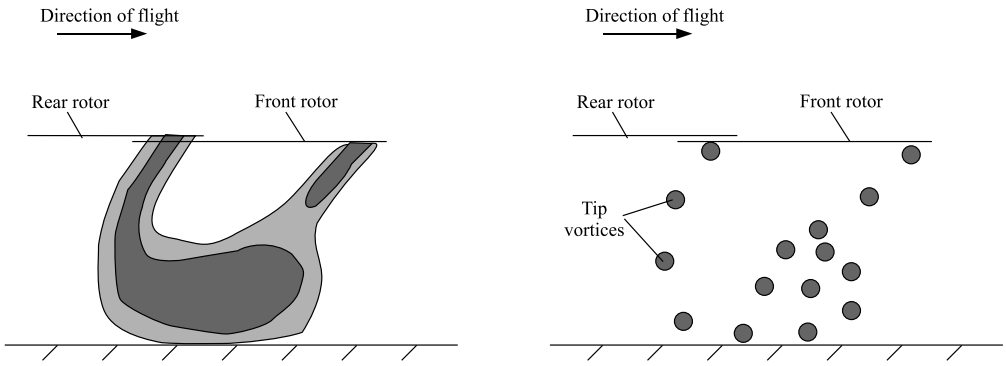

(a) *Vorticity distribution*

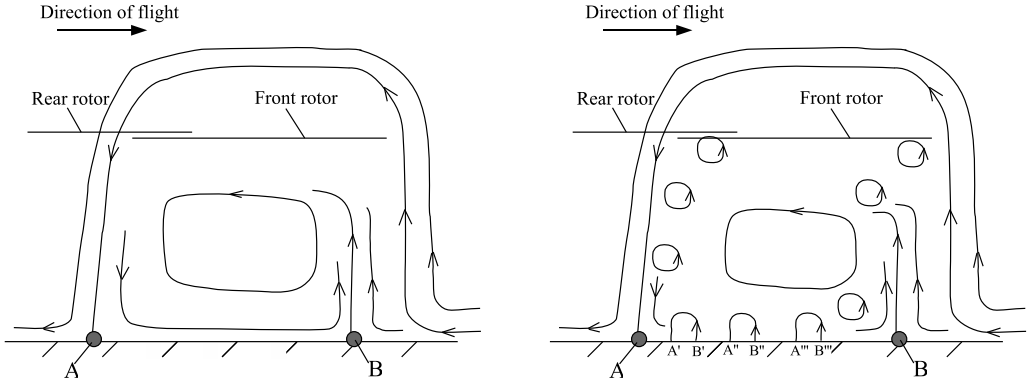

(b) *Velocity distribution*

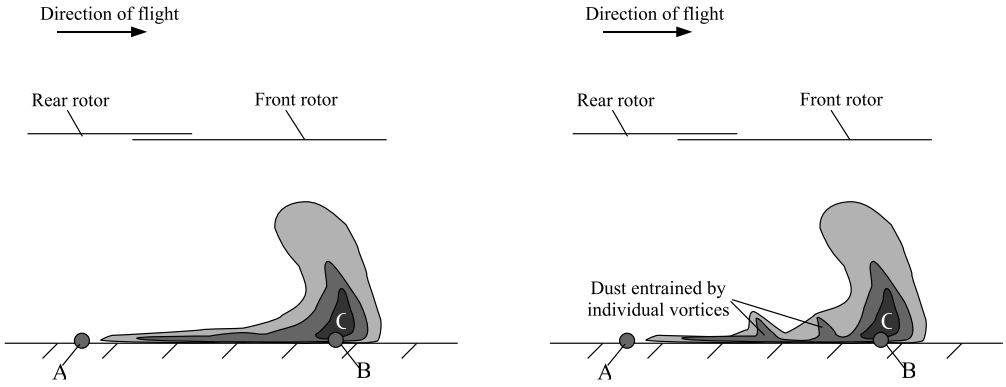

(c) *Dust distribution*

Figure 5.23: *Schematic of the process of dust entrainment along the ground plane for a tandem rotor helicopter. Flow field represented at coarse scale shown in left hand column and at fine scale shown in right hand column.*

using the VTM. The dust density distribution produced by each configuration has been calculated and the results are presented in Figures 5.24 to 5.31 which show the change in dust distribution as the forward flight speed is reduced. In each of the figures, parts (a) and (b) show, using an iso-surface of constant dust density, a snapshot of the dust density distribution within the flow field. Part (a) gives a three-dimensional view of the flow field while part (b) shows the flow field from a side perspective. This second view allows the vertical extent of the dust cloud in relation to the height of the helicopter to be appreciated. The third image in each figure shows contours of the average dust density distribution on a vertical slice through the flow on a plane that coincides with the centreline of the fuselage. The minimum contour level shown in the contour plots has the same value as the iso-surface used to generate the 3-D plots. The contour plots show the dust density in the flow around the helicopter averaged over 60 rotor revolutions. The data for these figures of average dust distribution was taken at a time far enough into the simulation so that the flow had settled into its long term behaviour thus avoiding any contamination of the data by vortical or particulate structures that arise in the initial conditions of the system. These average plots highlight the most persistent features within the dust cloud.

Figures 5.24 and 5.25 show the dust cloud that is created by the two configurations when they are flying above the ground at the relatively high advance ratio of $\mu^\star = 0.8$. At this advance ratio, both configurations operate in the ground vortex regime as described in § 3.3.1. At this forward speed, however, and with the inclination of the fuselage and rotor discs, the ground vortex forms some distance behind the leading edge of the rotors and is relatively compact (as shown in Figures 5.32 (b) and 5.33 (b)). The position of this interaction of the ground vortex with the ground plane thus results in the dust entrainment occurring some distance behind the nose of the aircraft. A low, crescent-shaped ridge of dust marks the front of the dust cloud below the aircraft. This ridge forms along the forward edge of the ground vortex that is generated by the helicopter and extends outwards and downstream. At this relatively high forward speed and with the nose of the aircraft pitched up, the interaction

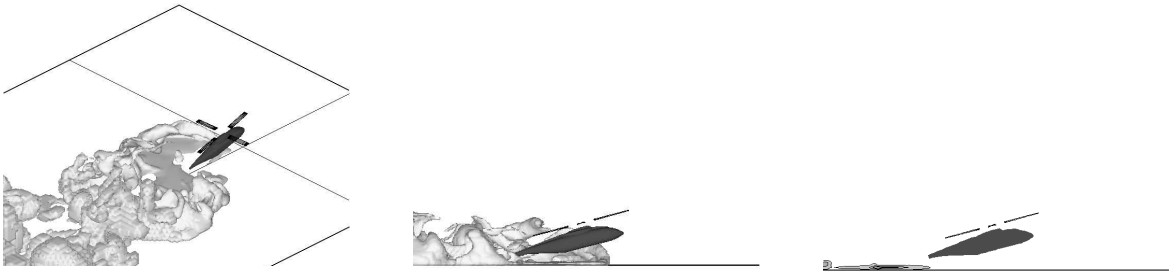

(a) (b) (c)

Figure 5.24: *Dust distribution surrounding a helicopter with single main rotor configuration ($\mu^\star = 0.80$).*

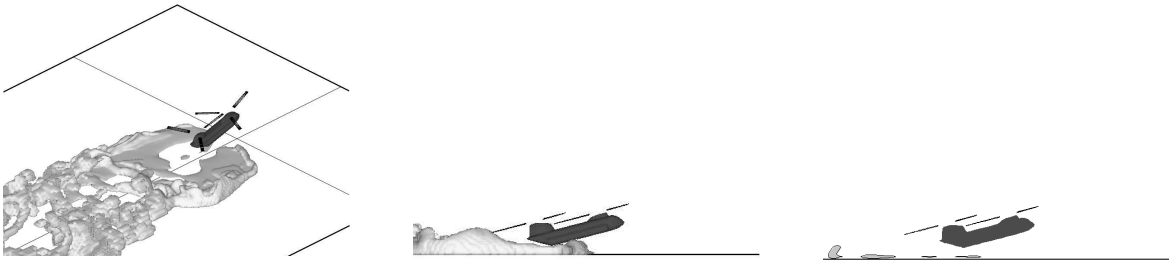

(a) (b) (c)

Figure 5.25: *Dust distribution surrounding a helicopter with tandem-rotor configuration ($\mu^\star = 0.80$).*

between the front and rear rotors of the tandem configuration appears to cause the ground vortex to be located further back than the ground vortex that is produced by the helicopter with the single rotor.

The iso-surface plots show there to be a distinct asymmetry in the dust distribution that is generated by the helicopter with the single main rotor. It should be noted that the rotor in the single rotor configuration was simulated to rotate anti-clockwise when viewed from above. This asymmetry can be explained by comparing the vorticity distribution created by the two configurations to the corresponding dust distribution (Figures 5.32 and 5.33). The iso-surface used to represent the vorticity distribution has been chosen to reveal the strongest vorticity that is present in the flow. The powerful crescent-shaped vortex which forms below each rotor system is clearly shown but the plot also reveals that this structure is highly asymmetric for the single rotor configuration. The core of the ground vortex remains significantly closer to the ground plane on the left hand side of the aircraft than on the right as

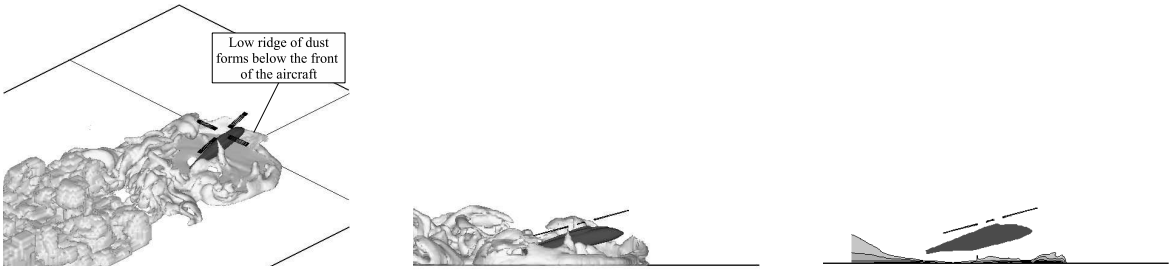

Figure 5.26: *Dust distribution surrounding a helicopter with single main rotor configuration ($\mu^\star = 0.47$).*

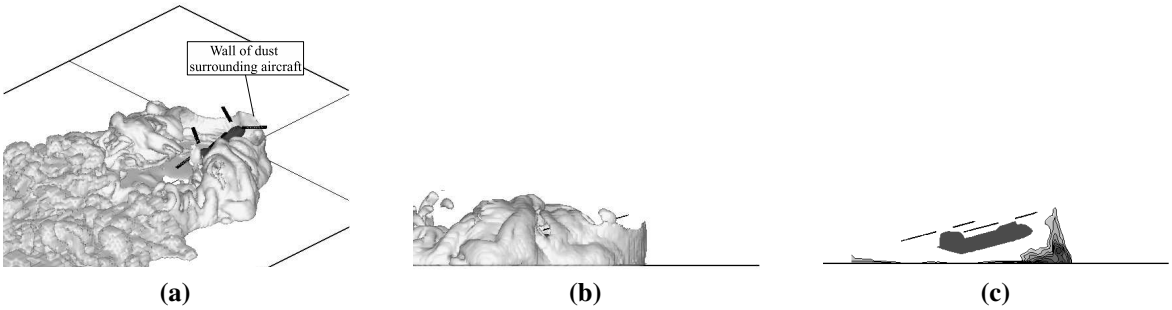

Figure 5.27: *Dust distribution surrounding a helicopter with tandem-rotor configuration ($\mu^\star = 0.47$).*

the helicopter moves forward along the ground. The tandem rotor configuration, on the other hand, generates a ground vortex that has a far more symmetric structure. The asymmetry in the dust cloud shown in Figure 5.32 (c) can then be explained by the correlation between the region of maximum entrainment of dust and the position and strength of the ground vortex.

As the advance ratio of the aircraft decreases, the dust clouds which develop in the surrounding flow field form closer to the front of the aircraft. Figures 5.26 and 5.27 show the dust cloud that the VTM predicts to form around the helicopters once they have decelerated to an advance ratio of $\mu^\star = 0.47$. At this forward speed, the wake of an isolated, horizontal rotor would exist within the recirculation regime. The rearwards tilt of the rotors in the simulations presented here, however, causes a fairly large ground vortex to form just forward of the helicopter instead. Most interestingly, the iso-surface plot of dust density distribution around the helicopter with the single rotor shows a fairly broad region in which the dust remains sheet-like and very close to the ground. In contrast, the dust cloud generated by the

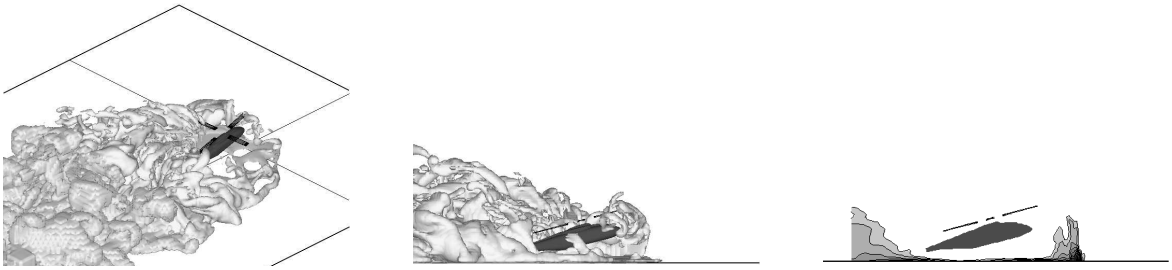

(a) (b) (c)

Figure 5.28: *Dust distribution surrounding a helicopter with single main rotor configuration ($\mu^\star = 0.29$).*

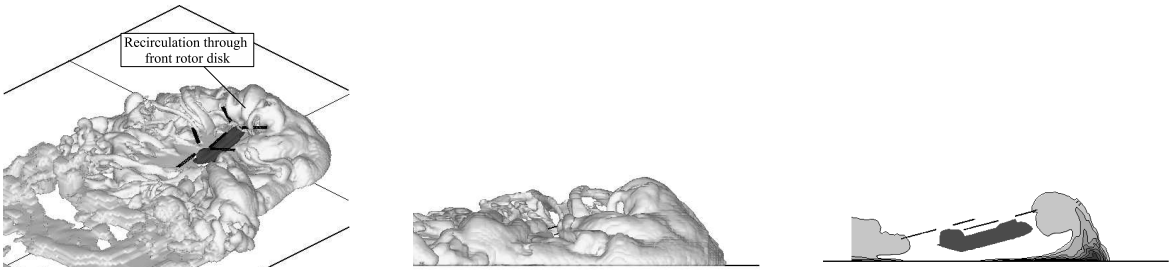

(a) (b) (c)

Figure 5.29: *Dust distribution surrounding a helicopter with tandem-rotor configuration ($\mu^\star = 0.29$).*

tandem rotors has significant vertical extent.

Further deceleration of the helicopters results in a significant enlargement of the dust cloud that surrounds the aircraft, particularly around the tandem configuration as the wake circulates around the front rotor disc. Figures 5.28 and 5.29 show the dust distribution in the flow with the aircraft travelling at $\mu^\star = 0.29$. At this advance ratio the rotors operate well within the recirculatory regime. A comparison of the averaged dust density on the longitudinal slice through the flow shows the tandem rotor configuration produces a dust cloud that is far larger and more persistent than the cloud that is produced by the single rotor configuration.

Deceleration to the slowest speed that was simulated results in both configurations becoming engulfed in a large and persistent cloud of dust. Figures 5.30 and 5.31 show the predicted dust clouds when the aircraft are flying at the very low forward speed of $\mu^\star = 0.29$. Significant recirculation of dust through the rotor discs is evident in both cases. It is quite

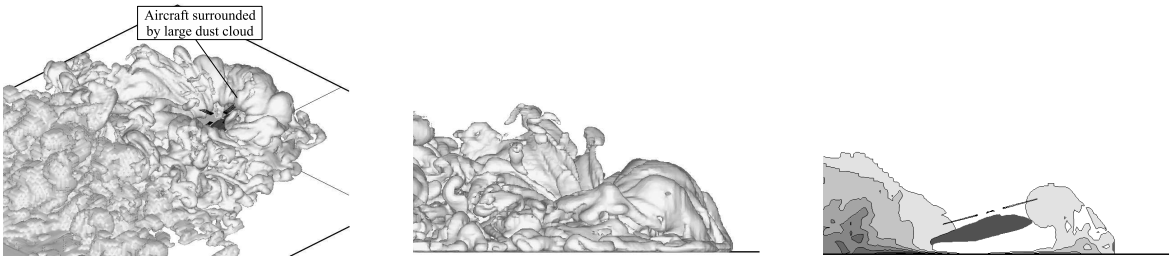

(a) **(b)** **(c)**

Figure 5.30: *Dust distribution surrounding a helicopter with single main rotor configuration ($\mu^\star = 0.12$).*

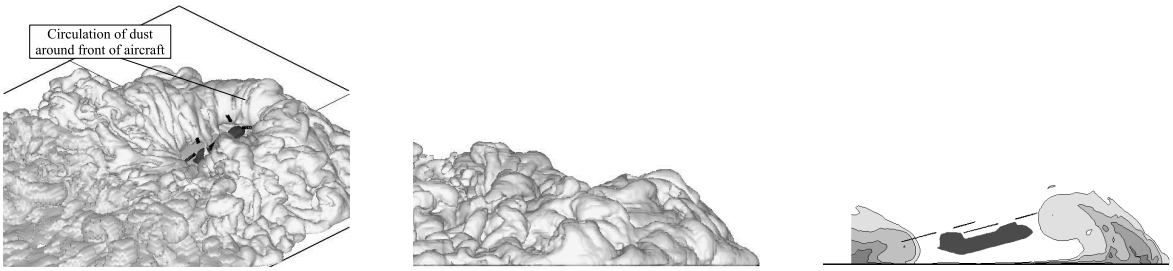

(a) **(b)** **(c)**

Figure 5.31: *Dust distribution surrounding a helicopter with tandem-rotor configuration ($\mu^\star = 0.12$).*

plausible that in practical circumstances in this situation the helicopter might be considered to be encountering brownout where it is highly likely that the pilot's view of the landing area will have become obscured.

5.6 Summary

To investigate how the configuration of a rotor system affects the geometry of the wake which develops around it, the VTM has been used to simulate a number of different isolated rotors hovering in ground effect. The wakes that were generated by the rotors were found to vary significantly in geometry and size not only between rotors but, in some cases, when the height of the rotor above the ground was changed. In the simulations some of the rotors produced wakes that extended down towards the ground before travelling radially outwards and forming a jet wake type structure along the ground plane, while other rotors generated

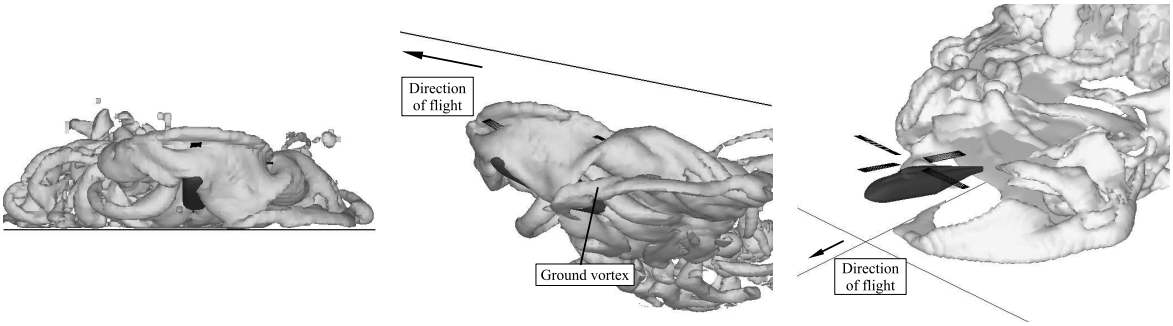

(a) *Vorticity distribution (viewed from the front of the helicopter).* **(b)** *Vorticity distribution (viewed from below the ground plane).* **(c)** *Dust density distribution.*

Figure 5.32: *Correlation between the vorticity distribution surrounding a helicopter with single main rotor and the regions of maximum entrainment of dust. ($\mu^{\star} = 0.80$).*

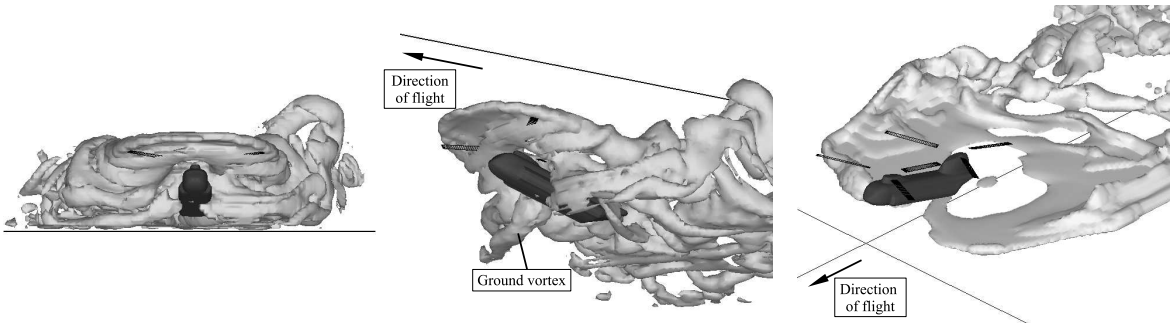

(a) *Vorticity distribution (viewed from the front of the helicopter).* **(b)** *Vorticity distribution (viewed from below the ground plane).* **(c)** *Dust density distribution.*

Figure 5.33: *Correlation between the vorticity distribution surrounding a tandem-rotor helicopter and the regions of maximum entrainment of dust. ($\mu^{\star} = 0.80$).*

wakes in which the dominant vortical structure was located around the blade tips. This wake behaviour appears to be dependent on the geometry of the rotor and its height above the ground. The actual parameter that controls the instability, which results in these different wake structures, is not, as yet, fully determined. A further investigation has been presented in which the wake and dust distribution around a single rotor configuration and tandem rotor configuration helicopter have been compared. It was shown that differences in the wake structures generated by the two configurations do exist when the rotors are operated at the same advance ratio. By examining the connection between the vorticity and velocity within the flow field and how this affects the dust cloud that is produced, it has been shown that the

entrainment and transport of dust is very much dependent on the induced velocities within the flow. Finally, the dust clouds generated by the single rotor and tandem rotor configurations at a number of advance ratios have been shown. The differences in the overall wake structures produced by the two rotor configurations result in the dust clouds that are generated by the helicopters also being very different in size and density. The results have shown that the rotors in a tandem configuration appear more susceptible to brownout. The results presented in this chapter have revealed that, while the vortical structures that are shed and trailed from the blades of each rotor remain consistent between rotors, the overall structure of the wake that develops appears to be rotor depended. Thus, as the formation of the dust cloud in the flow field around the helicopter is related to the behaviour of the rotor wake, changing the helicopter configuration can result in significant variation in the size and density of the dust cloud that is generated.

Chapter 6

Effect of Rotor Design on Helicopter Brownout

6.1 Introduction

With the recent resurgence of helicopter operations in desert environments there has been a renewed interest in the problems associated with the suspension of dust particles in the air flow surrounding helicopters. There are two different approaches to overcoming the problem of brownout – either by coping with the condition or by avoiding it all together. The first of these approaches uses instruments which allow the pilot to 'see through' the clouds of dust that form, such as in the systems described by Sykora [66] and Jansen *et al.* [67]. Although this technique may provide a short-term solution it does not prevent the aircraft from encountering the dust cloud. Not only can brownout be potentially dangerous but operation in dense dust clouds may affect the efficiency of the system and, over time, the dust can cause significant damage to the helicopter rotor and engines. Thus, when looking for a long-term solution to the problem of brownout, avoiding the situation completely or reducing the severity of the dust clouds that develop, through aerodynamic means, would be beneficial so as to avoid the costs associated with damage to the helicopter components.

Computational modelling of particle transport in the helicopter context is still in its relative infancy, however interest in the area is ever increasing. Haehnel *et al.* [7], Wachspress *et al.* [8] and D'Andrea [10] amongst others are all developing and implementing computational models which include the transport of particles to investigate brownout. Whitehouse *et al.* [6] have extended their computational predictions by conducting experimental investigations to examine the effects of aerodynamic design on the development of brownout. Other computational studies such as those by Wadcock *et al.* [11] focus on the behaviour of the flow field with particular interest in the downwash generated by the rotor and how this affects brownout. With all these computational models becoming more accurate and reliable, a fully aerodynamic solution to the brownout problem may well be found through computational investigations. This chapter presents the results of a study which was conducted using the VTM to examine the effect of altering various rotor parameters on the development and density of the dust cloud that is produced by a rotor operating in close proximity to a dusty surface. This investigation allows some insight to be gained into the dependency of the size and density of the dust cloud on the rotor design.

6.2 Rotor Configuration

The VTM has been used to simulate a rotor operating in slow-speed forward flight and in hover above a ground plane to examine how, when one of a number of parameters of the rotor configuration is altered independently of the others, the dust cloud produced by the rotor changes. A fictitious rotor, designed to be representative of the EH-101 in terms of its dimensions and operating conditions was used as a baseline rotor about which each chosen rotor design parameter was varied. The baseline rotor consisted of five rectangular blades, as shown in Figure 6.1, attached to an articulated rotor hub. A summary of the parameters of the baseline rotor is given in Table 6.1. This study was focused on examining the characteristics of an isolated rotor thus no fuselage was included in the simulations.

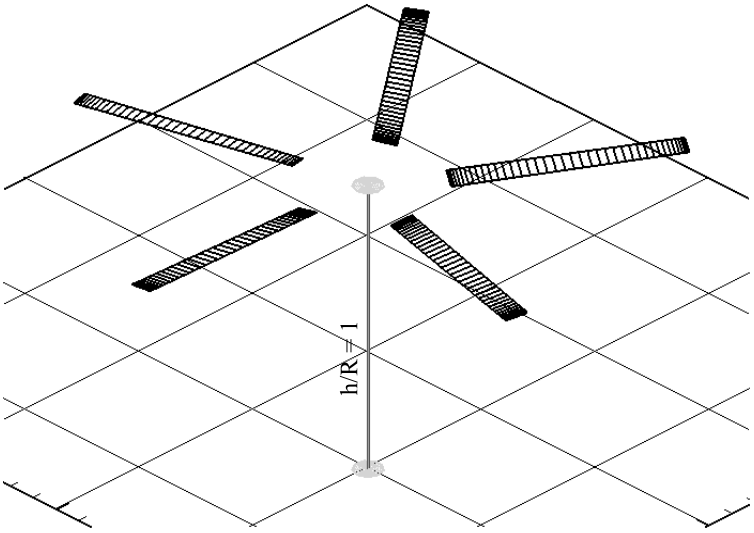

Figure 6.1: *Geometry of the baseline rotor.*

Rotor radius	9.3 m
Number of blades	5
Root cutout	$0.25R$
Solidity	0.124
Twist	-8° (Linear)
Flap/lag hinge offset	$0.05R$
Chord	$0.078R$
Aerofoil section	NACA23012

Table 6.1: *Summary of baseline rotor parameters*

6.3 Description of the Overall Flow Field

The dust clouds which develop around helicopters when the rotor wake interacts with a dusty surface form when the rotor is in close proximity to the ground and travelling at low forward speeds. For this reason, brownout is most often encountered when the helicopter is landing or taking off. To approximate a landing manoeuvre, three separate calculations were conducted to represent intermediate stages of the approach. At each stage the rotor is simulated in a steady flight case. In two of the cases, the rotor is modelled with forward speed at thrust normalised advance ratios of $\mu^\star = 0.6, 0.3$, and for the third case the rotor is modelled in

hover. This series of flight conditions is simulated to represent the rotor decelerating into hover. This method of breaking the landing manoeuvre down into intermediate stages allows an understanding of the features of the flow field at each speed to be obtained whilst avoiding the high computational costs associated with simulating a continuous manoeuvre. The rotor is trimmed to zero disc tilt and to a constant thrust coefficient $C_T = 0.012$ throughout – except for the simulations in which the effect of disc loading is examined. For all the simulations presented in this chapter, the centre of the rotor hub is positioned at a height of $1R$ above the ground.

To highlight the differences in the wakes produced by the baseline rotor at the three different advance ratios, three-dimensional snapshots of the flow field surrounding the rotor at each speed are shown in Figures 6.2 to 6.4. Iso-surfaces representing the vorticity and dust density are plotted for each advance ratio with the vorticity shown by the light surface and dust density shown by the dark surface. Examination of the vorticity distribution around the rotor at the three advance ratios reveals that, at the highest advance ratio, a ground vortex forms below the leading edge of the rotor disc while at $\mu^\star = 0.3$ the flow appears to recirculate around the front of the disc. When the rotor is in hover it is seen that the wake breaks down into a large number of small scale structures as a result of the natural instability in the flow field. The majority of these structures recirculate around the rotor disc to form a toroidally shaped wake. As discussed in Chapter 5, the structure of the wake produced by this particular rotor whilst in hover is somewhat different to the wakes produced by many other rotors. The basic physics relating the development of the velocity field to the formation of the dust cloud is nevertheless consistent for all rotors, as described in § 5.5.3. Figures 6.2 (b) to 6.4 (b) show combined surfaces of vorticity and dust density and reveal, that, when the ground vortex forms below the front of the rotor disc at the higher advance ratio, there is also a cloud of dust that forms in the same region. At the lower advance ratio there appears to be considerably less dust in the region below the front of the rotor than is seen at the higher advance ratio. It must be remembered however that these figures are instantaneous snapshots

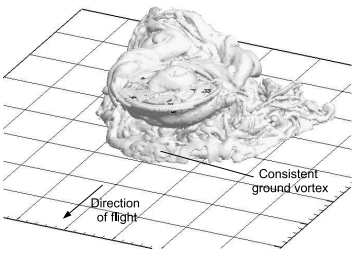

(a) *Vorticity*

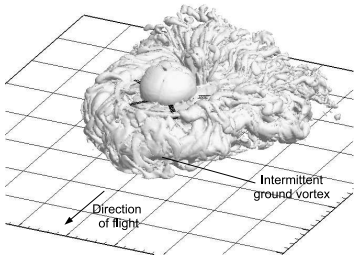

(a) *Vorticity*

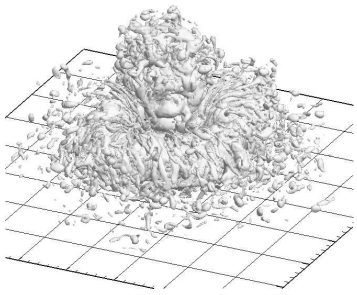

(a) *Vorticity*

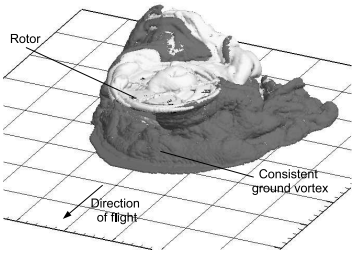

(b) *Vorticity and dust density*

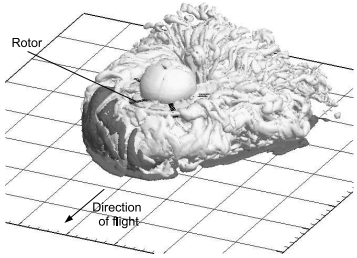

(b) *Vorticity and dust density*

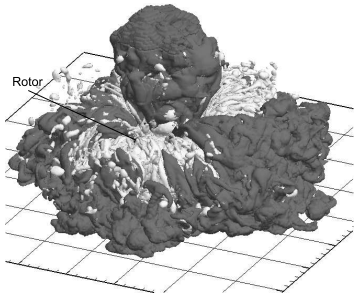

(b) *Vorticity and dust density*

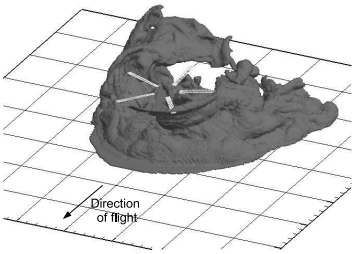

(c) *Dust density*

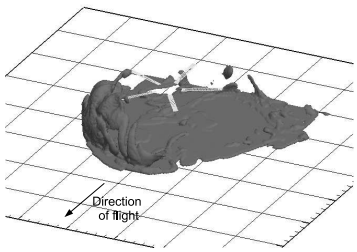

(c) *Dust density*

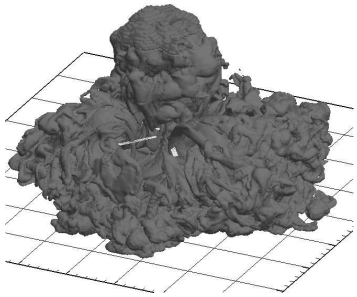

(c) *Dust density*

Figure 6.2: $\mu^\star = 0.6$.

Figure 6.3: $\mu^\star = 0.3$.

Figure 6.4: $\mu^\star = 0.0$.

of the flow fields and that the structure of the dust cloud that forms at the lower speed is intermittent due to the recirculatory nature of the flow. The wake produced by the rotor at the lower speed will be discussed in more detail later in this section. When the rotor is in hover, the dust cloud that develops extends only a small distance outboard of the rotor disc, with the majority of the dust forming a similar recirculatory structure as does the vorticity around the rotor disc.

To lend further insight into the processes that govern the entrainment of dust from the ground plane and the formation of the dust clouds within the air flow surrounding the rotor, the relationship between velocity, vorticity and dust density distributions, as was previously discussed in § 5.5.3, are examined. Figures 6.5 to 6.7 show the flow field that is produced by the baseline rotor at the three different thrust-normalised advance ratios. Presented in these plots are instantaneous snapshots of the vorticity, velocity magnitude and dust density distributions on a longitudinal plane through the centre of the rotor. Also shown is a map of the instantaneous particle trajectories through the flow.

At the highest advance ratio ($\mu^\star = 0.6$) a vortex is formed on the ground plane below the leading edge of the rotor (Figure 6.5 (a)) as was also seen in Figure 6.2 (a). This ground vortex remains fairly static with only minimal changes in its size and position as the simulation progresses. By comparing the snapshots shown in Figure 6.5 (a) and (c) with the plots of the averaged flow field shown in Figure 6.8 it can be inferred that the changes in size of the vorticity and dust distributions over time are small. Examination of the velocity distribution in Figure 6.5 (b) shows the largest velocities in the flow close to the ground plane to occur immediately below the vortex. The initial entrainment of dust from the ground plane into the flow field occurs at the downwind edge of the ground vortex. The dust stays in a thin layer close to the ground as it is transported in the flow. At approximately $-1R$, i.e. forward of the rotor, the trajectory of the flow turns away from the ground plane and the velocity field transports the entrained dust up into the circulating region of flow that is associated with the ground vortex.

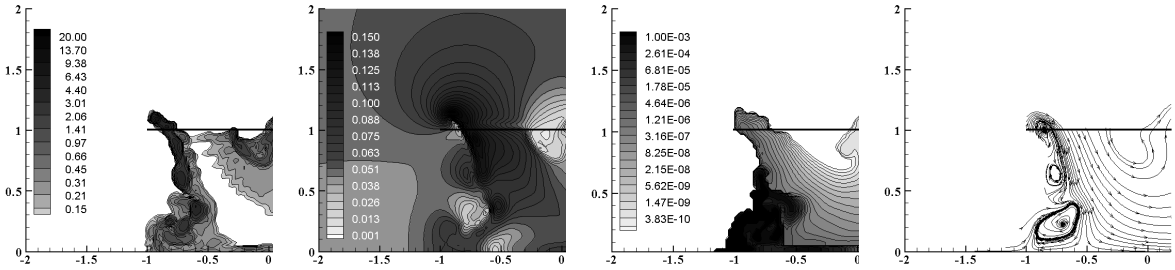

(a) *Vorticity distribution* **(b)** *Velocity distribution* **(c)** *Dust distribution* **(d)** *Flow trajectories*

Figure 6.5: *Snapshot of flow field parameters near the front of the rotor disc at a thrust-normalised advance ratio $\mu^\star = 0.6$. Scales consistent for $\mu^\star = 0.3$ and hover.*

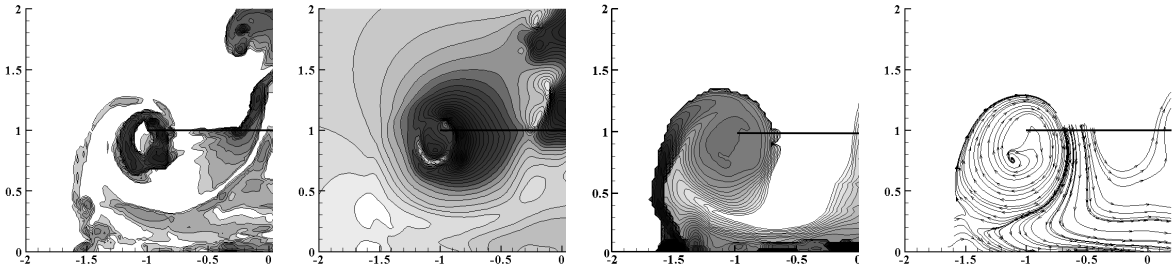

(a) *Vorticity distribution* **(b)** *Velocity distribution* **(c)** *Dust distribution* **(d)** *Flow trajectories*

Figure 6.6: *Snapshot of flow field parameters near the front of the rotor disc at a thrust-normalised advance ratio $\mu^\star = 0.3$.*

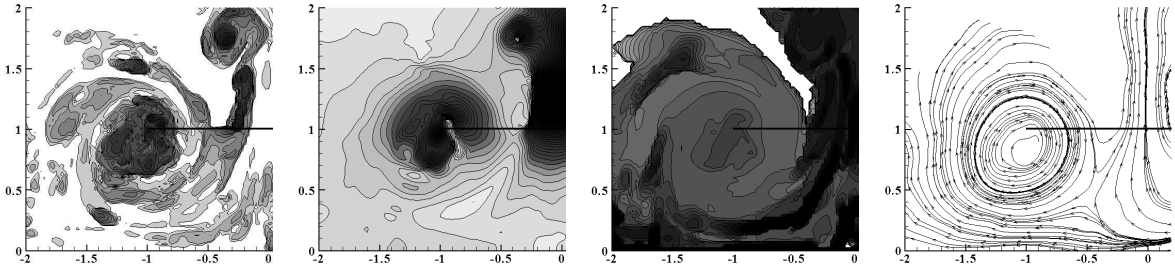

(a) *Vorticity distribution* **(b)** *Velocity distribution* **(c)** *Dust distribution* **(d)** *Flow trajectories*

Figure 6.7: *Snapshot of flow field parameters around the rotor in hover.*

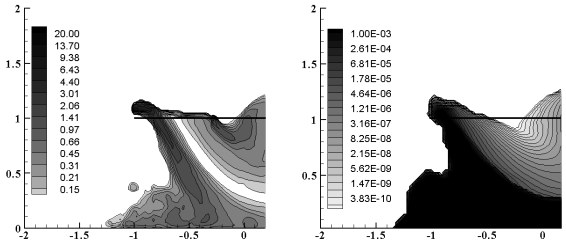

(a) *Vorticity distribution* **(b)** *Dust distribution*

Figure 6.8: *Flow field parameters near the front of the rotor disc at a thrust-normalised advance ratio $\mu^\star = 0.6$. (Averaged over 60 rotor revolutions.) Scales consistent for $\mu^\star = 0.3$ and hover.*

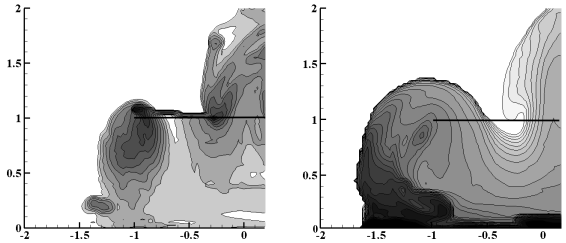

(a) *Vorticity distribution* **(b)** *Dust distribution*

Figure 6.9: *Flow field parameters near the front of the rotor disc at a thrust-normalised advance ratio $\mu^\star = 0.3$. (Averaged over 60 rotor revolutions.)*

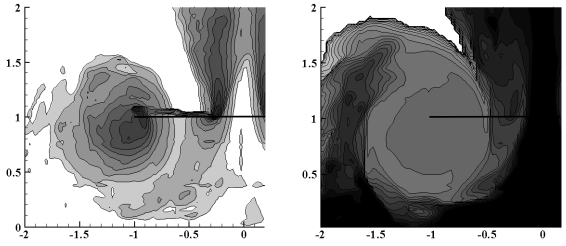

(a) *Vorticity distribution* **(b)** *Dust distribution*

Figure 6.10: *Flow field parameters near the front of the rotor disc while the rotor is in hover. (Averaged over 60 rotor revolutions.)*

As the advance ratio is reduced, the structure of the wake becomes less regular. Similar images to those shown in Figure 6.5 are given in Figure 6.6 but for the rotor at a forward speed of $\mu^\star = 0.3$. At this advance ratio and at the particular instant in time shown in the figure, the wake recirculates around the leading edge of the rotor rather than forming a ground vortex as is the case at faster forward speeds. This recirculation is intermittent with the wake regularly breaking down to form less coherent structures. As the wake extends out in front of the rotor, separation of the wake from the ground plane usually occurs around $-1.5R$. It is at this point that the majority of the dust is lifted from the ground either to become trapped in the recirculation zone around the front of the rotor or to be transported into the flow downstream of the rotor.

Evidence of the highly unsteady nature of the flow which develops around the rotor at $\mu^\star = 0.3$ is revealed by comparing the instantaneous snapshots of vorticity and dust density distribution shown in Figure 6.6 with the averaged distributions as shown in Figure 6.9. The average plots show the recirculation of vorticity and dust through the front of the rotor that was observed in the instantaneous snapshots. Closer inspection of the instantaneous and averaged distributions reveals a difference in the overall size and shape of the distribution below the front of the rotor. This difference is particularly noticeable in the vorticity distribution.

As the advance ratio reduces further towards the rotor being in hover, there is a significant increase in the size and density of the dust cloud that is produced. The dust density distribution in the flow field around the hovering rotor, along with the other flow parameters, is shown in Figure 6.7. Comparison of these to the average distributions presented in Figure 6.10 shows a similarity between the average and instantaneous plots such that the flow field produced by a hovering rotor appears to be far more constant than that which develops at $\mu^\star = 0.3$. While the rotor is in hover, some of the entrained dust becomes trapped in the recirculating region which forms around the edge of the rotor disc while a significant portion of the dust rises in a plume up through the centre of the rotor. A similar effect was discussed by Fradenburgh [18] when describing the structure of the wake below a rotor hovering in

ground effect. Part of the vorticity below the rotor was found to flow radially inward, then, at the axis of rotation, it would converge and flow vertically upwards. A similar upwards velocity in the simulations presented here results in the large plume of dust forming above the rotor. The instantaneous plot of dust distribution shows the highest dust densities to exist within this plume and in the flow close to the ground plane. Conversely, the lowest dust densities are found within the recirculating region around the edge of the rotor disc.

The intermittent nature of the rotor wake at the lower advance ratio of $\mu^\star = 0.3$ is investigated in more detail by considering the development of the wake over a number of rotor revolutions. Figure 6.10 shows how both the vorticity and dust density distributions develop over approximately 18 rotor revolutions. The corresponding interval over which the revolutions occur is far enough into the simulation for the initial transients in the wake to have dissipated. At the first instant in time (Figure 6.10 (a)) there is a region of strong vorticity located below the leading edge of the rotor disc, but this region appears to interact only weakly, if at all, with the ground plane. As a result there is no new entrainment of dust from the ground plane below the front of the rotor disc. The dust that does exist in the flow field towards the rear of the rotor disc is a result of previous interactions between the wake and the ground. As time proceeds, a vortex can be seen (specifically, between 57.5 and 62.5 rotor revolutions) to break away from the region of vorticity below the leading edge of the rotor and then to travel down towards then along the ground plane. Examination of the dust distribution over the same time period shows the dust that was already present in the flow field to be transported back behind the rotor whilst, on the ground below the front of the rotor, a new region of dust is formed as a result of the disturbance of dust on the ground. Initial entrainment of dust occurs when the vortex first reaches the ground plane and continues as the vortex travels along the ground. Once the dust has been entrained from the ground plane, it is then free to be transported in the flow field. Figure 6.10 (e) shows the dust to be transported away from the ground plane and up towards the rotor disc. While the vortex moves away from the ground and back up to the region directly below the rotor, the transport of

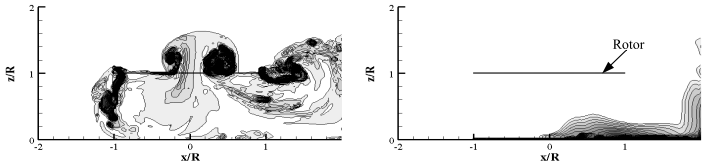

(a) *t = 54.2 rotor revolutions*

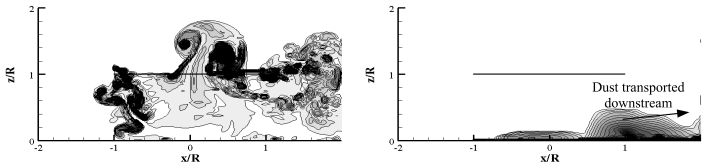

(b) *t = 55.8 rotor revolutions*

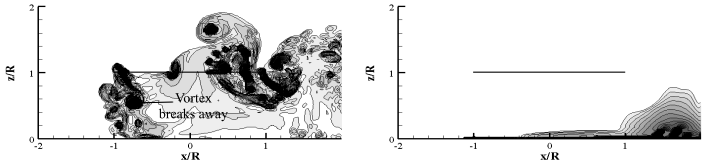

(c) *t = 57.5 rotor revolutions*

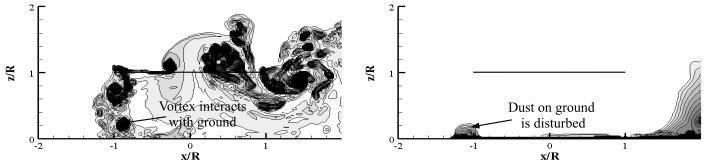

(d) *t = 59.2 rotor revolutions*

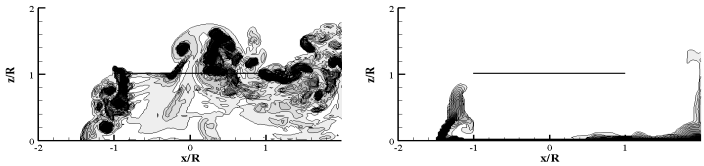

(e) *t = 60.8 rotor revolutions*

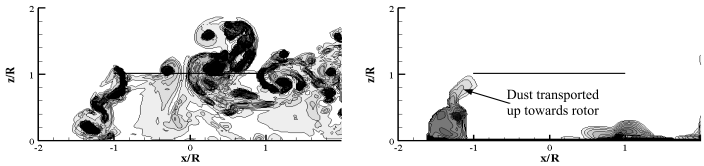

(f) *t = 62.5 rotor revolutions*

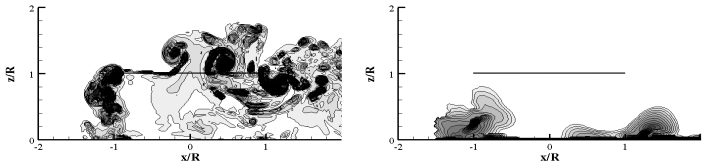

(g) *t = 64.2 rotor revolutions*

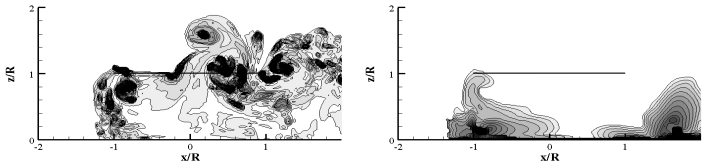

(h) *t = 65.8 rotor revolutions*

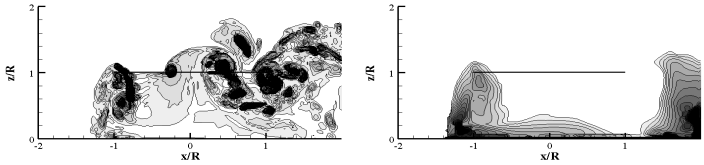

(i) *t = 67.5 rotor revolutions*

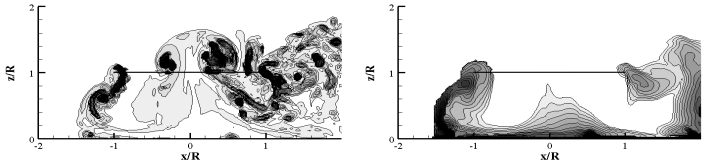

(j) *t = 69.2 rotor revolutions*

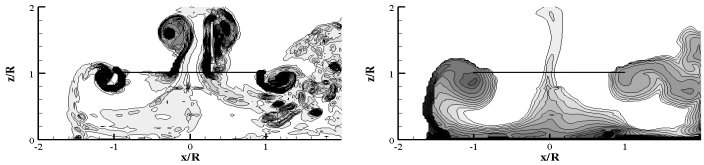

(k) *t = 70.8 rotor revolutions*

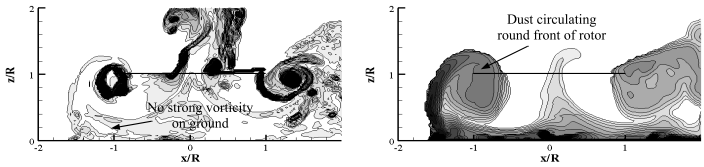

(l) *t = 72.5 rotor revolutions*

Figure 6.10: *Development of vorticity and dust density distributions over 18 rotor revolutions around the baseline rotor operating at $\mu^\star = 0.3$. Vorticity is shown on the left of each subfigure and dust density on the right.*

dust under the action of the velocity field within the region between the rotor and the ground continues, eventually forming a large cloud around the front of the rotor disc.

This intermittent breakdown of the wake and the corresponding entrainment of dust from the ground plane result in the flow field that is generated by the rotor at $\mu^\star = 0.3$ being less structured than that generated at $\mu^\star = 0.6$. The cyclic manner in which the vortical structures breakdown and travel towards the ground plane continues to occur repetitively as the simulation develops further. As the overall amount of dust that is entrained from the ground plane is very much dependent on the interaction of the rotor wake with the ground, the more frequently this breakdown of the vortical structures occurs, the more dust is entrained.

6.4 Influence of Rotor Design and Disc Loading

It has been shown, in § 5.5.3, that the formation and development of the dust cloud in the flow field around a helicopter is dependent on the velocity field that is generated by the rotor. The mean downwash velocities generated by the rotor are determined primarily by the disc loading while the more detailed characteristics of the flow field are influenced by the design of the rotor. In the following section, results will be presented which demonstrate the extent to which the disc loading of the rotor effects the size and severity of the dust clouds that are produced when the rotor is simulated at the same three advance ratios as analysed in § 6.3. Further results are then presented which show how various rotor design parameters alter the size and density of the dust clouds that are produced. More specifically, the sensitivity of the shape and size of the dust cloud to the number of rotor blades, the blade twist and the root cutout of the blades is examined. These particular parameters and, additionally, the tip shape of the blades have the greatest effect on the strength of the tip vortices and are thus likely to have the greatest effect on the dust cloud that is generated. The three parameters that were investigated were selected as they would be the most straightforward to change on a real rotor. Finding the optimum design of the tip shape, although feasible, would be more

involved than simply changing the twist or root cutout of the blades and a large number of tip shapes and sizes would be need to be simulated to reveal any trend in the results. Investigating what effect the number of blades, twist and root cutout have on the strength of the tip vortices and how this, in turn, effects the size and density of the dust cloud that forms, provides valuable information on the formation of dust clouds around helicopters. If the effect of changing the tip shape on the strength of the tip vortices that are generated is known, then the effect of the tip shape on the size and density of the dust cloud generated by the rotor could then be inferred from the results presented in this section. The effect that the number of blades, the twist of the blades and the root cutout have on the flow field are thus examined and the results that are presented augment the discussion of the effect of the height of the rotor above the ground presented in Chapter 5.

6.4.1 Disc Loading

The mean downwash from a helicopter rotor is governed in the main by the disc loading of the rotor. The differences in the size and density of the dust cloud that forms around the rotor as a result of changing the disc loading are discussed in this section. The same baseline rotor as described in § 6.2 was used for this investigation. By altering the collective pitch of the blades, the rotor system was trimmed to different values of thrust coefficient to represent different disc loadings. The values of thrust coefficients simulated at each of the three thrust normalised advance ratios ranged from $C_T = 0.008$ to 0.013 which are equivalent to the empty weight and maximum takeoff weight of the EH-101. The advance ratio is normalised with the hover inflow velocity and comparison of the systems at the same normalised advance ratio ensures that the gross characteristics of the flow e.g. the skew angle of the wake, are maintained while the disc loading of the rotor is changed. Differences in the more detailed characteristics of the wake, for instance the size of the ground vortex that forms, are still apparent and it is these differences that will be shown to be responsible for the slight changes to the size and density of the dust cloud that is generated.

Figures 6.11 to 6.13 show the distributions of dust density and vorticity in the flow field surrounding the rotor at the three different normalised advance ratios of $\mu^\star = 0.6, 0.3$ and 0.0. At each advance ratio, five different simulations were conducted with the rotor in each simulation being trimmed to a different thrust coefficient. The images present the average distributions on a vertical slice through the longitudinal centreline of the rotor. The data was averaged over approximately 60 rotor revolutions once the initial transients of the system had dissipated. The effect of increasing the thrust coefficient on the dust density and vorticity distributions at the highest advance ratio is shown in Figure 6.11. As the thrust coefficient, and therefore disc loading, is increased, the extent of the high density region of dust which forms below the rotor also increases. Examination of the vorticity distribution shows that, at the lowest thrusts of $C_T = 0.008$ and 0.009, a very weak vortex forms on the ground plane at the front of the rotor wake. The weakness of the velocity field that is induced by this ground vortex in comparison to the effect of the oncoming flow results in only a small dust cloud forming below the rotor. This small region of dust remains in close proximity to the ground plane.

As the thrust coefficient is increased, the extent of the dust cloud, both along the ground plane and vertically upwards towards the rotor, also increases as shown in Figure 6.11 (c), (d) and (e). At higher thrust, the ground vortex that forms just upstream of the point at which the wake impinges on the ground plane becomes larger and stronger. As the strength and size of the ground vortex increases, a greater amount of dust accumulates in the separation zone that is located at approximately -1R upstream of the rotor axis. The dust is then entrained into the flow field by the velocity field and forms a wall-like structure below the leading edge of the rotor disc.

Figure 6.12 shows the dust density and vorticity distributions in the flow field around the rotor when it is operating at a thrust normalised advance ratio of $\mu^\star = 0.3$. Again, the gross characteristics of the averaged distributions are similar over the range of thrusts but on closer inspection subtle differences between the distributions are revealed. At this

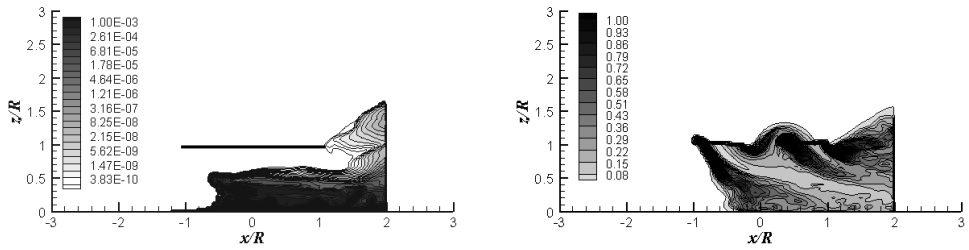

(a) $C_T = 0.008$

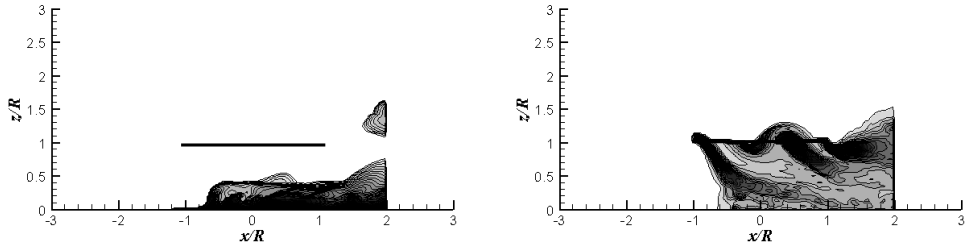

(b) $C_T = 0.009$

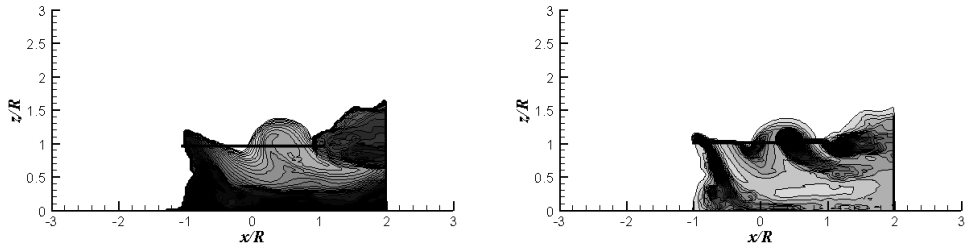

(c) $C_T = 0.010$

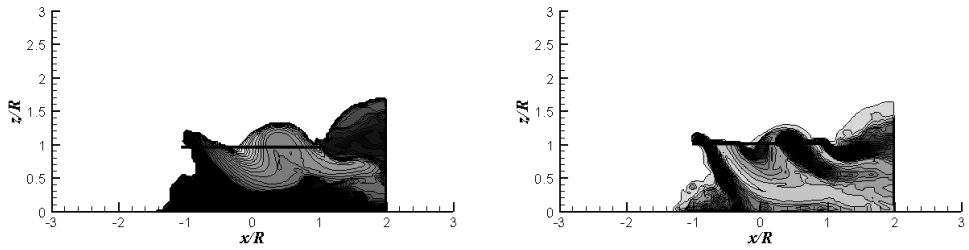

(d) $C_T = 0.012$

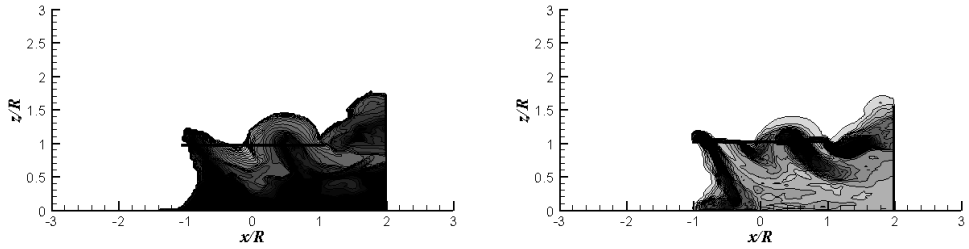

(e) $C_T = 0.013$

Figure 6.11: *Dust density and vorticity distributions generated by baseline rotor at $\mu^\star = 0.6$ at various thrust coefficients. Dust density shown on the left, vorticity shown on the right. Scales constant throughout remainder of chapter.*

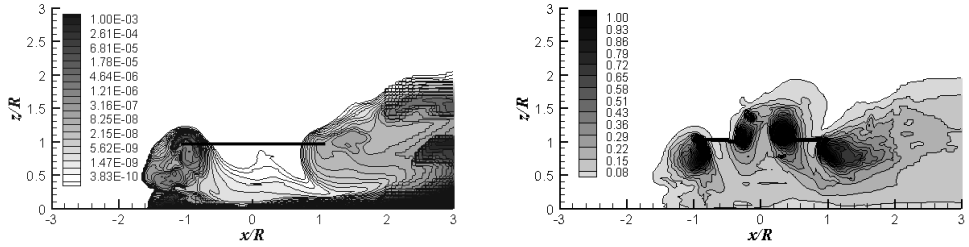

(a) $C_T = 0.008$

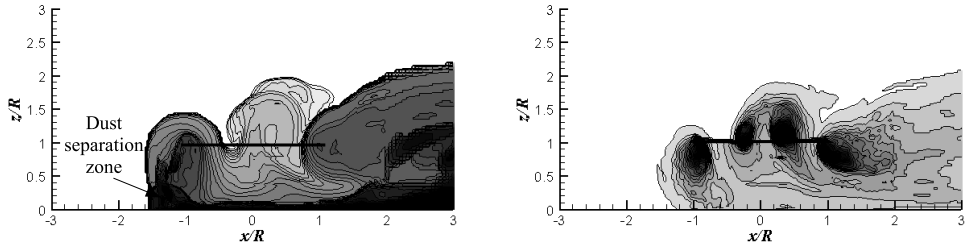

(b) $C_T = 0.009$

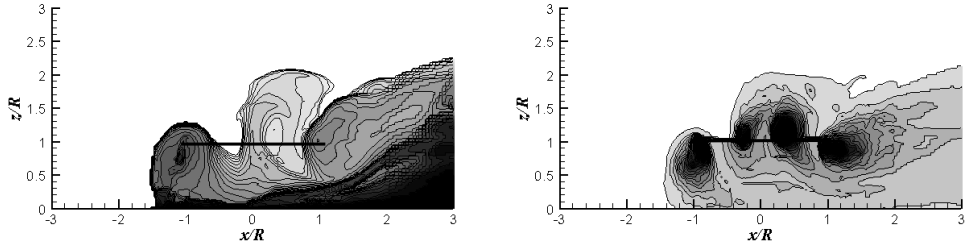

(c) $C_T = 0.010$

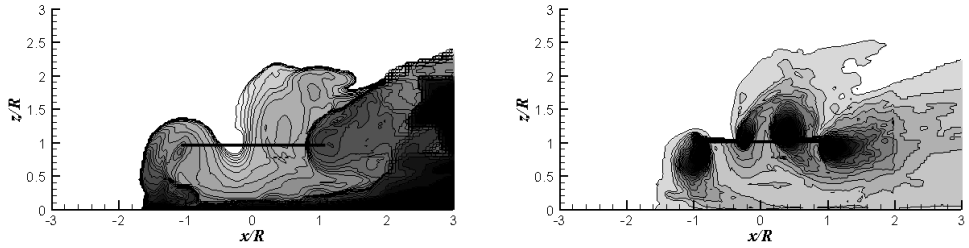

(d) $C_T = 0.012$

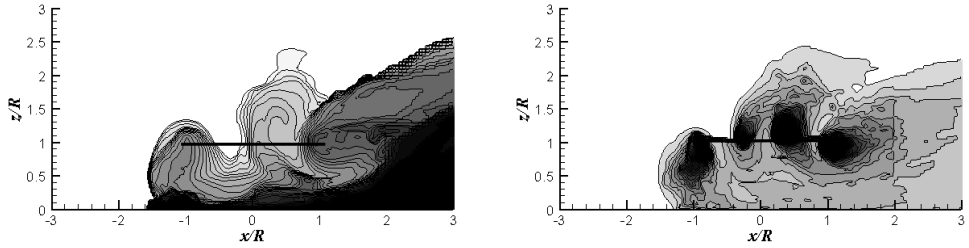

(e) $C_T = 0.013$

Figure 6.12: *Dust density and vorticity distributions generated by baseline rotor at $\mu^\star = 0.3$ at various thrust coefficients. Dust density shown on the left, vorticity shown on the right. Scales constant throughout remainder of chapter.*

advance ratio, the rotor wake recirculates intermittently through the front of the rotor disc. This recirculating flow entrains dust from the separation zone, which is evident in the dust distribution generated at each thrust coefficient at approximately -1.2R upstream of the rotor axis (highlighted in Figure 6.12 (b)), and transports it up into the flow around the front of the rotor. The dust then continues to recirculate in this region or is eventually transported downstream of the rotor. Examination of the development of the dust density distributions with changing thrust coefficient reveals that, at this advance ratio, as the thrust increases there is a very slight decrease in the density of dust that recirculates around the front of the rotor. This change may be due in part to the increase in downwash associated with increasing the disc loading. The dust that becomes entrained within the flow field may be transported downstream of the rotor more quickly when the downwash velocities are greater.

When in hover (Figure 6.13) the vortical structure generated by the rotor produces a highly recirculatory flow at all the thrust coefficients that were simulated. In hover, a wall-like structure of dust forms at around $x/R = \pm 2$. As the thrust coefficient is increased the wall-like structure becomes more prominent. This region of high density dust, which occurs at the separation zone, forms as the dust is entrained and transported away from the ground by the recirculating wake. This wall of dust is seen to some degree in all the simulations of this rotor in hover. The most obvious difference that occurs with a change in thrust, however, appears to be that, as the thrust increases, the size of the plume of dust above the centre of the rotor also increases. The extent of this plume correlates well with the corresponding plots of vorticity distribution. Closer inspection of the dust distributions, particularly in the region that circulates around the edge of the rotor disc, reveals there to be a distinct lateral asymmetry in the density of the cloud. This difference is particularly noticeable when $C_T = 0.012$. Examination of the development of the dust cloud reveals that the plume of dust above the centre of the rotor appears to affect the density of the dust cloud that develops around the rotor. Figure 6.14 shows a snapshot of the dust density distribution within the flow field surrounding the rotor when trimmed to $C_T = 0.012$. The arrows indicate the

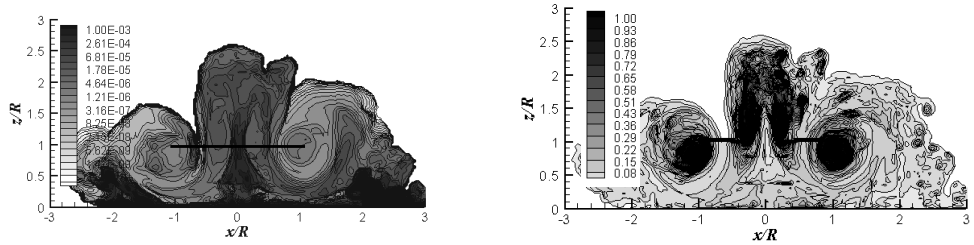

(a) $C_T = 0.008$

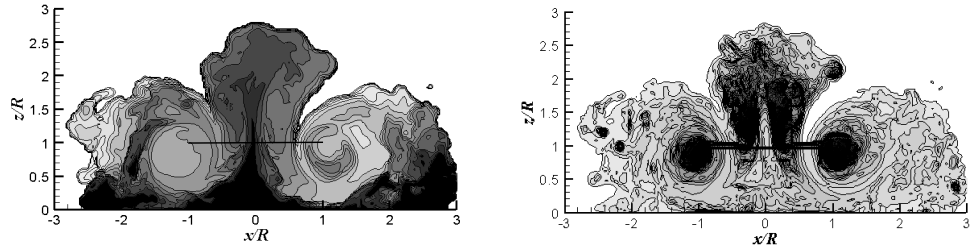

(b) $C_T = 0.009$

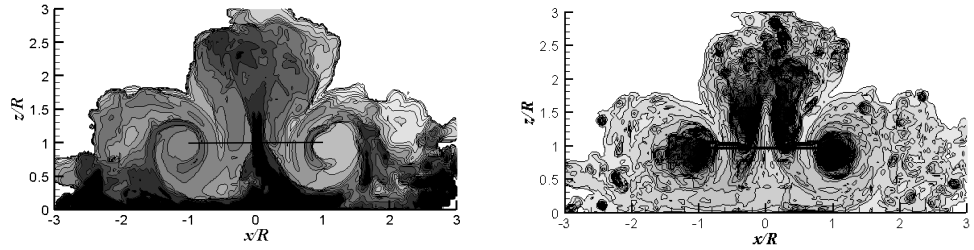

(c) $C_T = 0.010$

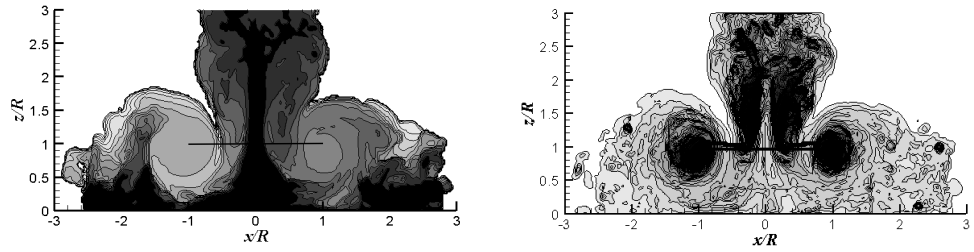

(d) $C_T = 0.012$

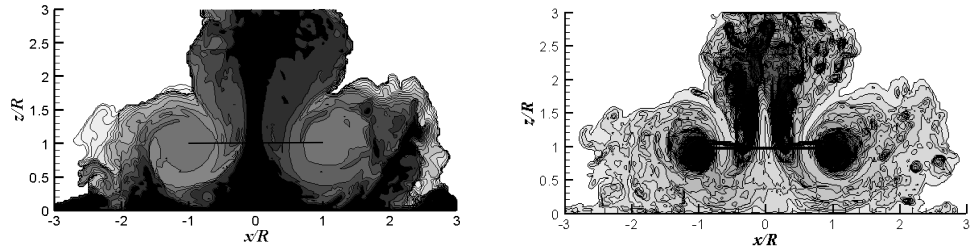

(e) $C_T = 0.013$

Figure 6.13: *Dust density and vorticity distributions generated by baseline rotor hovering at various thrust coefficients. Dust density shown on the left, vorticity shown on the right. Scales constant throughout remainder of chapter.*

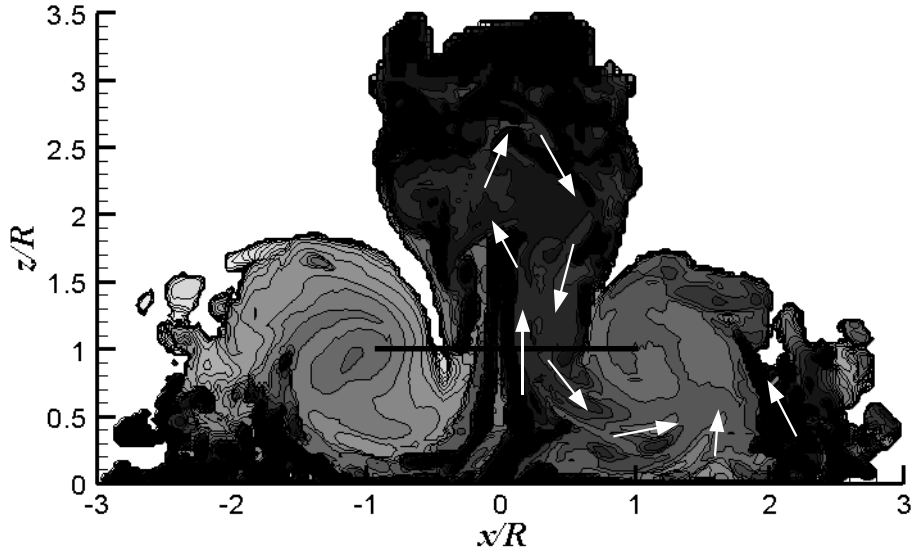

Figure 6.14: *Movement of dust contained within the plume above a rotor while hovering at a height of $1R$ above the ground.*

direction of movement of the dust through the flow field surrounding the rotor. As the cloud develops, a large amount of dust is transported up through the centre of the rotor into the plume above the rotor disc. The dust that is in the plume travels back down through the disc, in this case to the right of the figure, and contributes to the recirculation of dust around the right of the rotor disc. The vorticity in the plume is also transported back down towards the ground plane. This transport of vorticity increases the induced velocity close to the ground plane and this increase in velocity results in an increase in the entrainment of dust from the ground which adds further to the asymmetry of the dust cloud. The extent of the plume that forms may not be entirely realistic due to the lack of a fuselage in the present simulations, however. The asymmetry revealed in the results does suggest however that the density of the dust cloud that forms may be sensitive to the trim of the rotor disc and to small disturbances in the wake which might influence the movement of the dust within the plume. It also shows that the timescales associated with the formation of the dust cloud are very much longer than those associated with the flow around the rotor.

6.4.2 Rotor Design

When considering the strength of a rotor wake, vortex theory [68] shows that the total circulation, or, equivalently, vorticity, that is released from the rotor will be the same for a given thrust and disc area no matter what the design of the rotor. The distribution of the vorticity as it impinges on the ground plane can be altered, however, by changing the design of the rotor. As shown previously in § 6.3, the entrainment of dust from the ground plane into the airflow surrounding the rotor is initiated when the rotor wake approaches the ground and disturbs the dust. The interaction of the tip vortices with the ground plane plays a key role in the initial entrainment of dust. The design of the baseline rotor has been modified to investigate how altering the distribution of vorticity as it interacts with the ground plane affects the size and density of the dust cloud which develops. In all the cases that were simulated, the overall solidity of the rotor was maintained constant by adjusting the chord of the blades appropriately. This ensured that the overall strength of the wake produced by each different rotor configuration was kept constant. Three different rotor design parameters were modified, namely the number of blades, the blade twist and the root cutout of the blades. The results from this investigation of the effect of varying these rotor design parameters on the severity of the dust cloud are presented in the following sections.

6.4.2.1 Number of Blades

To investigate the effect that altering the number of rotor blades has on the dust cloud that develops, the number of blades on the baseline rotor was changed. Four different rotors were simulated; with 3, 4, 5 and 7 blades. Vortex theory [68] shows that the strength of the tip vortex trailed from each rotor blade when in hover,

$$\Gamma_v \propto \frac{2T}{\rho N_b (R - R_c) \Omega R} \tag{6.1}$$

where N_b is the number of blades and R_c is the root cutout of the blades. If the same total circulation is generated by the rotor, then distributing the circulation between an increasing number of blades results in the strength of each individual tip vortex being reduced while the gradient of the blade loading along each blade remains constant. Again, results are presented for the rotor operating at the three different advance ratios of $\mu^\star = 0.6, 0.3$ and 0.0 with the data in the plots having being averaged over approximately 60 rotor revolutions.

Figures 6.15 to 6.17 compare the dust density distributions which are generated by the rotors with different numbers of blades. At the highest advance ratio, $\mu^\star = 0.6$, that was simulated, changing the number of blades on the rotor appears to have only a small effect on the characteristics of the dust cloud that is generated, as shown in Figure 6.15. When the advance ratio is decreased to $\mu^\star = 0.3$ (Figure 6.16) the effect of changing the number of blades becomes more apparent. At this forward speed all four rotor configurations generate dust clouds that, in terms of geometry and size, are very similar but, as the number of blades is increased, the density of dust within the cloud reduces. In § 4.2.3 it was shown, by Eq. 4.24, that a non-linear relationship exists between the velocity that is induced along the ground plane and the resulting amount of dust that saltates across the ground and subsequently is entrained into the flow. When the number of blades is increased there is a reduction in strength of the tip vortices. This is shown by the vorticity distributions in Figure 6.18 where the strong region of vorticity below the leading edge of the rotor gradually moves away from the ground plane as the strength of the individual vortices decreases with increasing number of blades. This decrease in vortex strength also corresponds to a decrease in the induced velocity which, coupled with the non-linear relationship between velocity and dust, reduces the amount of dust that becomes entrained into the flow field surrounding the rotor.

The effect that the distribution of circulation has on the extent of the dust cloud produced by the rotor in hover can be seen in Figure 6.17. As was shown for $\mu^* = 0.3$, the general trend of the distribution, particularly within the region around the tips of the rotor blades, is for the dust density to decrease with increasing number of blades. With the strength of

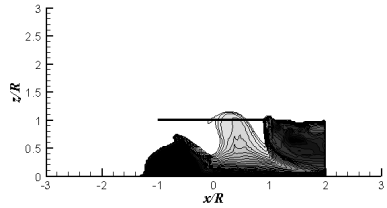

(a) *3 blades*

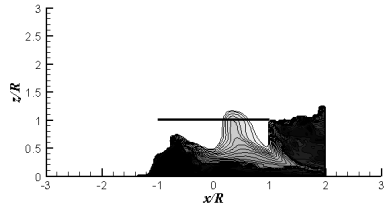

(b) *4 blades*

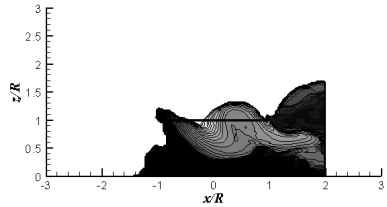

(c) *5 blades*

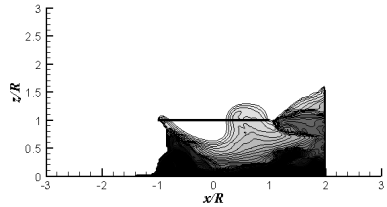

(d) *7 blades*

Figure 6.15: *Dust density distribution generated by baseline rotor with different numbers of blades at* $\mu^\star = 0.6$.

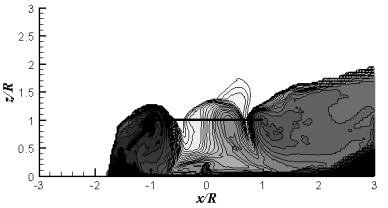

(a) *3 blades*

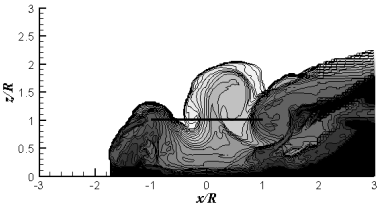

(b) *4 blades*

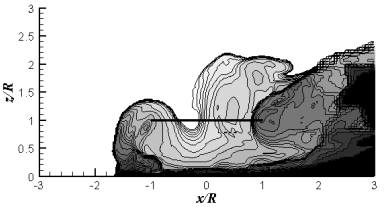

(c) *5 blades*

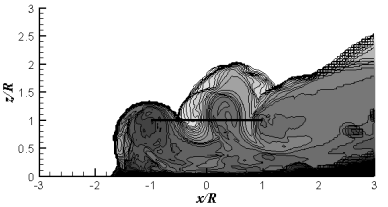

(d) *7 blades*

Figure 6.16: *Dust density distribution generated by baseline rotor with different numbers of blades at* $\mu^\star = 0.3$.

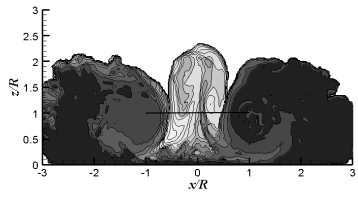

(a) *3 blades*

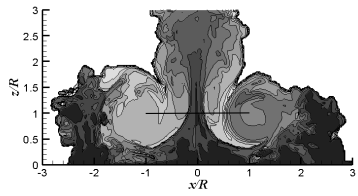

(b) *4 blades*

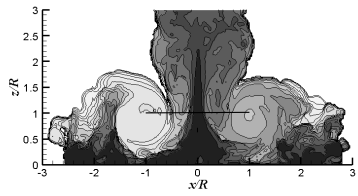

(c) *5 blades*

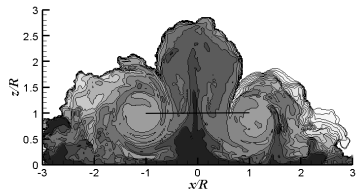

(d) *7 blades*

Figure 6.17: *Dust density distribution generated by baseline rotor with different numbers of blades in hover.*

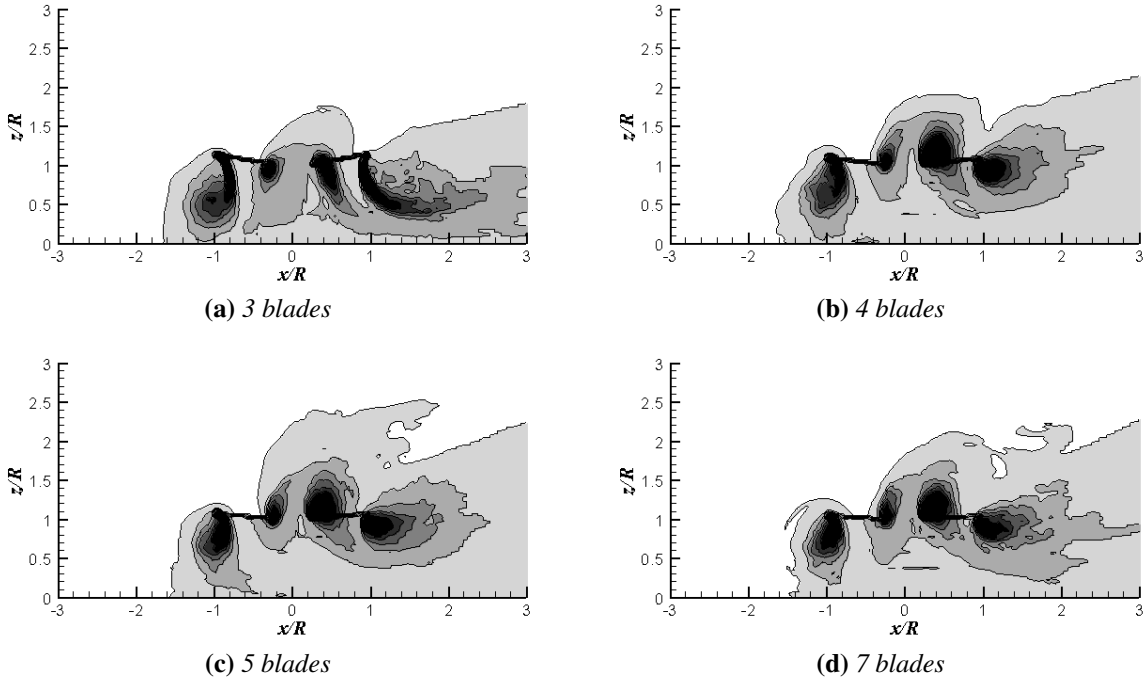

(a) *3 blades* **(b)** *4 blades*

(c) *5 blades* **(d)** *7 blades*

Figure 6.18: *Vorticity distribution generated by baseline rotor with different numbers of blades at* $\mu^\star = 0.3$.

the tip vortices being inversely proportional to the number of blades, the three-bladed rotor produces the strongest vortices and the figures show this rotor to generate the densest dust cloud. A similar wall of dust to that mentioned in § 6.4.1 forms at approximately $\pm 2R$ away from the centre of the rotor. The behaviour of this region of high density dust as the number of blades is increased is most interesting. The dust cloud generated by the three-bladed rotor is of high density throughout, thus the wall of dust is not particularly obvious. With the four-bladed rotor, the density of dust that recirculates through the rotor disc decreases, thus revealing the region of high density dust that composes the wall structure. As the number of blades is increased further, there is minimal further reduction in the density of dust within the recirculating region. There is, however, a reduction in the density of the dust which forms the wall. Thus, extrapolating this to a real life situation, a helicopter with more blades may have better brownout characteristics than others with fewer blades as the wall of dust is more diffuse and the pilot may well be able to see further.

6.4.2.2 Twist

To investigate further the effect that various rotor design parameters have on the size and density of the dust clouds generated by the rotor, the original baseline rotor configuration was modified to have different amounts of blade twist. The rotor was modelled to have blades with $8°, 11°, 13°$ and $16°$ of linear twist. Each rotor was simulated at the same three advance ratios used for the previous simulations presented in this chapter. The dust distributions that were generated at each advance ratio are shown in Figures 6.19 to 6.21.

Figure 6.19 shows the dust distributions that are predicted by the VTM to form around the rotors with different blade twist whilst simulated at $\mu^\star = 0.6$. As the twist of the blades is increased, the extent of the high density region of dust that forms below the leading edge of the rotor reduces. When the blades have a twist of $16°$, the dust cloud that is produced would cause the least obscuration of the pilot's visibility as the cloud is very small and remains in close proximity to the ground plane. The sensitivity of the dust distribution to blade twist can be explained by examining the averaged blade loading distributions across the rotor disc and the corresponding vorticity distributions within the flow field for the range of twist values that were simulated. As the twist of the blades is increased, the loading along the blades becomes more uniform and thus the loading in the tip region reduces. This change in the distribution of the loading along the blades, when the rotor is simulated at $\mu^\star = 0.6$, can be seen in Figure 6.22. For each of the four values of twist, the blade loading distribution around the rotor disc, averaged over 50 rotor revolutions, is shown. As the twist is increased the loading in the tip region, around the front of the rotor disc, decreases. The corresponding distribution of the circulation gradient ($d\Gamma/dr$), which is directly related to the strength of the tip vortices, is shown in Figure 6.23. The circulation gradient close to the tip of the blades reduces as the twist is increased, thus reducing the strength of the tip vortices. The effect of the reduction in strength of the tip vortices on the wake produced by the rotor at $\mu^\star = 0.6$ is visible in the plots shown on the left of Figure 6.24. As the twist increases and the strength of the tip vortices decreases the extent of the ground vortex which forms below the front of

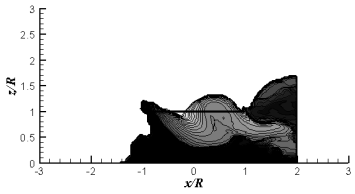

(a) $-8°$ *blade twist*

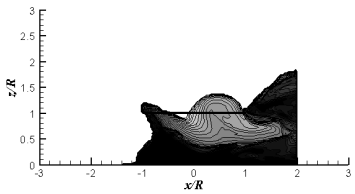

(b) $-11°$ *blade twist*

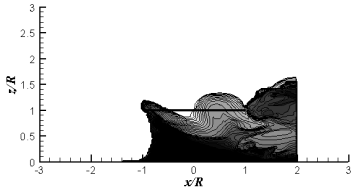

(c) $-13°$ *blade twist*

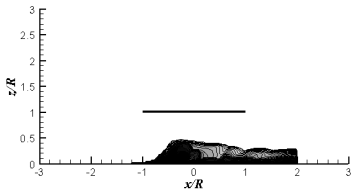

(d) $-16°$ *blade twist*

Figure 6.19: *Dust density distribution generated by baseline rotor with varying degrees of blade twist at* $\mu^\star = 0.6$.

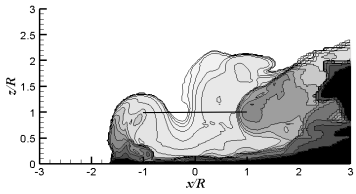

(a) $-8°$ *blade twist*

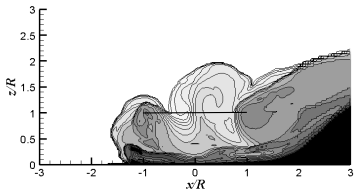

(b) $-11°$ *blade twist*

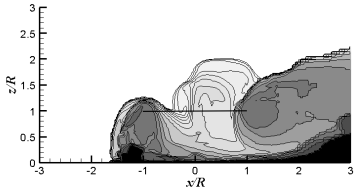

(c) $-13°$ *blade twist*

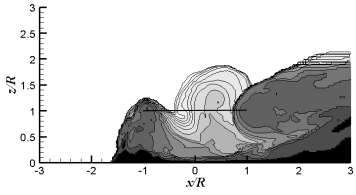

(d) $-16°$ *blade twist*

Figure 6.20: *Dust density distribution generated by baseline rotor with varying degrees of blade twist at* $\mu^\star = 0.3$.

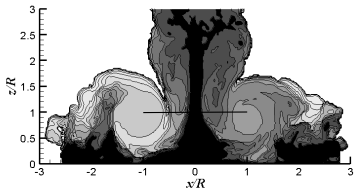

(a) $-8°$ *blade twist*

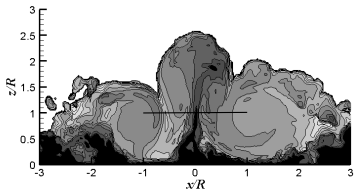

(b) $-11°$ *blade twist*

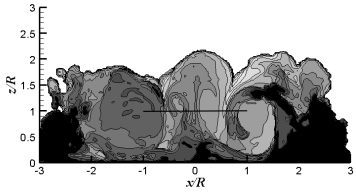

(c) $-13°$ *blade twist*

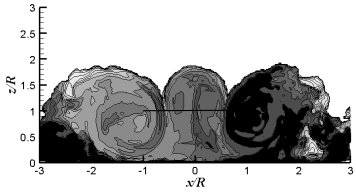

(d) $-16°$ *blade twist*

Figure 6.21: *Dust density distribution generated by baseline rotor with varying degrees of blade twist in hover.*

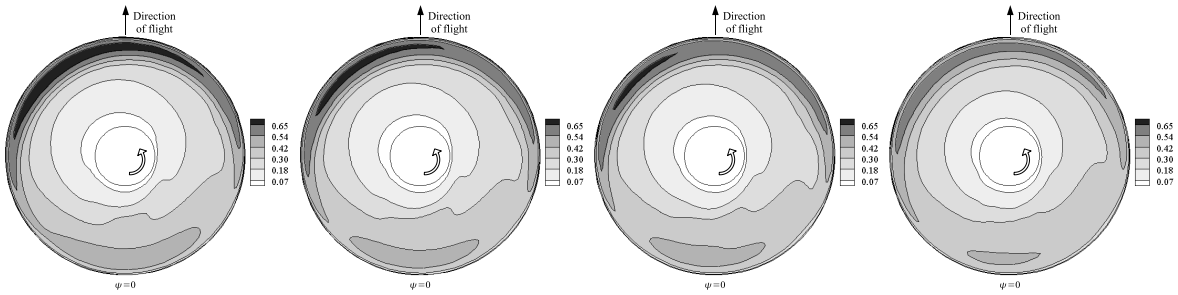

(a) -8° *blade twist* **(b)** -11° *blade twist* **(c)** -13° *blade twist* **(d)** -16° *blade twist*

Figure 6.22: *Blade loading distribution around rotor disc at* $\mu^\star = 0.6$*. Data averaged over 50 rotor revolutions.*

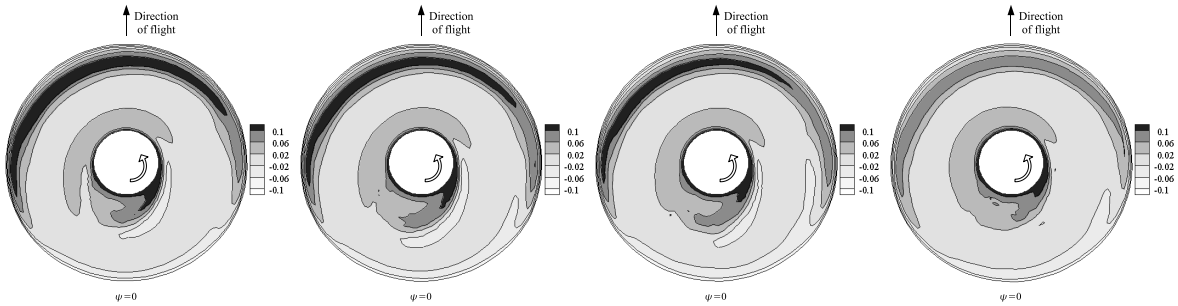

(a) -8° *blade twist* **(b)** -11° *blade twist* **(c)** -13° *blade twist* **(d)** -16° *blade twist*

Figure 6.23: *Distribution of the circulation gradient around rotor disc at* $\mu^\star = 0.6$*.*

the rotor, at this advance ratio, reduces. This reduction in the extent and strength of the wake in this area results in the size of the dust cloud produced also reducing as the twist increases.

When the advance ratio is reduced to $\mu^\star = 0.3$ there is similar reduction in strength of the tip vortices as the twist of the blades is increased. Figure 6.20 shows however, that instead of the dust cloud decreasing in size and density as the tip vortex strength decreases, as was the case when the rotor was simulated at $\mu^\star = 0.6$, the opposite is true and that the density of the dust cloud increases with increasing twist. Examination of the vorticity distribution at this lower advance ratio (shown on the right of Figure 6.24) reveals that, as the strength of the tip vortices reduces with increasing twist, and the distribution of the loading along the blades is altered, there is a more subtle change in the behaviour of the wake than occurs when the number of blades are altered (Figure 6.18). It would appear that as the strength of the tip vortices increases there is a greater tendency for these vortices to circulate round

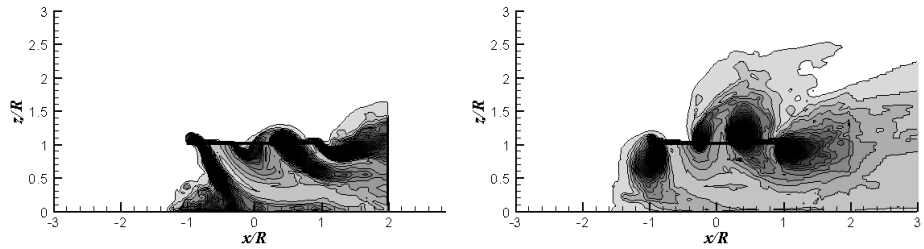

(a) $-8°$ *blade twist*

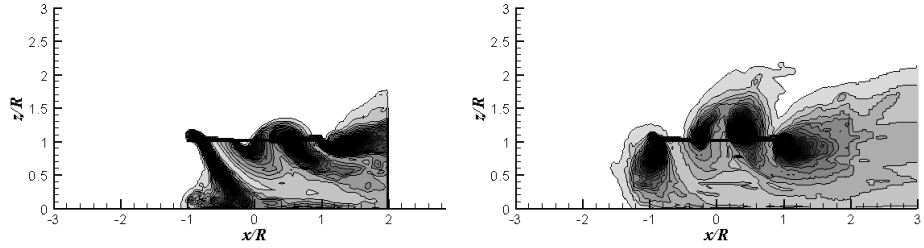

(b) $-11°$ *blade twist*

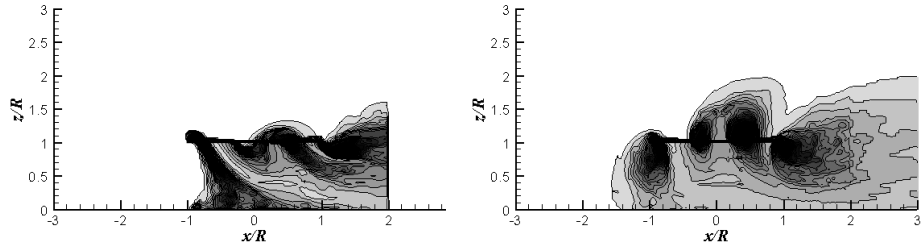

(c) $-13°$ *blade twist*

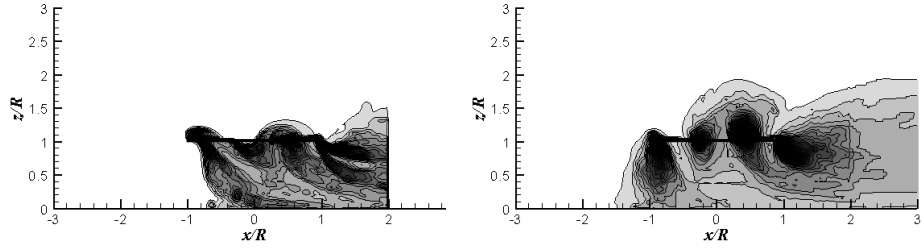

(d) $-16°$ *blade twist*

Figure 6.24: *Average vorticity distribution generated by baseline rotor with varying degrees of blade twist at* $\mu^\star = 0.6$ *(left hand column) and* $\mu^\star = 0.3$ *(right hand column).*

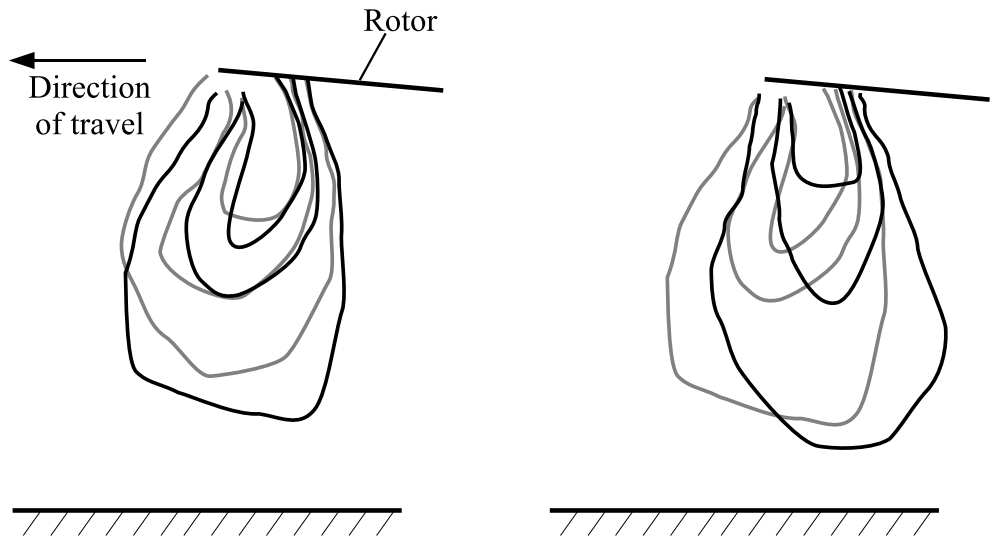

(a) $-8°$ *and* $-11°$ *blade twist* **(b)** $-11°$ *and* $-16°$ *blade twist*

Figure 6.25: *Schematic showing contours of the averaged vorticity distributions around the front of the rotor at* $\mu^\star = 0.3$ *as the twist of the blades is changed. In each subfigure the darker lines represent the vorticity from the rotor with the greater amount of twist.*

the front of the rotor disc. With the decrease in vortex strength associated with an increase in blade twist, the tip vortices travel down towards the ground more often than the vortices with greater strength. This change in the main direction of travel of the tip vortices is shown schematically in Figure 6.25. In each subfigure three contours of vorticity are shown for two different values of twist. With the dark contours representing the rotor with the larger twist, the figure shows that, when the twist is increased, the centroid of the vorticity moves towards the rear of the rotor and down towards the ground plane. As these contours show the vorticity distribution in the flow field averaged over a number of rotor revolutions, this slight change in the behaviour of the wake suggests that there is a greater tendency for the wake to travel towards the ground plane when the blades are more highly twisted. The more frequent the interaction of the wake with the ground plane, the more the dust is disturbed and released into the flow field – thus producing the dust distributions shown in Figure 6.20.

When the rotor is hovering above the ground, as shown in Figure 6.21, the most obvious change in the dust distribution is the height to which the plume of dust through the centre of

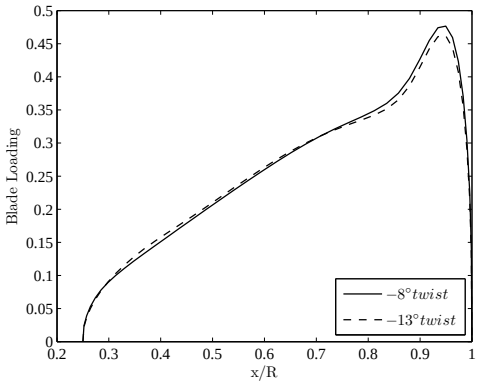

Figure 6.26: *Blade loading distribution along the length of the rotor blade when the rotor is in hover. Distribution has been averaged over 30 rotor revolutions and around the azimuth.*

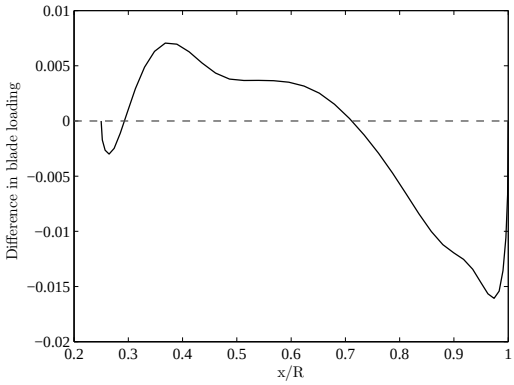

Figure 6.27: *Difference in blade loading distribution generated by the rotors with $-8°$ and $-13°$ of blade twist while in hover. Distribution is calculated by subtracting the distribution generated with $-8°$ blade twist from the distribution generated with $-13°$ blade twist.*

the rotor reaches. As the twist of the blades increases, the height of the plume decreases. The density of the dust within this plume is also seen to reduce. This change in wake geometry and dust density is most likely related to the increase in induced downwash close to the centre of the rotor when the twist of the blades is increased. Figure 6.26 shows the blade loading distribution along the length of the blade for the rotors with $-8°$ and $-13°$ of blade twist. The data shown was averaged over 30 revolutions and around the azimuth. The differences between these two distributions are small but are made more apparent in Figure 6.27 where the distribution along the blades with $-8°$ of twist has been subtracted from the distribution along the blades with $-13°$. Over the inboard portion of the blade (apart from a very small region at the root of the blade), up to approximately $x/R = 0.7$, the rotor with $-13°$ of twist has the greater blade loading while in the tip region the rotor with $-8°$ of twist has the greater blade loading. Thus, at the higher twist, the loading on the blades, close to the centre of the rotor, is greater than that on the rotor with lower twist. The change in the downwash distribution in the flow field surrounding the rotor, that is associated with an increase in the twist of the blades, is shown in Figure 6.28. By increasing the twist of the blades from $-8°$

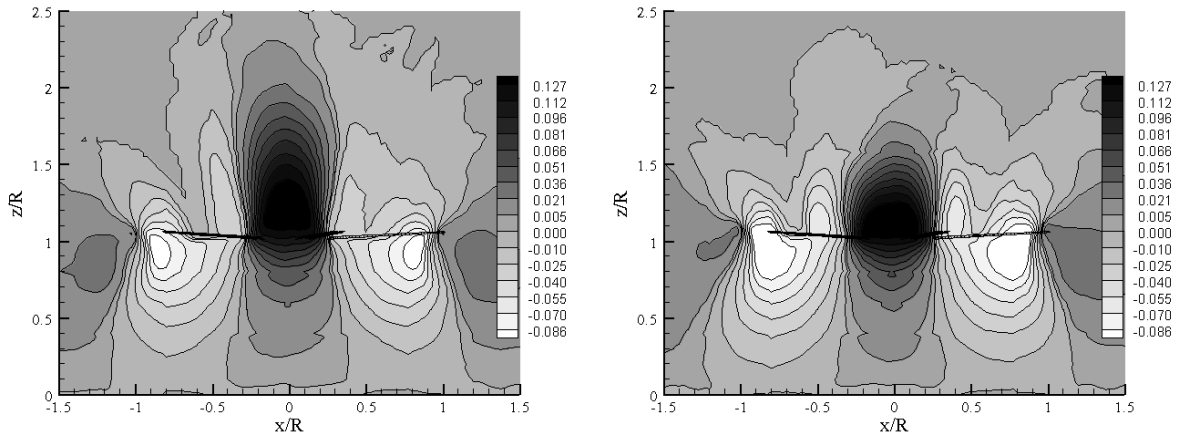

(a) -8° *twist* **(b)** -13° *twist*

Figure 6.28: *Downwash distribution on a vertical slice through the centreline of the rotor for two rotors with different amounts of blade twist. Negative values imply downwards velocity.*

to -13°, there is an increase in the downwards component of velocity below the rotor disc. This increase in downwash, at the higher twist, reduces the velocity of the upflow through the centre of the rotor. This reduction in upflow, in turn, reduces the amount of dust that escapes vertically upwards through the centre of the rotor resulting in the reduction in plume height shown in Figure 6.21.

6.4.2.3 Root Cutout

The final rotor parameter to be modified was the root cutout of the blades. The baseline rotor was altered to have root cutouts of 15, 20 and 25% of the blade radius. As with modifying the number of blades (§ 6.4.2.1), when modifying the root cutout of the blades, the overall solidity of the rotor was kept constant by changing the blade chord. Vortex theory [68] can be used to estimate the strength of the tip vortices that are trailed from the blades, as described in § 6.4.2.1. Equation 6.1 shows that increasing the root cutout of the blades increases the strength of the tip vortices that are generated. This change in vortex strength can be inferred from Figure 6.29 where the distribution of circulation gradient around the rotor discs at $\mu^\star = 0.6$ are shown. The radial circulation gradient in the tip region at the front of the disc

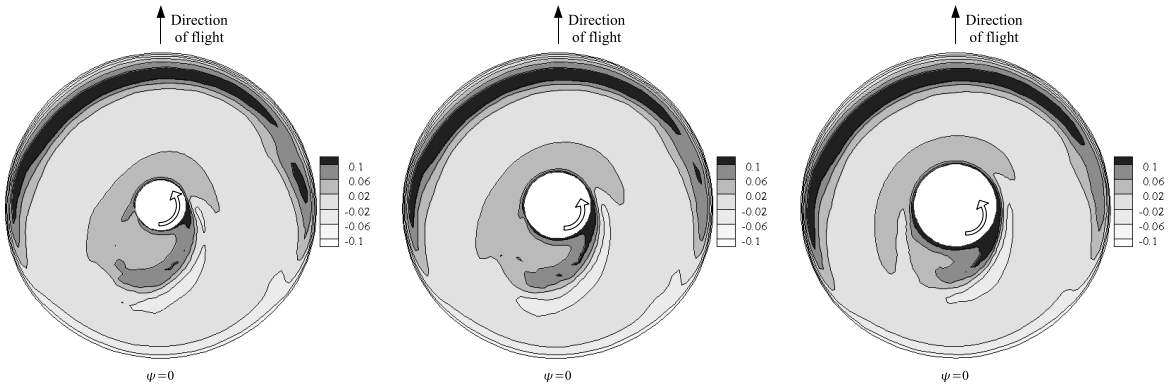

(a) 15% *root cutout* **(b)** 20% *root cutout* **(c)** 25% *root cutout*

Figure 6.29: *Distribution of the circulation gradient around the rotor disc at* $\mu^\star = 0.6$.

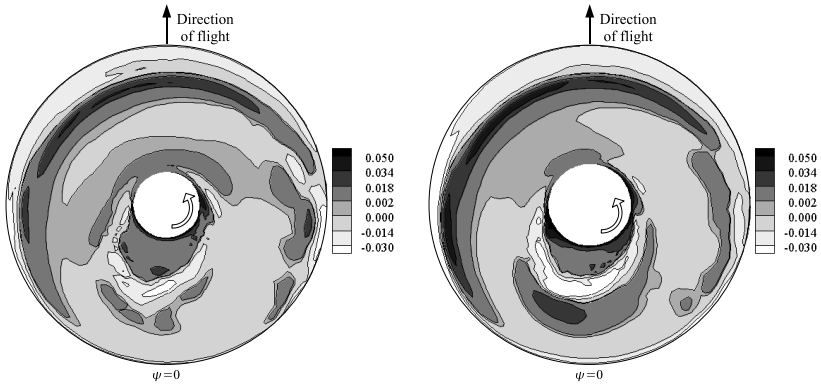

(a) $20\% - 15\%$ *root cutout* **(b)** $25\% - 20\%$ *root cutout*

Figure 6.30: *Difference in the distribution of the circulation gradient around the rotor disc generated with different root cutouts. Rotors simulated at* $\mu^\star = 0.6$.

is seen to increase with increasing root cutout. This is shown more clearly in Figure 6.30 where the distribution generated with a smaller root cutout is subtracted from that generated with a larger cutout. In this figure, the darker contours represent the areas of the disc where the circulation gradient is greater on the rotor with the larger cutout. Increasing the tip vortex strength by increasing root cutout has a similar effect on the dust distribution to that caused by decreasing blade twist, as discussed in § 6.4.2.2. The average dust distributions generated by the rotors with the three different root cutouts are shown in Figures 6.31 to 6.33.

When the rotors are simulated at $\mu^\star = 0.6$ (Figure 6.31), increasing the root cutout results in a slight increase in the size and density of the dust cloud below the front of the rotor. This

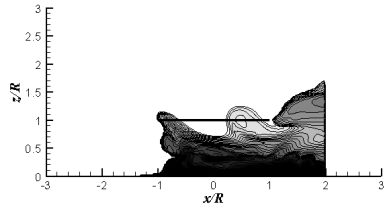

(a) 15% *root cutout*

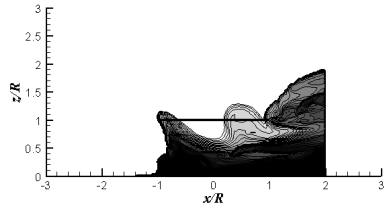

(b) 20% *root cutout*

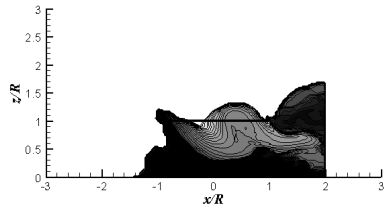

(c) 25% *root cutout*

Figure 6.31: *Dust density distribution generated by baseline rotor with varying blade root cutouts at* $\mu^{\star} = 0.6$.

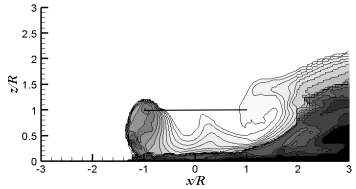

(a) 15% *root cutout*

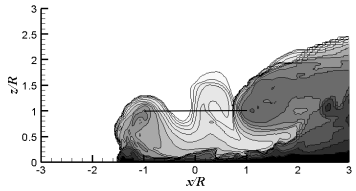

(b) 20% *root cutout*

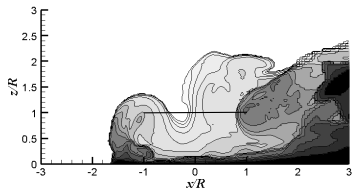

(c) 25% *root cutout*

Figure 6.32: *Dust density distribution generated by baseline rotor with varying blade root cutouts at* $\mu^{\star} = 0.3$.

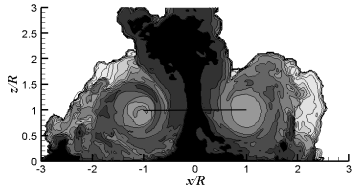

(a) 15% *root cutout*

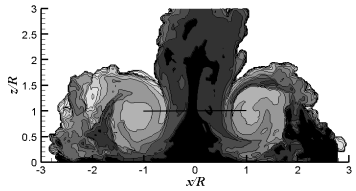

(b) 20% *root cutout*

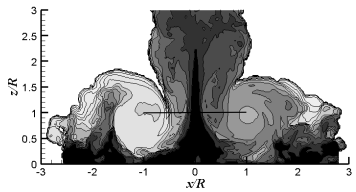

(c) 25% *root cutout*

Figure 6.33: *Dust density distribution generated by baseline rotor with varying blade root cutouts in hover.*

change in dust distribution shows the same trend as that observed when increasing the tip vortex strength by decreasing the blade twist. At the advance ratio of $\mu^{\star} = 0.3$ (Figure 6.32) there is a slight decrease in the density of dust within the cloud that forms around the front of the rotor. Again, this is in line with the observations made in § 6.4.2.2 that are due to subtle changes in the behaviour of the wake. When the rotor is in hover, Figure 6.33 shows that as the root cutout increases, there is a slight decrease in the density of the dust recirculating in the region around the blade tips. Figure 6.34 shows the Z-component of the velocity distribution generated by the rotor with varying amounts of root cutout when hovering above the ground. The figure shows only the upwards velocity. As the cutout decreases, the upwards velocity close to the ground plane, below the centre of the rotor,

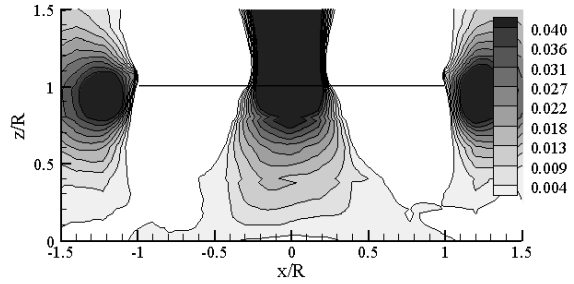

(a) 15% *root cutout*

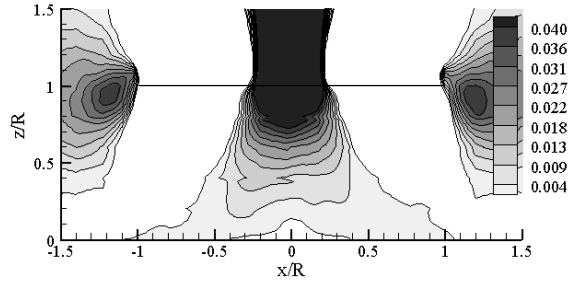

(b) 20% *root cutout*

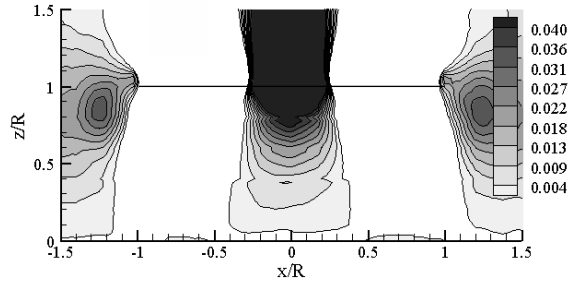

(c) 25% *root cutout*

Figure 6.34: *Distribution of upwards velocity generated by baseline rotor with varying blade root cutouts in hover. (Regions of downwards velocity blanked in order to reveal only the upwards distribution.)*

increases. This increase in upwards velocity increases the amount of dust that is entrained from the ground plane and that subsequently becomes contained within the plume. The density of dust in the plume has been shown previously, in § 6.4.1, to contribute to the dust recirculating around the rotor tips. Thus as the root cutout decreases the amount of dust transported from the plume to the recirculating regions increases.

6.5 Summary

A generic five-bladed rotor has been used as a baseline rotor and simulated using the VTM. The rotor was modelled at three different advance ratios and it has been shown that the main structure of the flow field and resulting dust cloud depends very much on the advance ratio of the rotor. As the forward speed of the rotor is reduced the wakes that are generated become less structured. The baseline rotor was then modified to investigate what effect the disc loading, the number of blades, the twist of the blades and the blade root cutout have on the size and density of the dust cloud which develops around the rotor. In was shown in Chapter 5 that the formation of the dust cloud is related to the induced velocities along the ground plane and to the behaviour of the rotor wake. The study of the baseline rotor in the current chapter has shown that altering the rotor parameters does influence the size and severity of the dust cloud that is produced and that the changes to the dust cloud are very much dependent on the strength of the tip vortices that are generated by the rotor. It was found that, for this particular baseline rotor, the behaviour of the wake and corresponding dust cloud, when the strength of the tip vortices was increased, was dependent on the advance ratio of the rotor. At the higher advance ratio, increasing the strength of the tip vortices resulted in the dust cloud becoming larger and more dense in all cases. At the lower advance ratio the same was true when the number of blades was changed, however the opposite was true when the twist and root cutout of the blades were altered. The more subtle changes in the flow field associated with changing these two parameters resulted in the dust density decreasing with increasing tip vortex strength. Although the findings presented may not be absolutely conclusive, as the wakes of different rotors may behave differently, they do suggest that the size and density of the dust clouds that are generated by rotors are sensitive to the rotor geometry. Thus, a fully aerodynamic solution to the problem of brownout may well be possible.

Chapter 7

Conclusions and Future Work

7.1 Conclusions

One of the main aims of this research has been to provide insight into the processes that govern the entrainment of dust from the ground into the flow field surrounding helicopters when they operate in desert conditions. The research has also focused on determining how the helicopter configuration and rotor design affect the size and geometry of the wake that is generated and how this in turn affects the size and density of the dust clouds that form. To conduct these investigations, a computational model called the VTM, that is based on the vorticity-velocity form of the Navier-Stokes equation, was used. It was also required that the VTM be modified to allow the transport of particles within the flow field to be simulated.

During hovering flight in ground effect, it appears that the overall structure of the wake that is generated by the rotor can vary significantly depending on the rotor configuration and the height of the rotor above the ground. Instability within the rotor wake can cause the rotor to generate one of two significantly different wake structures. In one of these structures the tip vortices move downwards and away from the rotor while in the other the vortices circulate around the rotor tips. This research suggests that the variation between the rotor performance of different helicopters, when operating in ground effect, may be due in part to

these differences in the structure of the wake that is generated by each rotor.

To allow the simulation of brownout a semi-empirical model has been integrated into the VTM to determine the amount of dust that is entrained from the ground plane into the flow field surrounding the rotor. The process of dust entrainment is governed by the induced velocities within the flow field and particularly by the velocities close to the ground. The simulations presented in this dissertation suggest there to be a universal model which describes the basic processes that govern the entrainment of dust. As the velocity along the ground plane increases beyond a threshold velocity, entrainment of dust from the ground into the flow field is initiated. The entrained dust stays in close proximity to the ground until the trajectory of the flow turns away from the ground and transports the dust up into the flow surrounding the helicopter. A separation zone exists where the dust accumulates as it is transported along close to the ground. The separation zone occurs close to a stagnation point in the flow where the radial velocity of the tip vortices is no longer great enough to penetrate the oncoming flow and the trajectory turns away from the ground plane. Due to the velocity field induced by each individual tip vortex, a very small separation zone is also formed just upstream of each vortex as it interacts with the ground. As the induced velocity is related to the vorticity within the wake, the size and density of the dust cloud that is produced is very much dependent on the behaviour of the rotor wake.

Data from military operations has suggested that tandem rotor helicopters are more susceptible to inducing brownout than single rotor helicopters. Simulations of these two helicopter configurations were conducted to determine whether the VTM predicts this to be the case. The results from the simulations have suggested that tandem rotor helicopters do in fact generate dust clouds that are larger and more dense than those generated by single rotor helicopters, when simulated at the same operating conditions, and hence these results suggest that tandem rotor helicopters are indeed more susceptible to inducing brownout. The overall wake structures generated by the single rotor and tandem rotor configurations, when operating at the same advance ratio, appear quite different. Gradually reducing the advance

ratio causes the wake from the single rotor to transition quite quickly from a form where there is a prominent ground vortex to that where the majority of the wake recirculates around the leading edge of the rotor. When the wake recirculates around the front of the rotor there is very little interaction of the wake with the ground plane. With the tandem configuration however, reducing the advance ratio results in the ground vortex from the rear rotor moving forward below the front rotor while the vorticity generated by the front rotor circulates around the leading edge of that rotor. This results in a much greater interaction of the wake with the ground plane than is experienced by the single rotor helicopter and thus a greater amount of dust is entrained into the flow field around the tandem rotor.

The entrainment of dust from the ground plane below a helicopter is very much dependent on the induced velocities within the flow. Thus, it may be expected that the stronger the tip vortices that are generated by the rotor the more dust that becomes entrained within the flow. This research has shown this to be not necessarily the case. It has been shown that the behaviour of the rotor wake, and hence the dust cloud, is dependent on the advance ratio of the rotor and that increasing the strength of the tip vortices does not necessarily mean a greater interaction of the wake with the ground plane. For the particular rotor that was simulated, at faster advance ratios, increasing the strength of the tip vortices, by changing the design of the rotor, does increase the size and density of the dust cloud as the strength of the wake along the ground plane increases. At slower advance ratios however, the method of changing the strength of the tip vortices appears to have an effect on the wake structure that forms. Decreasing the number of blades increases the strength of the wake on the ground and results in an increase in the density of the dust cloud. Changing the twist and root cutout of the blades however results in more subtle changes to the structure of the wake. Increasing the strength of the tip vortices by altering either of these two parameters causes the density of dust within the cloud to in fact decrease.

Although the physics that governs the entrainment of dust from the ground plane is consistent between rotors, the size and density of the cloud that forms is very much rotor depen-

dent. This research has focused on only a few select rotors but has shown how differences in wake structure can have a significant effect on the dust cloud that forms. Thus, to determine the size and density of the dust cloud that would form around any particular rotor, the behaviour of the wake of that rotor must first be known.

7.2 Future Work

The work presented in this dissertation can be extended considerably by conducting further work in the future. Much of this future work would involve improving the modelling of the ground plane and the dust entrainment models. However, there are also other areas that may require further investigation in the future that have been revealed by some of the results generated in the current research.

To conduct much of the research presented in this dissertation the VTM had to be modified to allow the transport of particles to be simulated. The particle entrainment models that were implemented were taken from work published in the field of sedimentology. One of the aims of the research was to show that these models capture the general behaviour of the dust clouds, as was presented in § 4.4, and to determine the physics that governs the entrainment process, as presented in § 5.5.3. In the future, this work must be extended further if the spectrum of dust density within the flow field around any particular rotor is to be modelled accurately. A controlled experimental investigation must be conducted in which the particles are all of a known size. Such an experiment is required so that the spectrum of dust within the clouds as predicted using semi-empirical entrainment models can be verified. The specific properties of the particles that saltate along the ground plane and those that become suspended in the flow can be specified in the computational model. The ability of the entrainment models used during this research to predict the spectrum of dust contained within the cloud could then be verified by comparing the computed distribution to data gathered through experiment. A further development to this would then be to establish

how the density of dust as predicted by the VTM relates to what a pilot would actually see and to determine how dense the dust cloud must be before the helicopter is considered to be encountering brownout.

Further work must also be done to make the ground plane more realistic. Firstly, the condition of no-slip should be implemented and a study conducted to determine how this affects the size and density of the dust clouds that are generated. In addition to this, and particularly relevant when simulating hovering rotors, the amount of dust that is on the ground plane, and available for entrainment, should be limited. Not only would this be more representative of an actual desert, there would also be interest in investigating how long it takes a dust cloud to disperse and settle out of the flow field once there is no further entrainment of dust from the ground. Another worthwhile modification to the code would be to allow the rotor to approach the ground plane during a simulation. As it is currently, the rotor can be simulated in any trajectory but the height of the rotor above the ground plane remains constant. For the research presented in this dissertation, landing manoeuvres were approximated by simulating the rotor at various gradually slowing advance ratios but the rotor remained at a constant height. A more realistic landing manoeuvre could obviously be simulated if the rotor was capable of flying down towards the ground plane.

Research conducted for this dissertation revealed that the overall structure of the wake generated by different rotors can themselves appear very different when operating in ground effect. In § 5.4 these differences were highlighted by studying the wakes of hovering rotors. An instability in the wake causes the structure of the wake to change but it is still unclear why this instability effects the wake of some rotors and not others. Thus, in the future, an investigation into wake instability in ground effect may be conducted to try to understand which particular rotor and wake characteristics cause this instability to propagate through the wake and change its overall structure. A worthwhile experimental investigation, which would augmented this further computational work, would be to examine the wake structures generated by a variety of hovering rotors under laboratory conditions to determine whether

these different wake structures do in fact exist.

Finally, some of the current work, in particular that in § 3.3.2 in which the rotor of Lee *et al.* was simulated and that in Chapter 6 in which a generic five-bladed rotor was simulated, has suggested that the boundary plot of Curtiss *et al.* [20], which describes the different structures of a rotor wake during forward flight IGE, may not be entirely accurate for all rotors. There is also difficulty in determining when the rotor wake transitions from the recirculatory regime to the ground vortex regime. Thus, in the future, a study may be conducted in which a variety of different rotors are simulated in forward flight in ground effect. By examining the wake structures generated at a range of flight speeds and rotor heights above the ground it will be possible to gauge how applicable the original boundary plot is to other rotors and perhaps a new boundary plot could be defined.

Although there is much work to be done in the future and many questions still to answer, it is hoped that the results presented in this dissertation will be of use to helicopter designers and operators when trying to reduce the amount of dust that is entrained by the rotor wake in desert conditions in the hope of eventually eliminating brownout altogether.

Bibliography

[1] Rodgers, S.J., "Evaluation of The Dust Cloud Generated by Helicopter Rotor Downwash," USAAVLABS Technical Report 67-81, U.S. Army Aviation Material Laboratories, 1968.

[2] Cowherd, C., "Sandblaster 2 Support of See-Through Technologies for Particulate Brownout," MRI Project No. 110565.1.001, Midwest Research Institute, 2007.

[3] Nathan, N.D. and Green, R.B., "Flow Visualisation of the Helicopter Brown-out Phenomenon," *Aeronautical Journal*, Vol. 113 (1145), July 2009, pp. 467–478.

[4] Lee, T.E., Leishman, J.G., and Ramasamy, M., "Fluid Dynamics of Interacting Blade Tip Vortices With a Ground Plane," 64th Annual Forum of the American Helicopter Society, Montréal, Canada, April 2008.

[5] Johnson, B., Leishman, J.G., and Sydney, A., "Investigation of Sediment Entrainment in Brownout Using High-Speed Particle Image Velocimetry," 65th Annual Forum of the American Helicopter Society, Grapevine, TX, 27-29 May 2009.

[6] Whitehouse, G.R., Wachspress, D.A., Quackenbush, T.R., and Keller, J.D., "Exploring Aerodynamic Methods for Mitigating Brownout," 65th Annual Forum of the American Helicopter Society, Grapevine, TX, 27-29 May 2009.

[7] Haehnel, R.B., Moulton, M.A., Wenren, Y., and Steinhoff, J., "A Model to Simulate

Rotorcraft-Induced Brownout," 64th Annual Forum of the American Helicopter Society, Montréal, 2008.

[8] Wachspress, D.A., Whitehouse, G.R., Keller, J.D., McClure, K, Gilmore, P., and Dorsett, M., "Physics Based Modeling of Helicopter Brownout for Piloted Simulation Applications," Interservice/Industry Training, Simulation and Education Conference (I/ITSEC), Orlando, Florida, Dec 2008.

[9] Wachspress, D.A., Whitehouse, G.R., Keller, J.D., K., Yu, Gilmore, P., Dorsett, M., and McClure, K, "A High Fidelity Brownout Model for Real-Time Flight Simulations and Trainers," 65th Annual Forum of the American Helicopter Society, Grapevine, TX, 27-29 May 2009.

[10] D'Andrea, A., "Numerical Analysis of Unsteady Vortical Flows Generated by a Rotorcraft Operating on Ground: a First Assessment of Helicopter Brownout," 65th Annual Forum of the American Helicopter Society, Grapevine, TX, 27-29 May 2009.

[11] Wadcock, A.J., Ewing, L.A., Solis, E., Potsdam, M., and Rajagopalan, G., "Rotorcraft Downwash Flow Field Study to Understand the Aerodynamics of Helicopter Brownout," American Helicopter Society Southwest Region Technical Specialists' Meeting, Dallas-Fort Worth, TX, 15-17 October 2008.

[12] Betz, A., "The Ground Effect on Lifting Propellers," NACA TM 836, NACA, August 1937.

[13] Knight, M. and Hefner, R.A., "Static Thrust Analysis of the Lifting Airscrew," T.N. No. 626, 1937.

[14] Knight, M. and Hefner, R.A., "Analysis of Ground Effect on the Lifting Airscrew," NACA TN 835, National Advisory Committee for Aeronautics, 1941.

[15] Zbrozek, J., "Ground Effect on the Lifting Rotor," R & M 2347, Aeronautical Research Council, July 1947.

[16] Cheeseman, I.C. and Bennett, W.E., "The Effect of the Ground on a Helicopter Rotor in Forward Flight," R & M 3021, Aeronautical Research Council, 1957.

[17] Hayden, J.S., "The Effect of the Ground on Helicopter Hovering Power Required," 32nd Annual Forum of the American Helicopter Society, Washington, D.C., 10-12 May 1976.

[18] Fradenburgh, E.A., "The Helicopter and the Ground Effect Machine," *Journal of the American Helicopter Society*, Vol. 5 (4), October 1960, pp. 24–33.

[19] Sheridan, P.F. and Wiesner, W., "Aerodynamics of Helicopter Flight Near the Ground," 33rd Annual forum of the American Helicopter Society, Washington DC, May 9 - 11 1977.

[20] Curtiss Jr., H.C., Sun, M., Putman, W. F., and Hanker Jr., E. J., "Rotor Aerodynamics in Ground Effect At Low Advance Ratios," *Journal of the American Helicopter Society*, Vol. 29 (1), 1984, pp. 48–55.

[21] Whitehouse, G.R. and Brown, R.E., "Modelling Rotor Wakes in Ground Effect," *Journal of the American Helicopter Society*, Vol. 49 (3), July 2004, pp. 238–249.

[22] Curtiss Jr., H.C., Erdman, W., and Sun, M., "Ground Effect Aerodynamics," *Vertica*, Vol. 11 (1-2), 1987, pp. 29–42.

[23] Cimbala, J.M., Billet, M.L., Gaublomme, D.P., and Oefelein, J.C., "Experiments on the Unsteadiness Associated with a Ground Vortex," *Journal of Aircraft*, Vol. 28 (4), April 1991, pp. 261–267.

[24] Saijo, T., Ganesh, B., Huang, A., and Komerath, N., "Development of Unsteadiness in a Rotor Wake in Ground Effect," 21st AIAA Applied Aerodynamics Conference, Orlando, FL, 23-26 June 2003.

[25] Saijo, T., Ganesh, B., Huang, A., Komerath, N.M., Bhattacharya, S., Pulla, D.P., and Conlisk, A.T., "Development of Unsteadiness in the Wake of a Rotor in Ground Effect," 59th Annual forum of the American Helicopter Society, Phoenix, AZ, 6-8 May 2003.

[26] Ganesh, B. and Komerath, N., "Unsteady Aerodynamics of Rotorcraft in Ground Effect," 22nd Applied Aerodynamics Conference and Exhibit, AIAA, Providence, RI, 16-19 August 2004, pp. 1–11.

[27] Ganesh, B. and Komerath, N., "Study of Ground Vortex Structure of Rotorcraft in Ground Effect at Low Advance Ratios," 24th AIAA Applied Aerodynamics Conference, AIAA, San Francisco, CA, 5-8 June 2006.

[28] Light, J.S., "Tip Vortex Geometry of a Hovering Helicopter Rotor in Ground Effect," *Journal of the American Helicopter Society*, Vol. 38 (2), April 1993, pp. 34–42.

[29] Preston, J.R., "VTOL Downwash / Outwash Operational Effects Model," American Helicopter Society 50th Annual Forum, Washington DC, May 1994.

[30] Graber, A., Rosen, A., and Seginer, A., "An Investigation of a Hovering Rotor in Ground Effect," *Aeronautical Journal*, Vol. 95, May 1991, pp. 161–169.

[31] Keller, J.D., Whitehouse, G.R., Wachspress, D.A., Teske, M.E., and Quackenbush, T.R., "A Physics-Based Model of Rotorcraft Brownout for Flight Simulation Applications," 62nd Annual Forum of the American Helicopter Society, Phoenix, AZ, May 9-11 2006.

[32] Griffiths, D.A., Ananthan, S., and Leishman, J.G., "Predictions of Rotor Performance in Ground Effect Using a Free-Vortex Wake Model," *Journal of the American Helicopter Society*, Vol. 50 (4), October 2005, pp. 302–314.

[33] Griffiths, D.A. and Leishman, J.G., "A Study of Dual-Rotor Interference and Ground Effect Using a Free-Vortex Wake Model," 58th Annual Forum and Technology Display

of the American Helicopter Society, Vol. 1, Montréal , Canada, 11-13 June 2002, pp. 592–612.

[34] Brown, R.E. and Line, A.J., "Efficient High-Resolution Wake Modelling Using the Vorticity Transport Equation," *AIAA Journal*, Vol. 43 (7), July 2005, pp. 1434–1443.

[35] Kenyon, A.R. and Brown, R.E., "Wake Dynamics and Rotor-Fuselage Aerodynamic Interactions," *Journal of the American Helicopter Society*, Vol. 54 (1), January 2009.

[36] Kim, H.W. and Brown, R.E., "Coaxial Rotor Performance and Wake Dynamics in Steady and Manoeuvring Flight," 62nd Annual Forum of the American Helicopter Society, Phoenix, Arizona, May 2006.

[37] Phillips, C. and Brown, R.E., "Eulerian Simulation of the Fluid Dynamics of Helicopter Brownout," *Journal of Aircraft*, Vol. 46 (4), July 2009, pp. 1416–1429.

[38] Phillips, C. and Brown, R.E., "The Effect of Helicopter Configuration on the Fluid Dynamics of Brownout," 34th European Rotorcraft Forum, Liverpool, UK, 16-19 September 2008.

[39] Phillips, C., Kim, H.W., and Brown, R.E., "The Effect of Rotor Design on the Fluid Dynamics of Helicopter Brownout," 35th European Rotorcraft Forum, Hamburg, Germany, 22-25 September 2009.

[40] Brown, R.E., "Rotor Wake Modeling for Flight Dynamic Simulation of Helicopters," *AIAA Journal*, Vol. 38 (1), January 2000, pp. 57–63.

[41] Toro, E.F., "A Weighted Average Flux Method for Hyperbolic Conservation Laws," *Proceedings of the Royal Society of London, Series A: Mathematical and Physical Sciences*, Vol. 423 (1864), 1989, pp. 401–418.

[42] Whitehouse, G.R. and Brown, R.E., "Modelling a Helicopter Rotor's Response to Wake Encounters," *Aeronautical journal*, Vol. 108 (1079), January 2004.

[43] Ahlin, G.A. and Brown, R.E., "Investigating the Physics of Rotor Vortex-Ring State using the Vorticity Transport Model," 31st European Rotorcraft Forum, Florence, Italy, September 2005.

[44] Ahlin, G.A. and Brown, R.E., "The Vortex Dynamics of the Rotor Vortex Ring Phenomenon," 63rd Annual Forum of the American Helicopter Society, Virginia Beach, Virginia, May 2007.

[45] Fletcher, T.M. and Brown, R.E., "Modelling the Interaction of Helicopter Main Rotor and Tail Rotor Wakes," *Aeronautical Journal*, Vol. 111 (1124), October 2007.

[46] Brown, R.E., *Numerical Solution of the Two-Dimensional Navier-Stokes Equations Using Viscous-Convective Operator Splitting*, M.sc. thesis, Cranfield Institute of Technology, 1990.

[47] Strang, G., "On the Construction and Comparison of Finite Difference Schemes," *SIAM Journal of Numerical Analysis*, Vol. 5, 1968, pp. 995–1011.

[48] Toro, E.F., "Some Aspects of Shock Capturing Methods for Gas Dynamics," 9112, College of Aeronautics Report, Cranfield Institute of Technology, June 1991.

[49] Rosenhead, L., "The Spread of Vorticity in the Wake Behind a Cylinder," *Proceedings of the Royal Society of London, Series A*, Vol. 127 (590), 1930.

[50] Moore, D.W., "Finite Amplitude Wave on Aircraft Trailing Vortices," *Aero. Quarterly*, Vol. 23 (307), 1972.

[51] Greengard, L. and Rokhlin, V., "A Fast Algorithm for Particle Simulations," *Journal of Computational Physics*, Vol. 135, 1997, pp. 280–292.

[52] Weissinger, J., "The Lift Distribution of Swept-Back Wings," 1120, NACA Technical Memorandum, March 1947.

[53] Cooke, A.K. and Fitzpatrick, E.W.H., *Helicopter Test and Evaluation*, American Institute of Aeronautics and Astronautics Education Series, Reston, VA, 2002.

[54] Bagnold, R.A., *The Physics of Blown Sands and Desert Dunes*, Methuen & CO. LTD., London, 1941.

[55] Lu, H. and Shao, Y., "Toward Quantitative Prediction of Dust Storms: An Integrated Wind Erosion Modelling System and its Applications," *Environmental Modelling and Software*, Vol. 16 (3), April 2001, pp. 233–249.

[56] Raupach, M.R., Gillette, D.A., and Leys, J.F., "The Effect of Roughness Elements on Wind Erosion Threshold," *Journal of Geophysical Research*, Vol. 98 (D2), 20 Feb 1993, pp. 3023–3029.

[57] MacKinnon, D.J., Clow, G.D., Tigges, R.K., Reynolds, R.L., and Chavez Jr., P.S., "Comparison of Aerodynamically and Model-derived Roughness Lengths (Zo) Over Diverse Surfaces, Central Mojave Desert, California, USA," *Geomorphology*, Vol. 63 (1-2), November 2004, pp. 103–113.

[58] Zender, C.S., Huisheng, B., and Newman, D., "Mineral Dust Entrainment and Deposition (DEAD) Model: Description and 1990s dust climatology," *Journal of Geophysical Research*, Vol. 108 (D14), 2003.

[59] Yin, D., Nickovic, S., Barbaris, B., Chandy, B., and Sprigg, W.A., "Modeling Wind-Blown Desert Dust in the Southwestern United States for Public Health Warning: A Case Study," *Atmospheric Environment*, Vol. 39 (33), 2005, pp. 6243–6254.

[60] White, B.R., "Soil Transport by Winds on Mars," *Journal of Geophysical Research*, Vol. 84 (B9), August 1979, pp. 4643–4651.

[61] Marticorena, B. and Bergametti, G., "Modeling the Atmospheric Dust Cycle: 1. De-

sign of a soil-derived dust emission scheme," *Journal of Geophysical Research*, Vol. 100 (D8), August 1995, pp. 16415–16430.

[62] Cheng, N.-S., "Simplified Settling Velocity Formula for Sediment Particle," *Journal of Hydraulic Engineering*, Vol. 123 (2), February 1997, pp. 149–152.

[63] Project on Government Oversight, "Brownout Accidents Plague CSAR-X Helicopter: Controversy Surrounds Air Force Selection," 2007.

[64] US Army, "Army Aircraft Mishaps/Accidents and Percentage of Chinook Accidents," 7 March 2007.

[65] Ahlin, G.A. and Brown, R.E., "Wake Structure and Kinematics in the Vortex Ring State," *Journal of the American Helicopter Society*, Vol. 54 (3), July 2009.

[66] Sykora, B., "Rotorcraft Visual Situational Awareness Solving the Pilotage Problem for Landing in Degraded Visual Environments," 65th Annual Forum of the American Helicopter Society, Grapevine, TX, 27-29 May 2009.

[67] Jansen, C., Wennemers, A., Vos, W., and Groen, E., "FlyTact: A Tactile Display Improves a Helicopter Pilot's Landing Performance in Degraded Visual Environments," *Lecture Notes In Computer Science*, Vol. 5024, 2008, pp. 867–875.

[68] Stepniewski, W.Z. and Keys, C.N., *Rotary-Wing Aerodynamics*, Dover Publications, Inc., New York, 1984.